NTNU
Norwegian University of
Science and Technology

A Winkler Model for the Seismic Analysis of Monopile Foundations

An Exploratory Study on the Modelling of
Soil-Structure Interaction during
Earthquakes

Thijs Bouman

Preface

This thesis is submitted in partial fulfilment of the requirements for the degree of Master of Science in "Offshore and Dredging Engineering" at the Department of Offshore Engineering at the Delft University of Technology, and in "Technology - Wind Energy" at the Departments of Civil and Environmental Engineering and Marine Technology at the Norwegian University of Science and Technology. This research has been carried out at the engineering & estimating department at Van Oord in Gorinchem, the Netherlands.

The aim of this research has been to investigate the impact of earthquakes on monopile foundations for the offshore wind sector. The focus of this thesis is on the soil-structure interaction, as this showed to be one of the major uncertainties in the seismic analysis.

This research started in Trondheim, Norway, as a Specialisation Project at the NTNU. I would like to thank Dr. ir. E. Bachynski for her advice and guidance during this entire project. Another word of thanks goes out to my to my TU Delft supervisors Prof. dr. A.V. Metrikine and Dr. ir. F. Pisanò for providing me with feedback throughout the graduation process in Delft.

I would also like to thank Ir. W. Op den Velde and Ir. R.J.N.J. Luiken for their help and for providing me with the opportunity to conduct my research at Van Oord.

Lastly, I would like to thank Tony. Your insights and unlimited enthusiasm for analysis methods definitely contributed to this thesis.

<div align="right">
T. Bouman
Rotterdam, November 2018
</div>

Abstract

The growing interest in the development of offshore wind farms in seismic active areas demands a better insight into the requirements earthquakes impose on the design of wind turbine foundations. The complexity of the soil-structure interaction (SSI) during an earthquake results in large uncertainties in the design process of a monopile foundation. The design codes do not provide a structured framework on how to deal with these uncertainties. On top of this, the design codes are for (offshore) structures in general and do not specify for the large diameter tubulars which are characteristic for the offshore wind energy sector.

This thesis presents the investigation into a 1D seismic Winkler foundation that is able to represent the SSI during an earthquake. The model, a beam on nonlinear Winkler foundation (BNWF) coupled with a nonlinear ground response model, is a fast method to determine the structural response for the stochastic seismic and offshore wind load cases. Semi-empirical formulations are used to implement cyclic loading effects into the model. A 3D finite element model of an embedded monopile is developed in parallel with the seismic Winkler foundation for tuning and validation purposes.

The resistance of the soil to lateral pile deflections is further investigated to address the uncertainty in the SSI. A 2D horizontal cross-section of the embedded monopile is considered to determine the linear dynamic properties (impedance) of the soil, and a plane strain finite element model is developed to investigate the effect of nonlinear soil behaviour. A combined frequency-time domain method is used as extension for the Winkler foundation to incorporate the obtained frequency-dependent foundation properties into a time-domain analysis.

It was found that none of the 2D analyses resulted in SSI representation that could be directly applied in a time-domain analysis. Moreover, the large D/L ratio of a monopile activates a global soil response, making an uncoupled 2D analysis inaccurate for the frequency range of interest.

Keywords: Monopile foundation, Soil-structure interaction (SSI), Seismic response model, Liquefaction, Beam on nonlinear Winkler foundation (BNWF), Soil response, Hybrid frequency-time domain model

Nomenclature

Abbreviations and Acronyms

ALE	abnormal level earthquake	HAWT	horizontal axis wind turbine
ALS	accidental limit state	LCOE	levelised cost of energy
BEM	blade element momentum	MP	monopile
BNWF	beam on nonlinear Winkler foundation	MSL	mean sea level
		NDOF	N degree of freedom
BoP	balance of plant	NPS	neutral plane solution
CapEX	capital expenditure	ODE	ordinary differential equation
CCF	controllable canonical form	OWT	offshore wind turbine
COG	centre of gravity	PHA	peak horizontal acceleration
CPT	cone penetration test	PHV	peak horizontal velocity
CSL	critical-state line	PSHA	probabilistic seismic hazard analysis
DOF	degree of freedom	RNA	rotor nacelle assembly
DSHA	deterministic seismic hazard analysis	SCPT	seismic cone penetration test
ELE	extreme level earthquake	SDOF	single degree of freedom
EOM	equation of motion	SISO	single input single output
FA	fore-aft	SLS	serviceability limit state
FE	finite element	SPT	standard penetration test
FEA	finite element analysis	SS	state-space
FEM	finite element method	SSI	soil-structure interaction
FLS	fatigue limit state	SVD	singular value decomposition
		ULS	ultimate limit state

Notation

			kind
$H(s)$	Transfer function	I_1, J_2, J_3	Stress invariants
ω	Frequency parameter	κ	Permeability of the soil
s	Complex Laplace parameter	K_n	N-th order Bessel function of the second kind
$\mathbf{A}(\omega), \mathbf{B}(\omega)$	Added mass and damping matrices		
$\bar{\mathbf{A}}, \bar{\mathbf{B}}, \bar{\mathbf{C}}, \bar{\mathbf{D}}$	Markov parameter matrices	k_m, K_s, K_f	Biot, soil and fluid bulk modulii
$\mathbf{A}', \mathbf{B}', \mathbf{C}', \mathbf{D}'$	State-space linear relation matrices	$\mathbf{M}, \mathbf{C}, \mathbf{K}$	Mass, damping and stiffness matrices
A_i, B_i	Integration constants	ν	Pressure dependent fitting constant
α	Biot coefficient	ϕ	Internal friction angle
β, s	Curve fitting constants	σ_c	Confining stress
ψ	Dilation angle	σ'	Effective stress
$\mathbf{D}$	Elastic tangent stiffness matrix	Σ	Singular values
ϵ	Strain tensor	τ_0	Maximum shear strength
$\vec{F_R}$	Retardation's force component	θ	Lode angle
$\vec{F}$	External force	u	residual pore-pressure
γ	Shear strain	u	Excitation (SISO system)
γ_f	Specific fluid weight	$\mathbf{U}, \mathbf{V}$	Mode shapes of the singular values
G_0	Initial shear modulus	$\vec{x}$	State variables of the str
g	Gravity acceleration vector	$\vec{X}$	Complex response amplitude
h_d	Discrete impulse response	y	Response (SISO system)
I_n	N-th order Bessel function of the first	$\vec{z}$	State variables of the system

Contents

Chapter 1

Introduction

The offshore wind industry has experienced an enormous growth in the last decade. This industry is mainly concentrated in Northwestern Europe, where the design conditions are well established and the foundations optimised to a high degree. Also other parts of the world can benefit from offshore wind power as means of energy production. However, the environmental conditions at these locations can be significantly different from the North Sea as many of the areas are well known for their high risk of strong earthquakes. The impact of earthquakes on the stability and the structural integrity of offshore wind turbines has only recently become of interest and is therefore a relatively new field of research.

With the recently sparked interest in the development of offshore wind farms in seismic active areas comes the demand for a better insight in the requirements earthquakes impose on the design of substructures for offshore wind. For example, the complexity of the SSI during an earthquake results in many uncertainties in the design process of a monopile foundation. The design codes used in the offshore and seismic engineering sectors do not give a structured framework on how to deal with these uncertainties, leading to the use of various design methods instead of a clear unified approach. On top of this, most design codes are for (offshore) structures in general and do not specify for the large diameter tubulars which are characteristic for the wind energy sector. More research into the seismic soil-structure interaction and structural behaviour of the foundations should support a more unified design approach.

Various attempts to develop a 1D computationally efficient model that is able to capture the SSI during an earthquake event are presented in this thesis. Such a model can be used to more accurately incorporate earthquake loading into monopile design tools. The thesis covers the modelling attempts and presents the issues faced during the process.

1.1. Background

The need for more reliable predictions of earthquake loading on monopile foundations arises from the interest in the development of offshore wind farms in seismic active areas. The developments in the offshore wind sector are presented on the basis of the key figures and trends. This is followed by a brief literature review of the seismic response of piles and wind turbines. Finally, the impact of SSI for offshore monopile foundations is discussed.

1.1.1. Offshore Wind Energy

The wind energy sector has seen an enormous growth over the last couple of decades. This can be clearly seen from Figure 1.1, which shows the cumulative and annual installed wind energy capacity in Europe since 1994. The figure shows an exponential growth, which is expected to continue for the coming decade. This is partly because of the greenhouse gas emission target set at the 2015 Paris Climate Accord, which moved many countries to upscale their investments in greener energy resources.
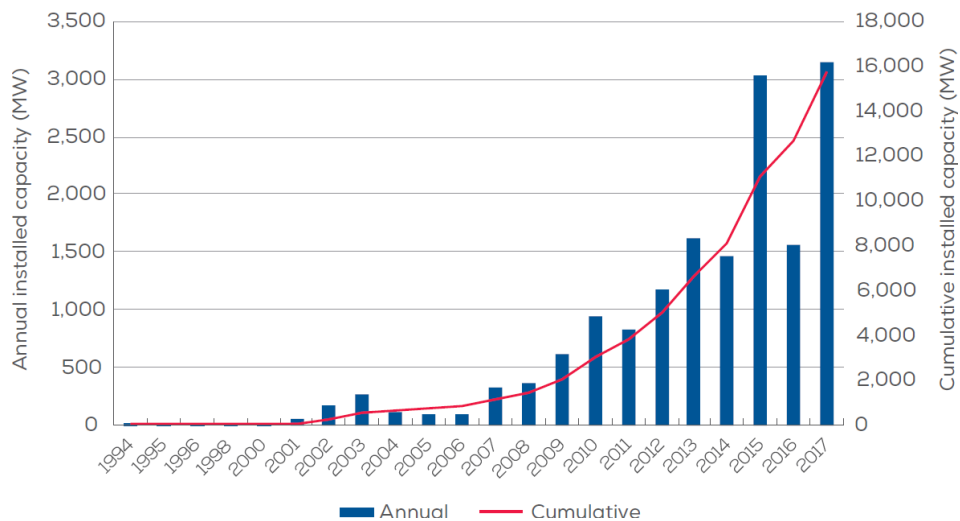
Figure 1.1: Cumulative and annual European offshore wind energy installation (121)

The goal of a minimum 27% share of renewable energy led to the development of many new wind energy projects.

In 2016 just over 4% (2,219 MW) of the worldwide newly installed wind energy capacity was located offshore (39). Offshore wind has many advantages over onshore, such as a more stable wind climate [1], more space and no conflict with regional politics. A major drawback used to be the relatively high costs of offshore compared to onshore. But, with bids of 49.90 €/MWh for the Kriegers Flak project in Denmark and 54.50 €/MWh for Borssele 3 & 4 in the Netherlands, the prices are becoming competitive (39).

To be able to compare energy prices is in the energy sector often referred to the levelised cost of energy (LCOE). This is the total investment (capital, operation and maintenance) divided by the total produced electrical energy. This value (Euro per megawatt-hour) can be used as a measure of comparison and efficiency of the project. A campaign is ongoing in the offshore wind energy sector to reduce this LCOE to become competitive with fossil fuel types. The current LCOE for offshore wind energy in Germany is in the range of 74.9 - 137.9 €/MWh, while that of brown coal is between 45.9 - 79.8 €/MWh (65).

At the end of 2016 almost 88% (12.63 GW) of the worldwide installed offshore wind capacity was located in the coastal waters of Northwest Europe. The remaining 12% was located largely in China (11%), with the remainder in Japan, South Korea and the United States (39). Although Europe is expected to stay the world leader in the near future, other markets like North and Latin America, China, Taiwan, South Korea, Vietnam, India and Australia are investing in offshore wind energy (80; 39). Note that most of these locations are subjected to a certain level of seismicity.

1.1.2.   Offshore Wind Foundations

Almost all wind energy foundations installed to this day are bottom founded structures. The floating wind energy market is slowly winning popularity as 80% of the offshore wind resource in Europe is located in waters of 60 m and deeper. At these depths, traditional bottom-fixed offshore wind foundations are no longer economically attractive (120). However, with up to today only a single installed floating wind farm[2], bottom founded will stay the backbone of the industry for the time being.

The installed substructure types in Europe at the end of 2017 are the monopile (81.7%), jacket (6.9%), gravity-based (6.2%), tripod/tripile (4.7%) and the floating spar buoy (0.13%) (121). A typical monopile foundations is presented in Figure 1.2. The numbers show that the monopile is by far the most popular

---

[1] Higher and steadier wind speeds across open water, resulting in less turbulence.
[2] Statoil's Hywind project, Scotland

Figure 1.2: Artist impression of a typical monopile foundation for an offshore wind turbine. The figure shows the monopile, (integrated) transition piece and secondary steel (boatlanding, platform and ICCP system). It can be seen that the shell of the pile consists of can sections. (Source: unknown)
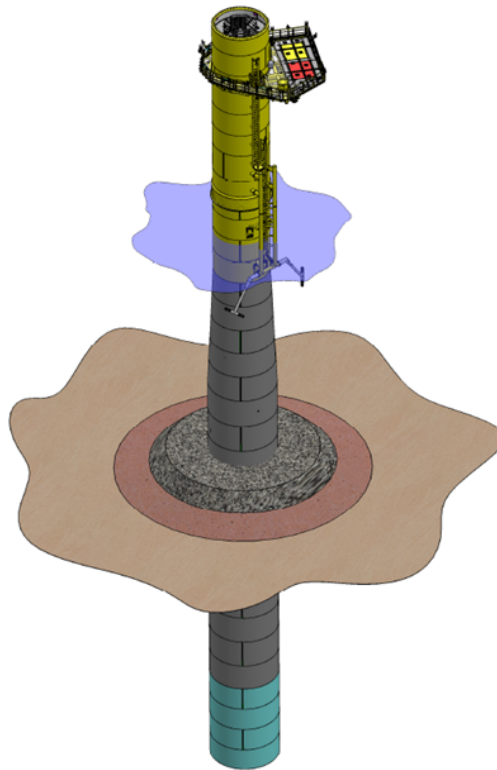
foundation type. This is due to its relatively easy fabrication and installation, which makes it a strong competitor to the other foundation types in shallow to moderate water depths. The cost of a monopile foundation varies between the 15% and 34% of the total capital expenditure (CapEX) of an offshore wind turbine (OWT), making up almost 32% to 65% of the total balance of plant (BoP) (18; 104). I.e., optimising the substructure could yield significant savings in the total LCOE.

The current trend in offshore wind turbine design is to increase the size of the turbines. The power produced by an offshore wind turbine is quadratically related to the the rotor area of the turbine. Increasing the rotor diameter decreases the required number of turbines for the same energy output, often bringing down the costs of both capital and maintenance. Currently, turbines with a rotor diameter of up to 164 meter are commercially available (114). To support the increasing turbines, the support structures have to increase likewise to accommodate the strength and stiffness requirements. Although a monopile foundation is a relatively simple structure consisting of only a single tubular, its increasing diameter and D/t ratio result in some uncertainties when it comes to strength capacity, loading and SSI.

1.1.3. Seismic Loading of Offshore Wind Turbines

Wind turbines are tall slender structures with a large concentrated mass at hub level. The support structures are designed to avoid the excitation frequencies (wind, wave and blade-passing frequency ranges) while being as flexible as possible out of economic consideration. This relatively large flexibility of the structure makes them also insensitive to a broad part of the seismic excitation frequency range as this is well above the fundamental natural frequency of the structure (56). However, OWT are not proven to be resistant against all seismic hazards. First of all, there are possibly different failure mechanisms involved, e.g. excessive base rotation due to liquefaction and subsoil deformations in the relatively thin monopile shell.

Seismic Evaluation of Wind Turbines

Studies for turbines smaller than 1.65 MW show that seismic loading will not be the critical load case for the support structure (9; 61; 71; 87). Also, for the larger 5 MW NREL turbine (53), the base shear

Table 1.1: Table for quick overview of design codes

Field	Standard
General offshore	• RP2A-WSD (7) • ISO19901-2 (49)
Offshore wind	• (95) • IEC 61400-1 Ed.3 - Part 1 (46) • Guideline for the Certification of Wind Turbines (34) • DNV-OS-J101 (27)
Piles in liquefiable soils	• Eurocode 8 (EN 1998-5:2004) • JRA • AASHTO • ISO-23469

and the nacelle's acceleration response for a moderate earthquake is comparable to that of a moderate sea condition (126; 116). (66) shows that due to its flexible support structure, a large 10 MW wind turbine superstructure is generally insensitive to horizontal ground shaking when subjected to pure earthquake loading. However, the combination of wind, wave, current and seismic loading needs to be properly accounted for as coupling effects leads to excessive base rotation. Also, out-of-phase oscillation of the tower-nacelle system results in additional stresses in the foundation.

Vertical seismic loading is often neglected in the seismic analysis of piles. However, support structures are generally stiffer in the vertical direction resulting in natural frequencies close to earthquake loading spectra (58). (96) showed a high vertical response in an OWT due to earthquake loading. More detailed studies by (44; 63; 62) agree that not only horizontal, but also vertical excitation could be a critical load case.

According to (48; 92), higher modes should be considered to accurately capture the dynamics of larger turbines, as these modes have a considerable contribution. The response spectrum approach as proposed in (95) becomes inadequate to estimate accurate peak shear forces and moments. (78) find that the aerodynamic damping of the wind turbine has a considerable influence on the seismic dynamic response of the wind turbine structure. A closed-form solution for the aerodynamic damping of a horizontal axis wind turbine (HAWT) is given by (108). They estimate the aerodynamic damping in the fore-aft direction for a 1.5-MW turbine to be between 0.0% and 0.6% for parked conditions and between 3.7% and 5.4% under operational conditions. For the side-side direction, the estimates are between 0.0% and 0.3%. These values deviate from the proposed 5% that is often applied in guidelines for the seismic analysis of structures. On the other hand, the contribution of hydrodynamic damping is overall small according to (126).

Seismic Guidelines

Several building guidelines include seismic design requirements in their contents. The offshore (oil & gas) sector also provides seismic design guidelines, such as the RP2A-WSD (7) and the ISO19901-2 (49). These design guidelines apply to offshore structures in general and do not specify for offshore wind structures.

There are four main standards and guidelines that provide direct seismic guidance for the offshore wind sector according to (91) and (58), which are presented in table 1.1 under "offshore wind standards". These guidelines provide a rather simple single degree of freedom (SDOF) seismic model (95), focus only on stating the requirements for analysis of seismic loads (34; 46) and primarily specify for the tower, not the substructure. The most recent standard, (27), specifies local ground amplification effects instead of using only the surface ground motions. The guidelines often depend on the use of other guidelines: the (34) refers to the (31) and the (7), while (27) refers for the seismic design criteria to the ISO19901-2 (49).

Most of the guidelines mentioned by (91) are based on seismic guidelines for buildings. These guidelines generally use a earthquake event based on a return period of 475 years. On the other hand, the ISO19901-2 addresses earthquake induced ground motions based on site-specific probabilistic seis-

mic hazard analysis (PSHA), and focuses on a two level seismic performance requirement: 1. extreme level earthquake (ELE) performance: Little or no damage to the primary structural and foundation components, and 2. abnormal level earthquake (ALE) performance: Plastic degrading behaviour is allowed in structural elements, but catastrophic failures should be avoided. The ELE and ALE return periods depend on the exposure level as prescribed by ISO29902 and ISO19903. For unmanned OWT structures these are 500 and 3000 years respectively. The ELE return period is in line with a return period of 475 years used throughout building codes, allowing the use of local seismic hazard data (59).

Piles are often chosen as preferred foundation type in liquefiable soils due to their proven ability to perform well in past earthquakes where soil has liquefied due to seismic loading (33). However, there is currently limited guidance on applying a performance based framework to piles. It is often preferable to have piles remain elastic as subsurface damage is difficult to assess. For this reason, design codes typically instruct the use of a large safety factor to avoid the formation of a plastic hinge in the pile. Further, almost all codes distinguish between inertial and kinematic interaction. These will be discussed in more detail in chapter 2. Several national and international standards (according to (33)) which cover design of piles in liquefiable soils are presented in table 1.1. They are based on the concept of Performance Based Earthquake Engineering (PBEE) (50). It must be noted that these codes are intended for slender piled foundations.

1.1.4.   Soil-Structure Interaction

The soil characteristics and the SSI mechanism contribute to most to the modelling uncertainties in the design of monopiles (101). This is due the the many unknown and possible spatial variation of the soil parameters in the seabed. Moreover, the exact mechanism involved in the interaction between the soil and the large diameter monopile are not yet well understood.

The SSI has been found to be a critical aspect in the analysis and design of wind turbines as it has a significant impact on the response of the structure to dynamic loading (73; 23). Studies by (124; 4; 123) showed that the mode shapes, eigenfrequencies and damping of the structure are influenced by the foundation stiffness, i.e. SSI model. (90; 99) state that the effects of SSI also play a significant role in the seismic analysis of wind turbines as it influences the dynamic response and the settlement of the structure (123). However, it is emphasised that the observation and analysis of SSI is difficult, especially in the case of soil liquefaction (123).

An often applied method to model the SSI is to use a BNWF. Several studies have been performed with this method (125; 52; 103) and more than 10% eigenfrequency reduction has been found (9). For detailed analysis, more advanced soil modelling is often favoured over the conventional Winkler-beam foundation method. The latter shows to give less accurate results for the large diameters typical for the offshore wind sector (76). The Pile Soil Analysis project (PISA), is a large joint industry project aimed at investigating and developing improved design methods for laterally loaded piles, specially tailored to the offshore wind sector (17). This project developed an improved P-Y method, which is better capable of capturing the SSI of the monopile. (59) points out that this method might be of interest for seismic analysis.

The non-linear behaviour of soil is found to be of high relevance for the seismic response of wind turbines (3; 79; 11). Studies by (81; 32; 82; 57) into the kinematic and inertial seismic behaviour of piles used in civil structures showed that the embedded part of the foundation could be susceptible to damage. Stresses due to shear motions in the soil column are shown to have destructive impact on pile foundations. Furthermore, a study by (60) on the seismic fragility of offshore wind turbines shows that it is important to take details such as soil interfaces into account. (42) on the other hand found that the effect of soil interfaces loses importance for larger diameters as kinematic response may dominate the cases of large diameter piles. It is explicitly stated that further research is necessary. A paper by (26) states that there is a limited diameter range for piles in seismic regions. This is due to the contribution of the kinematic and inertial actions, which are affected by the stiffness of the pile in a different manner. The validity of the size limitation for monopiles with low L/D ratios needs to be determined.

Piles in Liquefiable Ground

Several authors have looked into the behaviour of slender piles in liquefiable ground as many failures of piled foundations for civil structures have been reported after major earthquakes. Most design and analysis methods for piles in liquefiable ground split the piles response into kinematic soil-pile interaction and inertial pile-superstructure interaction. Model tests have been conducted to investigate the seismic demand and effect of liquefaction on pile foundations (13; 28; 106; 15). These tests boosted the understanding of seismic pile response in liquefiable ground.

The SSI is often modelled as Winkler-beam foundation as mentioned before. Attempts to extended the P-Y method for liquefied soils has been done by adapting the P-Y curves (97). However, this pseudo-static approach fails to capture the dynamics and the change of soil properties during earthquakes (115). Dynamic P-Y formulations have been done by (13; 72; 74). These are based on free field effective stress and soil stiffness degradation to account for soil liquefaction. A method by (109) uses a semi-empirical method to determine near field pore pressure and plastic energy generation in the p-y element. Different semi-empirical models to estimate pore pressure buildup on which the initiation of soil liquefaction can be estimated have been developed (24; 89; 37). It is pointed out that P-Y methods over-simplify the dynamic response of soil and the approximation of the material properties tend to be rather crude (115).

1.2.   Thesis Objective

The development of offshore wind farms in seismic active areas presents offshore wind foundation designers with the challenge of a complex new type of loading. This leads to the need of a solid understanding of the potential failure modes due to seismic loading and a method to estimate the damage to the offshore wind turbines and their foundations. Geotechnical earthquake engineering has been a topic of research since the 60's and much understanding in the fields of soil mechanics and SSI has been achieved since. However, researchers and engineers still struggle to accurately model and predict the earthquake induced structural dynamics as this requires large inefficient finite element (FE) models and/or has a lot of uncertainties/assumptions.

Therefore, the objective of this thesis is to investigate possible methods to implement seismic loading into a computationally efficient 1 dimensional Winkler-beam model, and identify the problems and uncertainties of these methods.

There are three major components to be considered in a seismic analysis; the soil, the structure and the interaction between these two. Offshore wind turbine structures are generally insensitive to the earthquake loading as the natural frequencies of the structure are outside the exciting seismic frequency range (66). Therefore, the focus of the thesis is on the SSI during seismic loading.

1.3.   Structure of Thesis

The thesis is organised into the following chapters:

Chapter 2   Theoretical background. Relevant theoretical background on monopile support structures, soil mechanics, soil-structure interaction and geotechnical earthquake engineering.

Chapter 3   3D seismic monopile response model. The numerical formulation of the 3D finite element seismic monopile response model. The monopile and soil characteristics used throughout the thesis are presented here as well.

Chapter 4   Seismic Winkler-Beam Model. The Winkler-beam model, which is often the preferred model type for the dynamic analysis of monopile foundations, is combined with a ground response model in an attempt to better capture the dynamic response to seismic loading. This chapter covers the numerical formulation of the models and looks into various methods for state-dependent P-Y curves.

Chapter 5   Soil-Structure interaction. A 2 dimensional plane stress/strain analysis to determine the foundations response to lateral loading. First, the linear small strains response of the soil is analysed. Secondly, the faced issues while trying to determine the seismic soil degradation

Figure 1.3: Flowchart representation of the structure of the thesis. The arrows represent data/result dependency of the sections.
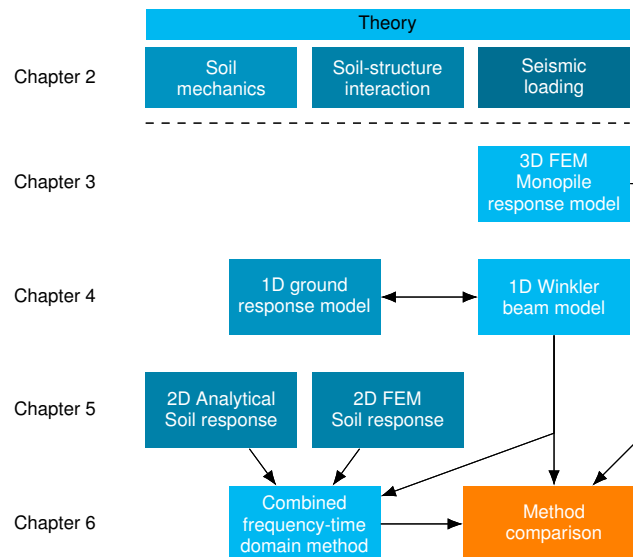
and liquefaction impact are presented.

Chapter 6   Frequency-Time Domain Winkler Foundation. A method to implement frequency dependent foundation parameters into a time domain analysis of a Winkler-Beam model.

Chapter 7   Conclusions, discussion and recommendation for further work. The main findings of the thesis are summarised and discussed. Finally, recommendations for further research into seismic behaviour of substructures for offshore wind will be presented.

The structure of the thesis is presented in figure 1.3.

1.4.   Software Used

The following software was used throughout this thesis:

ANSYS Mechanical 19.1	Finite Element Analysis programme	ANSYS, Inc.
Microsoft Excel 2016	Spreadsheet programme	Microsoft
MATLAB R2018a	Numeric computing environment	MathWorks, Inc.
Maple 2018	Symbolic and numeric computing environment	Maplesoft

Chapter 2

Theoretical Background

2.1.   Introduction

This chapter gives an overview of the relevant background information and theories on which the thesis is based. The chapter is divided into four sections. First, section 2.2 covers monopile foundations. Here, the design process of a monopile is briefly presented. After this, section 2.3 presents the fundamentals of soil mechanics. This is followed by section 2.4, which covers the SSI for monopile foundations. Finally, section 2.5 gives an introduction into the aspects of seismic loading, with a focus on the seismic behaviour of piles.

2.2.   Monopile Foundations

A huge research effort has been spent on the optimisation of support structures for offshore wind in the recent years. And, although the concept behind a monopile has not changed over the years, new methods and insights have pushed the optimisation of these foundations to a new level.

2.2.1.   Structural Characteristics

The design of a monopile support structure is driven by the requirements for installation, turbine operation, maintenance and lifetime. The conventional monopile support structure consist of the pile and a transition piece that connects the pile to the tower. A typical monopile foundation is presented in figure 1.2. The monopile is a large tubular section, sometimes with integrated transition piece.

The piles are constructed of steel cans and cones which make up the outer shell of the foundation. The tower structure is often provided by the turbine manufacturer and can often not be changed. The substructure designers are therefore challenged to design based on this given structural aspect. The monopile is due to its relatively simple design well suited for mass-fabrication. Nowadays, monopiles with diameters of up to 11 m diameter is claimed to be feasible (102). These new dimensions are necessary to support the next generation of multi-megawatt turbines. Current assumptions are that monopiles can be used in water depths of up to 60 m. However, turbines in deeper water will challenge the feasibility of the monopile, particularly as wave action will increasingly interfere with the dynamics of the turbine structure.

The embedded depth of the monopile depends on the sea and soil conditions on site. The depth is determined by the maximum allowed rotation and deflection of the support structure under extreme weather conditions. The aim is to minimise the depth to safe on steel, while maintaining the stability and required dynamic structural characteristics. Soil related limiting conditions for this type of support structure are the lateral deflection (due to large cyclic loads) and change in the natural frequencies. Both these limiting conditions depend on the soil condition, and to achieve accurate designs a "realistic" SSI model is necessary (73). Owing to the possibility of large variations in soil conditions and water depths across a wind farm site, individually optimised designs for each turbine position

Figure 2.1: Primary steel design process of a monopile foundation from a geotechnical perspective. The vertical flow is the general structural design process and the horizontals are the geotechnical and seismic procedures. (after: (Whyte; 67))
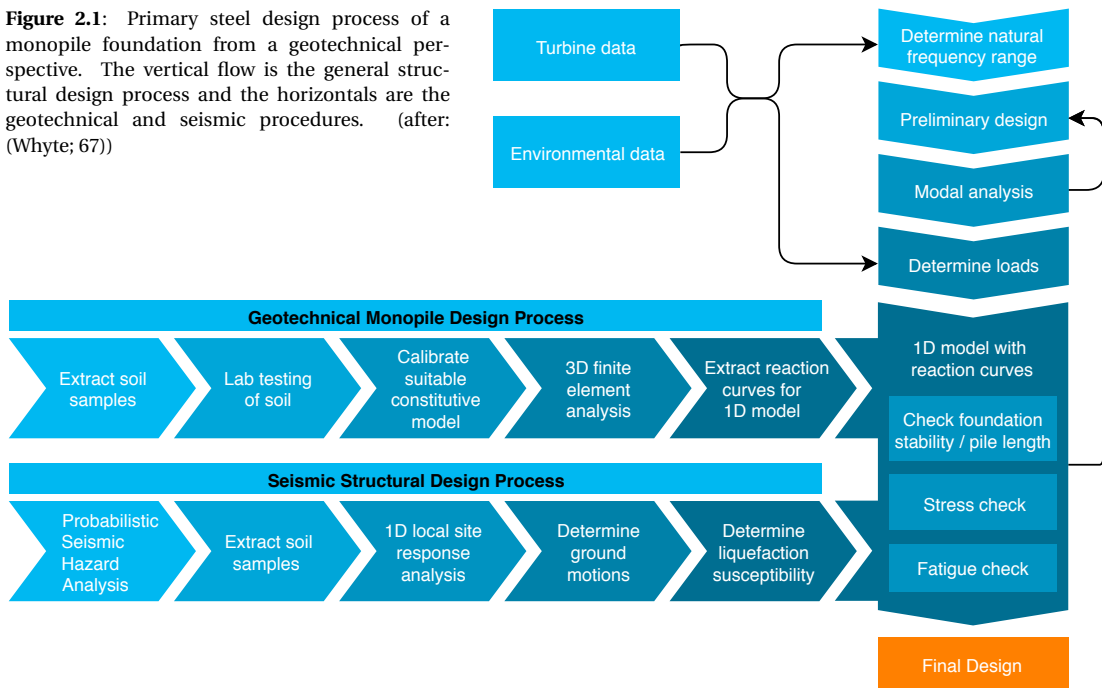
will significantly reduce the amount of steel required for the foundations. There are 3 main structural variables: wall thickness, pile length and pile diameter. Across a site, pile diameters are typically fixed in a number of groups, principally due to the limitations arising from installation and transportation equipment. Therefore, optimisation based on embedded pile lengths and wall thickness is important (55).

2.2.2. The Design Process

The design process of monopile foundations follow a certain strategy that exists of several steps. An example of such a process is illustrated in figure 2.1. The process can be divided into the general structural design flow (vertical flow in figure) and several relevant processes of the sub-disciplines that support the design with data (horizontal flows). The figure shows the sub-processes relevant for a seismic design.

The process starts with the choice of turbine and the investigation of the environmental data. Based on this, a certain design frequency range is established. A typical power spectral density graph with frequency target is shown in figure 2.2. Typically the structure is designed to avoid the forcing wind, wave and 1P/3P frequency ranges. Depending on site specifications, other load types, e.g. earthquakes, are to be considered as well.

The structural dynamics of the tower and monopile can be quite accurately captured with a 1 dimensional beam model. In the present day, the BNWF is a strongly preferred approach in the industry for its quick and reliably performance. The foundation parameters (reaction curves) for the 1D model are usually extracted from a significantly slower full 3D FE model based on a constitutive soil model. The use of the 1D model instead of the full 3D model allows for quick optimisation of foundations across the wind farm site.

The preliminary design is modelled with the Winkler-beam method and tested for various criteria: natural frequency, stability, peak stresses and fatigue performance. The design of a monopile is an iterative process. If any of the criteria fail or shows room for optimisation, the design is updated and checked again.

There is only little experience with the seismic design process of offshore wind turbines as the first large commercial wind farms in seismic areas are being developed only recently. The seismic design process in figure 2.1 is therefore based on the earthquake engineering experience from other fields (67;

Figure 2.2: Typical normalized spectra of actions due to wind, sea waves, and earthquake ground motions. The yellow and orange bands represent the ranges of vibration periods for conventional wind turbines corresponding to main and higher modes, respectively. (source: (25)).
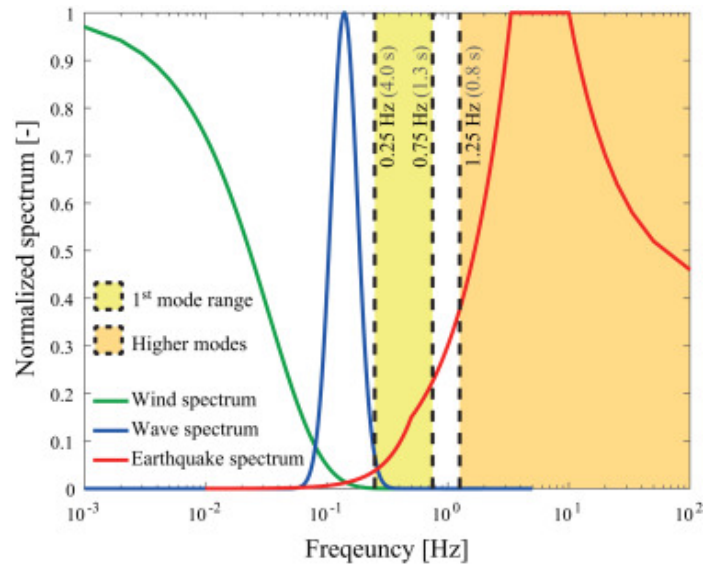
14). First, both the site's earthquake and soil characteristics are to be assessed. This information can be used as model input data to determine the local site response, as will be covered in section 2.5.1.4. The predicted motions of the soil column can be used to determine the liquefaction susceptibility as well as serve as input motions for the seismic loading.

2.3. Fundamentals of Soil Behaviour

This section covers the fundamental aspects of soil mechanics that are important for constitutive soil modelling and earthquake engineering. First, the small-strain soil behaviour is covered. This small-strain regime dictates the wind turbine dynamics under normal operation conditions (112). This is followed by the nonlinear behaviour of saturated sands, which forms the basis for offshore seismic geotechnical engineering.

2.3.1. Small-Strain Soil Behaviour

The stiffness of soil is strongly dependent on the shear strength. For sand like soil types, this shear strength depends on the shear strain in the soil, as displayed in figure 2.3. The shear stress shows an asymptotic behaviour, which relates to a degradation of the shear modulus G for increasing shear strain. When small pile displacements are assumed, the soil response can be considered to be in the small-strain regime where $G = G_{max}$. This regime can be conveniently represented by a linear elastic material. It is found that for the majority of depths and load cases[1], pile deflections remain in this linear elastic regime, therefore dictating the dynamic behaviour of monopile support structures (112).

The elastic behaviour of soil can be described by Hooke's law for isotropic materials:

$$\begin{bmatrix} \Delta p \\ \Delta q \end{bmatrix} = \begin{bmatrix} K & 0 \\ 0 & 2G \end{bmatrix} \begin{bmatrix} \Delta \epsilon \\ \Delta \gamma \end{bmatrix} \quad \text{where:} \quad K = \lambda + \frac{2\mu}{3}, \quad G = \mu \tag{2.1}$$

Where:
K	=	the bulk modulus	(Pa)
G	=	the shear modulus	(Pa)
λ, μ	=	the Lamé parameters	(Pa)

---

[1]This holds for normal operational conditions and not the extreme load cases.
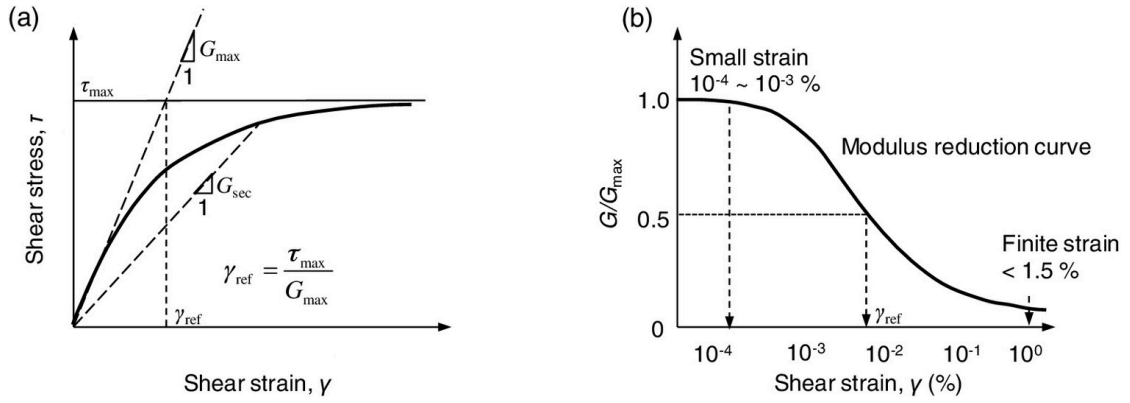
Figure 2.3: The shear strain dependent properties of sandy soils. (a) Typical shear stress-strain relationship; (b) shear modulus degradation (29)

Wave Equation

The 3 dimensional wave equation can be derived from the stress equilibrium of a infinitely small soil section. For brevity, only the derivation in the x direction is presented:

$$\rho \frac{\partial^2 u}{\partial t^2} = \frac{\partial \sigma_{xx}}{\partial x} + \frac{\partial \sigma_{xy}}{\partial y} + \frac{\partial \sigma_{xz}}{\partial z} \tag{2.2}$$

The stress equilibrium can be rewritten in terms of strain as:

$$\rho \frac{\partial^2 u}{\partial t^2} = \frac{\partial}{\partial x}\left(\lambda \bar{\epsilon} + 2\mu \epsilon_{xx}\right) + \frac{\partial}{\partial y}\mu \epsilon_{xy} + \frac{\partial}{\partial z}\mu \epsilon_{xz} \tag{2.3}$$

Substituting the Cartesian stress-strain relations results in:

$$\rho \frac{\partial^2 u}{\partial t^2} = \left(\lambda + \mu\right)\frac{\partial \bar{\epsilon}}{\partial x} + \mu \nabla^2 u \tag{2.4}$$

Two wave equations can be derived from these strain equilibrium equations. These are based on the volumetric and rotational strain components.

1. The first wave equation which is associated with the volumetric strain represents a pressure wave component. The equation of motion (EOM) is obtained by the sum of the strain equilibria derived with respect to its variable:

$$\rho \frac{\partial^2 \bar{\epsilon}}{\partial t^2} = \left(\lambda + 2\mu\right)\nabla^2 \bar{\epsilon} \tag{2.5}$$

2. The second wave equation, which is associated with the rotational strain, represents a shear wave component. To obtain this equation, the stress equilibria are rewritten in the form of the rotation-displacement relations. This relation is achieved by differentiating the stress equilibria with respect to each other and then subtracting the equilibrium in the z direction from that in the y direction. Doing this for the x direction yields:

$$\rho \frac{\partial^2 \Omega_x}{\partial t^2} = \mu \nabla^2 \Omega_x \tag{2.6}$$

The expressions for the wave velocities can be derived from the wave equations 2.5 and 2.6. For the pressure and shear waves these are given by equations 2.7 and 2.8 respectively:

$$V_p = \sqrt{\frac{\lambda + 2\mu}{\rho}} \tag{2.7}$$

$$V_s = \sqrt{\frac{\mu}{\rho}} \tag{2.8}$$

Figure 2.4: Typical critical state line, describing the state of the soil based on the void ratio and mean effective stress.
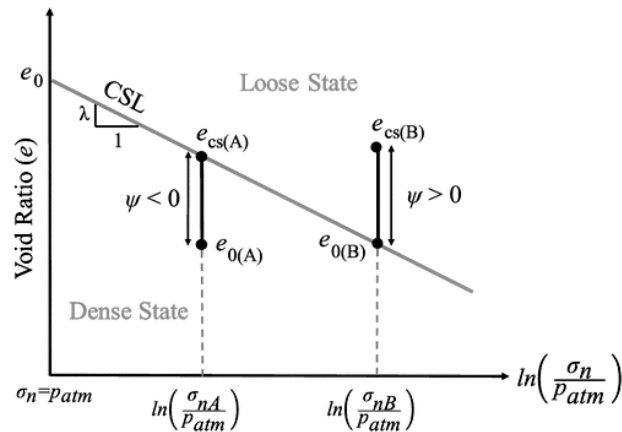
Here:

$\lambda + 2\mu$	=	the P-wave modulus	(Pa)
μ	=	the shear modulus	(Pa)

The shear modulus is an important parameter for modelling the soil stiffness and is therefore required to determine foundation stiffness characteristics. A method to obtain the small strain shear modulus is the seismic cone penetration test (SCPT). This method sends a seismic pulse from a transmitter which is pushed into the earth and measures the pulse at the surface. From this, the shear modulus can be determined using back-calculation methods based on equation 2.8.

2.3.2. Large-Strain Behaviour of Saturated Sands

The zeros on the off-diagonal of equation 2.1 indicate that the volumetric and shear deformations in a linear material are considered to be independent of each other. However, in reality this is not the case. The actual stress-strain behaviour of sand is nonlinear and dependent of various state parameters, e.g. confining stress, void ratio, stress history and others. Critical state soil mechanics uses the condition that sand approaches a continuous state, where no further changes in volume and stress occur, when it is being sheared continuous (98). The states are described by a line, the critical-state line (CSL), which connects all steady-state combinations of stresses and void ratios. The CSL line is presented in figure 2.4. Been and Jefferies (10) introduced the critical state parameter ψ to describe the state of the sand, which is based on the relative void ratios:

$$\psi = e - e_{cs} \tag{2.9}$$

where:

e	=	the void ratio	(-)
e_{cs}	=	the critical state void ratio	(-)

The state of the soil can be divided into loose and dense. When the state parameter of the sand is negative (void ratio below the CSL) the sand is dense of critical, and vice-versa, when the state parameter is positive the sand is loose of critical. The behaviour of the soil in these conditions depends on if the soil condition is drained or undrained. The behaviour for these cases is discussed in the following sections.

Drained Monotonic Loading

If water drains sufficiently quick, volume changes of the soil can occur instantaneous and loads will be carried by the soil skeleton (94). Therefore, the shear strength of uncemented sands is based on the internal friction of the sand grains. A common way of describing the shear strength τ of soils is therefore based on an internal friction angle ϕ and the confining pressure σ'. This is expressed as:

$$\tau = \sigma' \tan(\phi) \tag{2.10}$$

Figure 2.5: Global and local void ratios within triaxial sand test of loose and dense sand. (45)
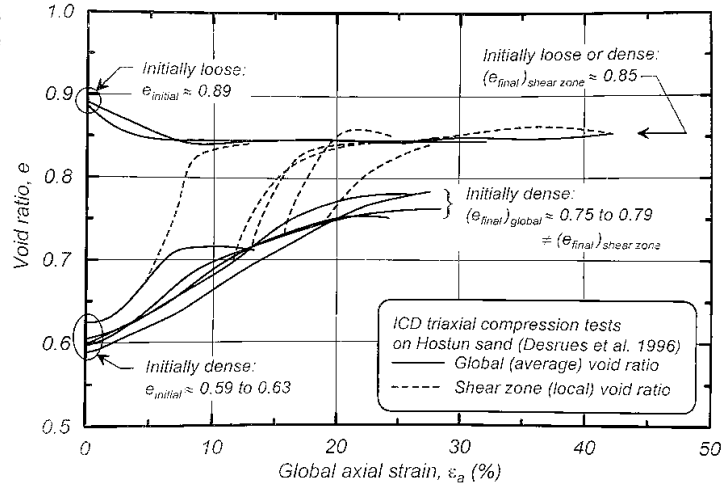
The shear behaviour of drained sand depends on its initial state. Figure 2.5 shows the change in void ratio when sheared. The loose sand is densified during shearing and the volume decreases. The dense sand on the other hand dilates when sheared. This dilation can be seen as the space needed for the sand particles to slide over each other. The void ratios of both the loose and dense sand during shearing approach a final value. This is the value of the CSL for the given confining pressure.

Undrained Monotonic Loading

A loading condition is said to be undrained when the loading rate is larger than the rate of pore pressure dissipation. This occurs in fine grained soils with low permeability or in sands under rapid loading conditions, e.g. earthquakes.

When undrained soil is loaded, the incompressible pore fluid restricts any change in volume. This means that the soil skeleton is not able to carry any load increments as the volumetric strain is unchanged. The hydrostatic component of any additional loads is taken by the pore fluid while the shear strength is unchanged. The undrained shear strength of soils can be expressed as a constant:

$$\tau = s_u \tag{2.11}$$

Note that this equal to equation 2.10 for the effective stress related to the initial undrained volumetric strain.

As the pore fluid is taking up part of the load, the soil can be considered as a two phase medium. From this follows that the stresses are a superposition of the stresses in the soil skeleton and pore fluid. The formulations for the total hydrostatic stress p, the effective stress p' and the deviatoric stress tensor σ^{dev} can be defined as:

$$p = \frac{\sigma_{11} + \sigma_{22} + \sigma_{33}}{3} \tag{2.12}$$

$$p' = \frac{\sigma'_{11} + \sigma'_{22} + \sigma'_{33}}{3} = p - u \tag{2.13}$$

$$\sigma_{ij}^{dev} = \sigma_{ij} - p\delta_{ij} \tag{2.14}$$

Here:

σ	=	the Cauchy stress tensor	(Pa)
u	=	the pore pressure	(Pa)
δ_{ij}	=	the Kronecker delta	(-)

Characteristic undrained behaviour can be understood when the incompressibility is combined with critical state soil mechanics. According to critical state soil mechanics, sand has the tendency to approach a certain relative void ratio under shearing. However, the void ratio of undrained saturated

sands cannot change. The pore fluid will exert a pressure in the opposite direction of the volumetric change the sands wants to undergo in order to maintain a stress equilibrium. When combining equations 2.10 and 2.13, two general situations can be defined:

1. Dense sand wants to dilate when sheared. This dilation results in a negative pore pressure and therefore an increase in effective stress. This increased effective stress results in a higher stiffness and shear strength.

2. Loose sand will have the tendency to compact. However, this compaction is restricted by the pore fluid which will result in an increase in pore pressure. This increase in pore pressure results in an decrease in effective stress and therefore shear strength. When the effective stress approaches zero the pore fluid carries all the load and there is no shear strength left. This phenomenon is called liquefaction.

Drained Cyclic Loading

Environmental loading on offshore structures, and therefore in the soil, is often of cyclic nature. To design a structure for these conditions, it is necessary to account for the significantly different cyclic behaviour of soils. Only the soil characteristics is not enough to describe its behaviour under loading. Also the mode, amplitude and frequency of the cyclic loading influence the response (94).

Cyclic loading of drained sand can cause compaction. The reversal shear stresses result in a restructuring of the sand grains often resulting in densification. The actual densification depends on the magnitude of the volumetric strains, the number of load cycles, the initial relative density, the confining stress (45).

Undrained Cyclic Loading

Undrained cyclic loading has features in common with drained cyclic loading. However, in the undrained situation a volume change is restricted. The soil skeleton tends to compact under cyclic loading transferring loads from the skeleton to the pore fluid. In contrast to many metal plasticity models, soil often has a interaction between shear and volumetric strain (non-zero off-diagonal values in equation 2.1). This means that plastic volumetric change in the soil can be induced by cyclic loading. This plastic volumetric strain can not lead to a volume change and has therefore to be in equilibrium with the elastic strain. This means reduced effective stresses in the soil. Continuous loading at a certain combinations of magnitude and frequency can lead to the complete counteracting of the elastic part by the plastic part. In other words, the sand grains are not in contact with each other anymore and the pore fluid is carrying all the loads.

The ratio between the excess pore pressure and the effective consolidation stress is called the excess pore pressure ratio r_u, defined as:

$$r_u = \frac{\Delta u}{p'} \tag{2.15}$$

This parameter describes the state of effective stress in the soil. There is often referred to $r_u = 1$ as initial liquefaction as this means that the effective stress has reduced to 0. This parameter is a convenient way to keep track of the state of liquefaction in experiments and is often used as input parameter in parametric liquefaction models of soils.

A distinction can be made between two types of liquefaction (45; 67). These types are related to the state of the soil before loading. The liquefaction types are:

• Flow liquefaction. This type of liquefaction occurs in loose-of-critical sands that are loaded. Here, the soil skeleton compacts, transferring its loads to the pore fluid. The new medium state is like a fluid unable to carry any shear forces and will flow like a liquid. This type of liquefaction can occur in both monotonic as cyclic loading.

• Cyclic mobility. This type is associated with cyclic loading of dense-of-critical sands. The cyclic loading compacts the soil leading to a progressive reduction in shear strength. Characteristic to

this type of liquefaction is that when the soil is monotonically loaded after liquefaction, the soil stiffens. This is due to the fact that although liquefaction occurred, the soil is still in a dense-of-critical state. Under monotonic loading the soil dilates, preventing large deformations.

2.3.3. Material Damping

Damping is the dissipation or loss of energy in a system. The main type of damping in soils is hysteretic material damping. This damping is primarily related to shearing and the dissipated energy is equal to the area under a stress-strain diagram. This type of damping is related to the plastic material behaviour. Soils show a degradation of the shear modulus as presented in figure 2.3. The increase in plasticity for larger shear strains would result in larger damping values in the soil.

Based on the theory above, no damping would be expected in the small-strain regime. However, this is not the case. Values of approximately 2% critical damping for soil columns excited in the small-strain regime have been found (67). There is still uncertainty about all the physical mechanisms leading to this damping values in the linear regime. One of the mechanisms is related to the viscous resistance of the ground water flow. The soil is saturated with water at offshore locations. This pore-fluid feels flow resistance when it is expelled from the soil volume during loading. This resistance, and therefore the damping, is related to the permeability of the soil and the viscosity of the pore-fluid. The damping resulting from ground flow is present in both the small-strain as well as in the nonlinear regime (22). It must be noted however that the small-strain damping is also present in dry soils, meaning that viscous damping is not solely responsible.

2.3.4. Numerical Modelling of Undrained Sand Behaviour

The value of earthquake models depends on the accuracy and realism of the soil model. Various attempts have been made to develop soil models that somehow can account for the degradation effects of the soil under loading. Due to the high complexity of soil liquefaction, only empirical models were able to predict liquefaction quite reasonably for a long period of time. When more computational capacity became available, attempts were made to develop constitutive soil models. These models are increasingly effective in the estimation of soil dynamics. However, the high complexity prevents models to accurately describe all soil characteristics. To date, no soil model exists that accurately describes all soil characteristics.

Constitutive Soil Modelling

The development of finite element analysis (FEA) led to the possibility to predict soil behaviour with a numerical model. The calculation method of this finite element method (FEM) is based on the stress-strain relationship. Therefore, the accuracy of the FEA is directly dependent of the used material model. Constitutive models try to capture the mechanics of the soil on a fundamental level. Several physical and theoretical equations are used to describe the behaviour of a single element of soil. Here, a brief overview of their principles and characteristic features is presented. (70)

Most constitutive models are based on theories for elastic and plastic behaviour. The elastic part can generally be described by Hooke's law for isotropic materials (equation 2.1), which often acts as the basis for constitutive models. However, various phenomena such as strain irreversibility, shear/volumetric strain coupling, stress path dependency and strength degradation can not be accurate modelled by only elasticity theory (70). For this reason, constitutive models are extended with a plasticity description. An incremental plasticity formulation exist out of 3 steps:

- Yield function. The loading type is defined by the yield function. When a stress increment $\Delta\sigma$ leads to a stress outside the yield surface, elastic-plastic loading will occur. When the stress decreases or the stress stays within the yield surface, the deformations will be of elastic nature. The stress state can never exceed the elastic domain. When this happens the yield surface has to be updated so that the stress state is on the edge of the elastic domain.

- Flow rule. The plastic deformations are described by the flow rule. Mathematically, the flow rule

is expressed as:

$$d\epsilon^p = d\lambda \frac{\partial g}{\partial \sigma} \tag{2.16}$$

Here:
λ =   the strain increment magnitude   (-)

When g is equal to the yield function, the flow rule is called associative. Otherwise it is called non-associative.

- Hardening rule. The elastic domain changes with plastic deformation. The means that the yield stresses depend on the plastic loading history. Hardening rules describe how the yield surface evolves when plastically deformed. The yield surface is described by the hardening parameters, which are updated after every increment.

2.4. Soil-Structure Interaction

The actual SSI mechanism is a highly nonlinear complicated 3D process where axial and lateral loads are transferred to the soil in different ways. The SSI can be determined with a continuum approach that considers the soil as a 3 dimensional solid. However, as full 3D modelling of the SSI is often demanding and still holds many uncertainties, several methods have been developed for a simplified description of the lateral resistance of piles in soils. This would result in the so called beam on elastic foundation, or beam on Winkler foundation approach. In this method, the pile is considered to be a beam that is supported by uncoupled lateral springs that represent the soil. The accuracy of this method is strongly dependent on how well the springs replicate the lateral soil resistance.

2.4.1. The P-Y Method

The springs used in the beam on Winkler foundation are referred to as reaction curves or P-Y curves. This method not only exists for the lateral displacement, but also for axial and rotational deflections (17). However, only the lateral P-Y variant is considered in this thesis. The load resistance experienced by the pile depends on many factors, e.g. pile diameter and soil type. This means that the reaction curve is simply a description of the lateral resistance and not a physical representation of the SSI. For this reason, the validity of the applied reaction curves should be carefully considered for the intended load situation. The development of P-Y curves for various soil conditions is still an ongoing subject of research.

There are several methods to determine reaction curves. Three often used methods are:

- Using empirical relations provided by design codes and guidelines.
- using a 2D/3D numerical FEA to extract the resistance to pile displacements.
- Back calculating the curves from real, model or centrifuge tests.

The industry standard used to be the first approach, which was initially intended for the slender piles of offshore oil and gas jackets. Nowadays, the use of a 3D model is the recommended approach according to the DNV-GL guideline and often applied within the wind energy sector. Such a model automatically also captures the soil interactions in the depth direction. These models usually take much computational effort and are therefore only used once to extract the P-Y curves for a Winkler-beam model. An advantage of this method is that, although the P-Y springs are applied as uncoupled in the Winkler-beam model, they still hold some non-local information as long as the deflection of the pile can be considered static and is alike the displaced shape of the pile used for the extraction. The third method is mainly applied in academic research, where the focus is more on the reaction mechanism than on a representative foundation description.

Although the reaction curve provides a quick and relatively accurate method for determining the soil resistance, there are several limitations in the use of this foundation representation. Possible limitation would be:

Figure 2.6: Damping component of soil medium for a piled foundation (imaginary component of foundation impedance). Three cases are shown: viscous damping, hysteretic damping and without damping. The significant increase in damping above the cut-off frequency is due to wave radiation. (75)
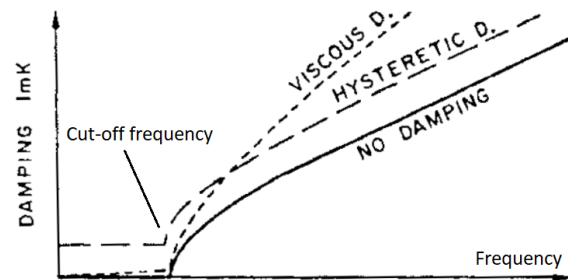
- There is uncertainty in the validity of the reaction curves for large diameter piles. The original method was based on pile tests for relatively slender piles. Test have been performed to validate the reaction curve approach for large diameters.
- A winkler type foundation considers the environment to be rigid, i.e. the uncoupled springs do not take into account the displacement of adjacent springs. In reality however, it is expected that the shearing of soil layers influences the soil reaction.
- The piles do not take time dependent soil response into account. The stiffness of the foundation is considered to be independent of strain rate.

Flexible piles result in local soil displacement while a rigid piles cause a global soil reaction which can often not be accurately captured by considering the soil to be independent layers. Also, the large diameter relative to the depth of rigid piles results in a restoring moment caused by vertical shear stresses at the soil-pile interface (17). (59) mentioned that the use of the additional foundation elements as proposed by (17) might improve seismic analysis of monopile foundations.

2.4.2.   Damping

The structural damping extracts energy from the system resulting in a often beneficial reduction in dynamic response. However, the actual damping values for a monopile founded offshore wind turbine still hold a significant uncertainty. An important damping source, besides the aerodynamic damping from the turbine, is in the foundation. Values of 3% critical damping are found to be appointed to the foundation (113).

The damping in the foundation can be directly related to two phenomenon in the soil: the dissipation of energy in the soil and the carrying away of energy in the form of waves. The damping in soil like materials has been briefly introduced in section 2.3. The damping characteristics of soil can be combined with a P-Y procedure to determine an equivalent Rayleigh damping. This Rayleigh damping is based on a scaled combination of the mass and stiffness matrices to target a damping value for a certain frequency range. The radiation damping component can contribute quite significantly to a system. However, this radiation damping will only be present in the system above a certain cut-off frequency, making the foundation damping frequency dependent. Figure 2.6 shows the damping (imaginary component of the pile impedance) for viscous, hysteretic and no damping cases. All cases show the increase in damping above the cut-off frequency due to radiation damping.

Soil damping estimations are often based on a modal analysis of a platform in the Gulf of Mexico by (19). This paper estimates the contribution of the soil damping by subtracting the other damping types. This approach estimates the soil damping to be around half of the total modal damping.

The contribution of the foundation damping poses a challenge in seismic analysis, as the current knowledge on foundations values for piled foundations is primarily based on measurements and theories for the small-strain soil regime. Therefore, further research is necessary to determine the contribution and influence of damping during an earthquake.

2.5.   Geotechnical Earthquake Engineering

Earthquake engineering is a relatively young discipline, taking off around the time of the earthquakes in Niigata, Japan and Alaska in 1964. After this, the field quickly matured when the development of nu-

clear reactors asked for a better insight into seismic hazards (14). Much research has been performed since, on e.g. earthquake occurrence, load spectra and seismic structural response.

2.5.1.   Ground Motions

In earthquake engineering, a proper description of ground motions is essential. Therefore, this section first covers seismic waves, followed by ground motion characteristics and the ground response analysis.

Seismic Waves

The energy released during a fault rupture is converted into heat and pressure waves propagating away from the source (67). The waves originating from this source are body waves. There are two types of body waves: P-waves (primary/pressure) and S-waves (secondary/shear). The EOM for these two types of waves are derived in section 2.3. P-waves are pressure waves, i.e. the particle motion is parallel to the direction of the wave propagation. Analogous to acoustic waves, P-waves can travel through both solid materials (rock/soil) as liquid materials (oceans/Earth's core) (14). S-waves are shear waves that cause sideways soil deformation, i.e. the particle motion is perpendicular to the direction of the wave propagation. At ground surface, S-waves can produce both vertical (SV) and horizontal (SH) motions. Shear waves cannot travel through liquids such as oceans and the Earth's core, as liquid is unable to transmit shear forces. Also liquefied soil layers will significantly reduce wave amplitude (14). The velocity of a body wave depends on the stiffness and the density of the medium through which they pass. P-waves travel faster than S-waves as soil is generally stiffer in compression than in shear. Therefore, P-waves arrive first at site. The mathematical expressions for the wave velocities are given by equations 2.7 and 2.8.

Surface waves occur when (inclined) body waves interact with a surface, e.g. the surface of the Earth. Rayleigh waves and Love waves are the most relevant types of surface waves for earthquake engineering applications. Rayleigh waves are produced by interaction of P- and SV-waves with the Earth's surface. Rayleigh waves involve both horizontal as vertical particle motions. Love waves are shear waves that that are the result of SH-waves that interact with a soft superficial layer and have no vertical component of motion.

Waves interact with the medium through which they travel. This interaction leads to changes in wave direction, intensity, frequency or even wave type. The types of interaction can be categorised as:

- Reflection
- Refraction
- Diffraction
- Dispersion
- Attenuation

Motion Records

The seismic waves reach the surface of the Earth and produce ground motions at the site. These ground motions can be quite complicated and can be described by the six kinematic degrees of freedom of the soil particles. However, in practice the rotational components are usually neglected and only the three orthogonal translation components are used. Earthquakes are typically recorded as ground motion time histories. This allows for the analysis of various parameters of interest for earthquake engineering. For many engineering purposes is it not necessary to use the exact ground motion time history. The reproduction of the relevant motion characteristics is often sufficient. In engineering, three ground motion characteristics are of primary significance: the amplitude, the frequency content and the duration of the motion. Many other relevant characteristics can be derived from these three.

The ground motions can be described in terms of acceleration, velocity or displacement. The most commonly used measure of the amplitude of a particular ground motion is the peak horizontal acceleration (PHA). The PHA for a given component of motion is simply the largest value of horizontal acceleration obtained from the accelerogram of that component. Horizontal accelerations have

commonly been used to describe ground motions because of their natural relation to inertial forces. Another useful amplitude parameter is the peak horizontal velocity (PHV). Since the velocity is less sensitive to higher-frequency components of the ground motion, the PHV is more likely than the PHA to characterise ground motion amplitude accurately at intermediate frequencies. Its anti-derivative, the peak displacement, is less commonly used as a measure of ground motion.

Frequency Content

Earthquakes result in complicated ground motions that often contains a specific range of frequencies. The frequency content describes how the amplitude of ground motion is distributed among different frequencies. Frequency analysis of earthquake loading holds valuable information since the frequency content of the loading strongly affects the response of the structure.

Any periodic function $x(t)$ can be expressed, using Fourier analysis, as the sum of a series of harmonic terms of different frequency, amplitude and phase. The function can be expressed as:

$$x(t) = c_0 + \sum_{n=1}^{\infty} c_n \sin\left(\omega_n t + \phi_n\right) \tag{2.17}$$

Here:

c_n	=	the amplitude of the nth harmonic	(-)
ϕ_n	=	the phase angle of the nth harmonic	(rad)

The Fourier amplitude spectrum of a strong ground motion shows how the amplitude of the motion is distributed with respect to frequency. The Fourier amplitude spectrum can be obtained from the earthquake time signal. The frequency density function is described as:

$$\hat{f}(\omega) = \int_{-\infty}^{\infty} x(t) e^{-2\pi i x \omega} \mathrm{d}x \tag{2.18}$$

The power spectral density function is another way to describe the frequency content of a signal. Moreover, the power spectral density function is an effective method for stochastic earthquake analysis as it allows for statistical input of the ground motion parameters. To generate artificial earthquakes, the produced stationary random time series is multiplied with a deterministic intensity function. Changes in frequency content during the motion can be described using an evolutionary power spectrum approach.

Earthquakes tend to have a specific site related characteristic when it comes to frequency. This characteristic is based on the local site effects and the wave propagation from the source. On a more general level, earthquake frequency spectra tend to have a specific shape. A typical earthquake spectrum is shown in figure 2.2. Fourier acceleration amplitudes tend to be largest over an intermediate range of frequencies bounded by the corner frequency f_c on the low side and the cutoff frequency f_{max} on the high side. The corner frequency can be shown theoretically (16) to be inversely proportional to the cube root of the seismic moment. This result indicates that large earthquakes produce greater low-frequency motions than smaller earthquakes. The cutoff frequency is not well understood; it is characterised both as near-site effect and as source effect (67) and is usually assumed to be constant for a given geographic region.

Ground Response Analysis

Ground response analyses are used to predict ground surface motions for the development of design response spectra, to evaluate dynamic stresses and strains for evaluation of liquefaction hazards, and to determine the earthquake-induced loads. The ground response analysis used in practice are a simplification of reality. Ideally, a complete ground response analysis should take the following factors into account (35):

- The complete rupture mechanism at the source of the earthquake.
- The propagation of the stress waves through the Earth's crust to the top of bedrock beneath the site.

Figure 2.7: visualisation of the concept behind a local ground response model. The 1D model consists of several soil layers, overlaying the rigid bedrock. (38).
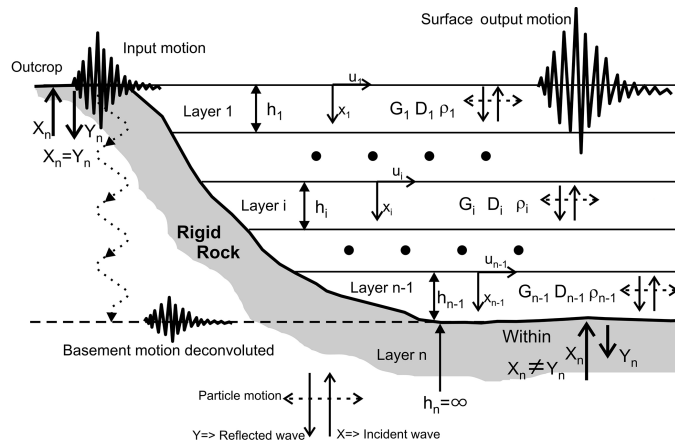
- The influence of the soil characteristics on the ground surface motion.

However, the mechanism of fault rupture is so complex, and the nature of energy transmission between the source and the site so uncertain that this approach is not practical for common engineering applications (67). In practice, the analysis is separated into two parts. On large scale: empirical methods are used to describe history based relations between a fault and a site. These predictive relations are used in e.g. a PSHA analysis to determine the motion characteristics of the bedrock at the site. On local scale: a seismic ground response analysis determines the ground motions in the soil column at the site. This step determines any local frequency amplification effects, which can lead to great differences at different locations. Despite the fact that seismic waves may travel through tens of kilometres of rock, and often through less than 100 m of soil, the soil plays a very important role in determining the characteristics of the ground surface motion (67). A graphical representation of the site response analysis is presented in figure 2.7.

A large variation in ground response motions can be found over relative short distances. It has been recognised that these differences are related to the variations in local site effects. Seismic hazard evaluations have been performed for many earthquake prone areas. These studies shows that the local geology is one of the dominant factors determining the variation of ground motions, and the corresponding seismic hazard (67).

In a one dimensional site response analysis it is assumed that the response of a site is predominantly caused by shear waves propagating in vertical direction through the soil column. When using an linear approach, an analytic expression can be derived for the soil motions. This expression is based on a one-dimensional shear beam:

$$\rho(z)\frac{\partial^2 u}{\partial t^2} = \frac{\partial}{\partial z}\left(G(z)\frac{\partial u}{\partial z}\right) + \frac{\partial}{\partial z}\left(c(z)\frac{\partial}{\partial t}\frac{\partial w}{\partial x}\right) \tag{2.19}$$

Here:

ρ	=	the soil density	(kg/m^3)
G	=	the shear modulus	(N/m^2)
c	=	the damping coefficient	(Ns/m^2)

This linear expression allows for the derivation of a transfer function, which relates the frequency response of the ground surface to the frequency input at the bedrock. An often assumed ratio between outcropping motion and surface motion is 2 as the surface can be considered to be a free end.

In reality, soil behaviour can only be considered linear in the small-strain regime. Severe earthquake loading is not in this regime and the nonlinear modulus reduction (figure 2.3) should be accounted for, as they have a significant impact on the behaviour of soil subjected to cyclic loading (35). It shows that a linear approach is valid for greater depths where the confining stresses dominate over the shear stress. However, near the surface, where the decreasing shear wave velocity and wave reflection result in larger ground motions, the shear strain becomes significant and nonlinear soil behaviour may take place. Numerical methods can be used to determine the possible seismic response of the soil column.

Figure 2.8: Components of soil-structure interaction. The total interaction can be considered as a superposition of the kinematic interaction and the inertial interaction. (109).
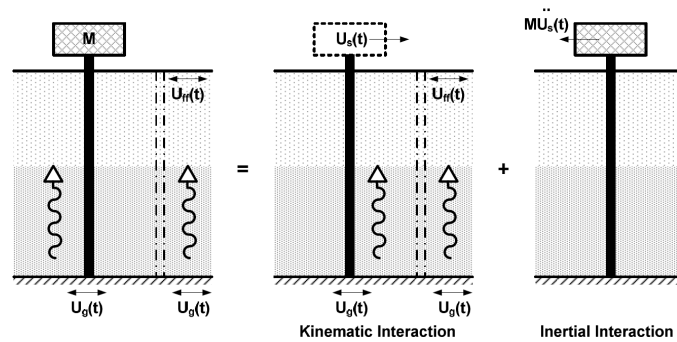
Nonlinear dynamic effects show to be present in reality as earthquake records show a de-amplification of the high frequencies and a shift of the natural frequency of the soil column to the softer region (35). It is also shown that the nonlinear soil response has an effect on the dispersion of the seismic waves.

Site response analyses are often performed deterministic. The parameters for a case of interest are used and kept constant during the analysis. At most, several input ground motions are used when computing nonlinear soil computations to assess the variability of the obtained time histories (35). Probabilistic approaches can be used to e.g. determine the effect of variability in soil properties or perform a site sensitivity analysis. The Monte Carlo method is an effective method to explore model parameters.

2.5.2.   Pile behaviour under Seismic Loading

During an earthquake, the dynamics of a structure are determined by the coupling of three systems: the superstructure, the foundation and the surrounding soil (109). In a SSI analysis, the combined effect of all of these systems are determined to correctly estimate the influence of the dynamics of the soil and the soil-structure interaction. In many civil structures, this interaction is ignored as its effect is considered beneficial or irrelevant. However, the accuracy of the SSI model can have a significant impact in cases where the stiffness of the foundation has a considerable influence on the design lifetime, e.g. wind turbine foundations.

Two physical mechanisms can be distinguished in a SSI analysis of a pile under seismic loading. These mechanisms, as presented in figure 2.8, are:

- Soil-pile kinematic interaction. This mechanism represents the effect of the often stiffer pile element in the soil. The piles resistance to the seismic soil motions results in induced stresses in the foundation and the scattering of the seismic waves.
- Structure-pile inertial interaction. This part represents the inertial interaction between the soil, foundation and the superstructure. This mechanism refers to the D' Alambert forces associated with the acceleration of the complete[2] system (109).

Kinematic Seismic Pile Response

Various pseudo-static analysis methods have been developed to asses the kinematic loading in piles under lateral ground motions. Many of these pseudo-static methods use displacement-based analysis, such as the beam on winkler foundation method. Here, the soils stiffness is represented by springs linking the pile to the displacement of the soil column. A variety of spring types have been developed to account for different soil properties. Also attempts to represent liquefied soil by a springs has been done.

The kinematic pile response neglects any inertial forces. The interaction comes from the stiffness of the pile which resists the soil displacement. This approach is used in codes to asses flow liquefaction which produces a limit lateral pressure on the pile (54).

---

[2]For slender piles under e.g. multistory buildings, the superstructures mass dominates and only the inertial interaction at the piles head is taken into consideration.

Inertia Response of Piles

In reality, the foundation and superstructure have a mass and therefore inertia. Kinematic based soil pile models will not be able to correctly capture any dynamic effects in the analysis. The mass of the structure can be accounted for by applying the inertia loads in the model. A method to implement these is to use impedance equations (86).

Coupling of Kinematic and Inertial Interaction

The kinematic-inertial-decomposition leads to certain uncertainties later, when the kinematic and inertia components of the seismic SSI analysis are combined again. When the two components are separately determined, the uncertainty arises on how to combine the two load combinations. combined load factors can be applied to account for the fact that the peak kinematic and inertial demands may not occur simultaneously (115). Shake table tests show that the inertial and kinematic components are in phase when the natrual period of the structure is less than that of the ground (106). This indicates that the peak stresses obtained from the kinematic and inertia analyses should be combined. The superposition of these components may be approximately valid even in nonlinear soils (32). This is due to that the inertial shear strains induced in the soil occur typically near the surface. While the S-wave induced shear strains on the other hand are more likely to be important at relatively deep elevations.

Methodologies for Soil-Structure Interaction Analysis

Two common methods exist to determine the SSI of a structure. These methods are:

- The direct method.
  In a direct approach, the structure and the soil are considered in the same model. Both are simultaneously calculated in e.g. a numerical solver. The soil is often modelled as solid elements based on a constitutive soil model. The assumption of superposition is not required and true nonlinear analysis can therefore be performed (109). However, to achieve accuracy, a significant soil volume has to be taken into account, leading to large models with high number of nodes. Including the nonlinear behaviour, the direct method often results in computationally demanding models. For this reason is the direct method only applied to deterministic cases and not for e.g. optimisation.

- The substructure method.
  In the substructure approach is the model decomposed into three separate parts, which are later combined to get a full solution. The parts are:

  1. determine the kinematic interaction
  2. determine the foundation impedances
  3. determine the inertial interaction

  This method, which is based on the principle of superposition, is only exact for linear soil and structure behaviour. The method can however be updated for nonlinearities by aplying an iterative procedure (109). The three step method is popular due to its quick computational time compared to the direct method.

2.6.   Summary

In this chapter, a summary of the relevant theory on which the work and models in this thesis are based was presented. The structural characteristics and the design process of monopile foundations was covered in the first section. This was followed by the fundamentals of soil behaviour, which determines the soil motions and SSI during an earthquake. After this, methods to represent this SSI in mathematical models was discussed. Finally, the relevant aspects of geotechnical earthquake engineering were presented.

Chapter 3

3D Seismic Monopile Response Model

3.1.   Introduction

A full 3 dimensional FE model of a monopile embedded in the seabed is developed in order to determine seismic response. This model will act as a basis and validation tool for the investigated methods in this thesis. Section 3.2 presents the characteristics of the monopile and the type of soil used for the analyses in this thesis. This is followed by the formulation of the numerical model in section 3.3. Finally, the behaviour of the model is validated in section 3.4. The model was originally intended to function as seismic analysis model. However, the model is used for static harmonic analysis as well by changing the boundary conditions.

3.2.   Monopile and Site Characteristics

The dynamics of a monopile foundation depends on many factors, such as e.g. the pile diameter and the soil stiffness. For this reason, all the analyses in this thesis are performed for identical situation to be able to assess the results in the same framework. The characteristics of the monopile and location used in the analyses are presented in this section.

3.2.1.   Monopile Characteristics

The monopile is assumed to be a tubular section embedded in a semi-infinite soil half-space. The tower and nacelle are not included in the models as these are not required for the analysis of the foundation's response behaviour. The focus of this thesis is on the seismic performance of the latest generation large diameter monopiles. The monopile considered in the seismic analysis is based on a design by Van Oord for a 9.5 MW wind turbine, as used in the Borssele 3 & 4 offshore wind park. The monopile is designed for a water depth of 30 meters and has an embedded depth of 30 meters. Table 3.1 presents the monopile characteristics as used in the models. The presented values are rounded as the actual monopile details are classified. The pile is simplified by considering a constant diameter and wall thickness over the height.

The monopile is considered to be constructed of S355 structural steel. The material properties as implemented in the model are presented in table 3.2. The steel material model is implemented as

Table 3.1: Geometric characteristics of the monopile

Property	Parameter	Value	Unit
Length	L	80	m
Embedded depth	L_d	30	m
Outer Diameter	D	7.4	m
Wall thickness	t	0.074	m

Table 3.2: Material properties of S355 steel

Property	Parameter	Value	Unit
Young's modulus	E	210	GPa
Poisson's ratio	v	0.3	-
Density	ρ_s	7850	kg/m^3
Yield strength*	σ_y	325	GPa

* $63 < t \leq 80 mm$

25

Table 3.3: Soil material properties

Property	Parameter	Value	Unit
Young's modulus	E	Fig. 3.1	MPa
Shear wave velocity	V_s	Fig. 3.1	m/s
Poisson's ratio	ν	0.3	-
Density	ρ	2038	kg
Friction angle	ϕ	30	deg
Cohesion	c	10	Pa
Dilatancy angle	ψ	0	deg
Permeability*	κ	1E-5	m/s
Soil bulk modulus	K_s'	18	MPa
Water Bulk modulus	K_w'	2.2	GPa

∗ used in the nonlinear two-phase analysis

Figure 3.1: Young's modulus and shear wave velocity profile
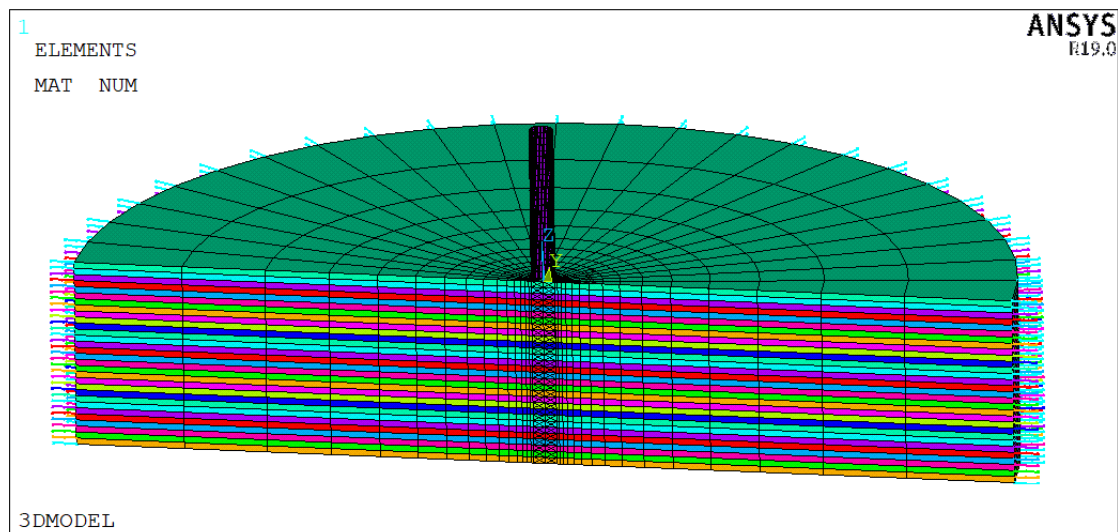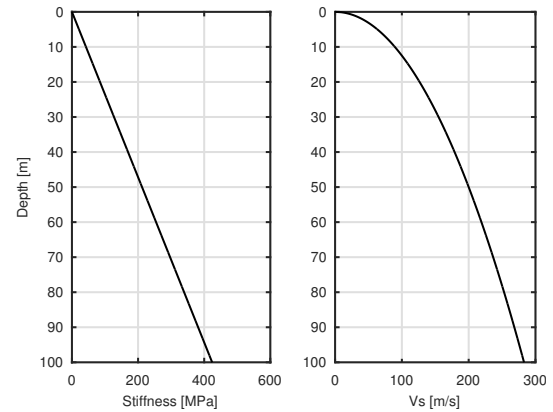
Figure 3.2: An impression of the 3D FE model developed in ANSYS. The coloured layers represent the change of soil properties over the depth. The element differed for various analyses for optimal result.

isotropic linear. Yielding is not considered since plastic deformation is not allowed in the foundation.

3.2.2. Soil Characteristics

The soil parameters used in the models are based on a representative fictional location. The complete soil column is considered to be of a clean sand type. The soil characteristics as implemented in the models are presented in table 3.3.

The stiffness of the soil is usually a function of, among others, the confining stress. This results in a variation of the stiffness over the depth. In this thesis is an actual relation between the confining stress and the stiffness ignored and a linear function is chosen to represent the soil stiffness. The variation of the stiffness and the corresponding share wave velocity are presented in figure 3.1.

3.3. Numerical Model

The model exists of a tubular cross section embedded in a soil half-space. The visualisation of the model by ANSYS is presented in figure 3.2. The model makes use of a symmetry plane for reduced computational effort. The monopile dimensions are presented in table 3.1 and the radius of the soil volume is 40 times the monopile radius. The height of the soil volume is taken as 2 times the embedded depth of the monopile. The model characteristics are discussed in the following subsections.

(a) Linear plane element (4-node)   (b) Linear solid element (8-node)   (c) Linear shell element (4-node)

(d) Quadratic plane element (8-node) (e) Quadratic solid element (20-node) (f) Quadratic shell element (8-node)
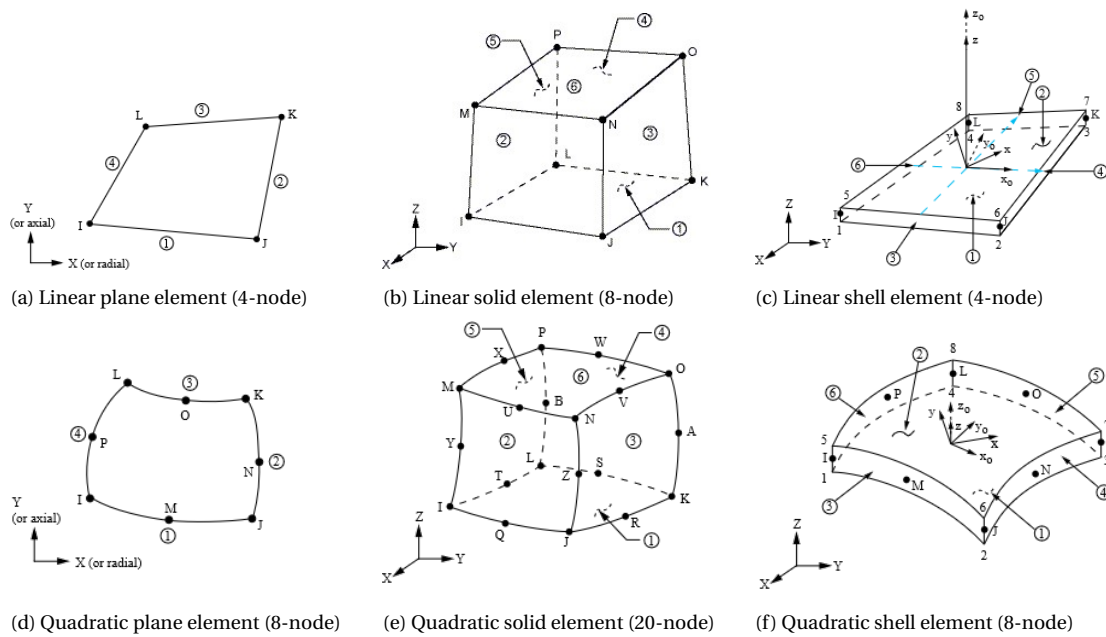
Figure 3.3: ANSYS' element geometries. (6)

3.3.1.   Element Types

The soil has been modelled using two types of elements. The element choice is based on the type of analysis: small-strain or nonlinear soil regime. On top of this are both linear as well as higher-order elements used in the different analysis. The two types are:

1. The linear small-strain analysis is performed with regular solid elements. ANSYS provides this element as first order SOLID185 element with linear displacement behaviour or as higher order SOLID186 element with quadratic displacement behaviour. The element nodes each have 3 translational degree of freedom (DOF) (x,y,z).

2. The non-linear analysis is performed with coupled pore-pressure mechanical solid elements. Again, ANSYS provides this element as first order CPT215 element with linear displacement behaviour or as higher order CPT216 element with quadratic displacement behaviour. The element nodes each have 3 translational DOF (x,y,z). The corner nodes have a additional pore-pressure DOF. The theory behind the coupled pore-pressure mechanical elements is covered in section 5.5.1.

The geometries of the regular solid and the coupled pore-pressure mechanical solid are identical. The geometry of the linear elements is mode up of 8 corner nodes as presented in figure 3.3b. The higher-order elements make use of an additional 12 midside nodes. The geometries of the higher order element types is presented in figure 3.3e. The soil volume is primarily[1] meshed with the cubic shape option, as these provide the highest accuracy.

The monopile is meshed with ANSYS' first-order SHELL181 or higher-order SHELL281 element. These are shell elements based on the Mindlin-Reissner shell theory. The elements nodes each have 3 translational DOF (x,y,z) and 3 rotational DOF (xx,yy,zz). Shell elements are suitable for analysing thin shell structures, e.g. a monopile. The geometries of the SHELL181 and SHELL281 elements are presented in figure 3.3c and 3.3f respectively.

The choice between linear or higher-order elements depends on various factors. Usually, higher-order elements are preferred in structural analysis as they support curved shapes (quadratic shape functions) and solve issues such as shear locking. However, for some situations the linear element types result in higher accuracy. The linear elements are considered in this thesis for the following reasons:

---

[1]Completely meshed with the cubic shape option in case of plastic material behaviour or linear elements.

1. Linear elements are usually preferred for nonlinear analysis (6). Linear elements and quadratic elements have the same number of integration points. Therefore, a fine mesh of linear elements usually results in a better accuracy at less computational expense then a comparable coarse mesh of quadratic elements.

2. The use of higher order elements with midside nodes is not recommended for analysis were wave propagation is of interest (6). Elements with midside nodes have non-uniform mass distribution which can lead to wave distortions.

When using the linear elements, the degenerate forms and highly distorted element shapes should be avoided.

3.3.2.   Mesh Size

The mesh size of the soil and monopile are limited by the computational demand of the model. The soil volume requires a large quantity of elements to accurately describe the soil structure interaction and local material plasticity. Mapped meshing was used to generate a cylindrical symmetric mesh of cubic elements for the soil. The mesh densities were chosen in such a way that the number of nodes remained under 60.000, as this resulted in a satisfactory computational time. Based on the restriction of the number of nodes, the mesh for the linear elements resulted in 24 elements around the circumferential of the pile with an element height of 0.5 m, and the mesh for the quadratic elements resulted in 16 elements around the pile circumference with an element height of 1.0 m.

The monopile has the same mesh size as the soil at the soil-pile interface. It is recommended that 3D flat shell elements do not extend over more than 15 degrees of an arc (6). This requirement is satisfied with the chosen mesh.

For accurate results, the maximum element size should be smaller than a tenth of the wave length (93). E.g. for a maximum frequency input of 10 Hz in a soil with a shear wave velocity of 50 m/s, the maximum element size in the soil column should be 0.5 m or less in the direction of wave propagation. This requirement is not fulfilled with the chosen mesh densities for the less stiff soil strata near the surface.

3.3.3.   Boundary Conditions

Three types of boundary conditions are defined in the model. These boundary conditions can be categorised as the far field and the symmetry plane boundary conditions.

Far-Field Boundary Condition

The far-field outer radius of the soil is represented as a non-reflective viscous boundary layer. This layer is modelled by linear viscous dampers that absorb the radiating wave energy, resulting in a computationally "infinitely" far boundary. The damping constants are based on the Lysmer-Kuhlemeyer (84) boundary conditions:

$$f_p = -\rho_s V_p \frac{\partial u_r}{\partial t} \tag{3.1}$$

$$f_s = -\rho_s V_s \frac{\partial u_\theta}{\partial t} \tag{3.2}$$

where:
f_p, f_s	=	the pressure and shear wave tractions	(N)
V_p, V_s	=	the pressure and shear wave velocity	(m/s)

The Lysmer-Kuhlemeyer viscous boundary condition in its presented form is only applicable to linear materials. However, the boundary conditions is used in both the linear and nonlinear analysis. The use of the element is permitted under the assumption that the strains are reduced to the small-strain regime due to attenuation. Therefore, the far-field boundary should be placed far away enough from the pile.

Symmetry Plane

Symmetry conditions apply at the symmetry plane of the model. No additional constraint is required for the pore pressure DOF as the symmetry axis will acts as an impermeable boundary.

3.3.4. Soil-Pile Interface

The contact between the surface of the monopile and the soil has been modelled in three ways:

1. Direct contact. This method couples the nodes of the the piles shell elements with the soil element nodes at the soil-pile interface.

2. Modified soil-element contact. This method uses different material parameters for the elements surrounding the monopile. The interface material parameters account for difference in friction between the sand and the steel pile and the different contact response. The exact value for the stiffness in this surrounding layer is hard to estimate as it is influenced by e.g. densification due to pile driving or loosening due to reduced soil-pile contact.

3. Contact elements. These elements are meshed over the outer surface of meshed areas or volumes, and keep track of the contact status at every time step. Several contact definitions are possible withing ANSYS to describe different situations. Two contact options have been implemented for the soil-pile contact surface. The first option is compression - no tension with Coulomb friction, and the second option is compression - capped tension with coulomb friction. The capped tension can be interpreted as possible generated negative pressure between the pile and the soil. The accuracy of the contact elements showed to be strongly dependent on the mesh size. The 2D plane strain model showed to be working fine with the contact elements, as circa 100-160 elements where used to model the half-circumferential interface between the soil and the pile. However, the full 3D seismic response model showed inaccurate and unwanted behaviour while using the contact elements. Due to the computational limitation of this model, only 12 elements spanned the half-circumference of the pile-soil contact. The model showed unrealistic contact pressures and shear forces. This could be due to insufficient possibility for load redistribution in the relatively large elements, but this was not further looked into.

   The use of contact elements resulted in convergence issues related to the iterative penalty method used in the analysis of the contact elements. The gravity induced pressure in the soil column pushed the soil through the pile wall at the soil-pile interface. The lack of lateral support of the soil resulted in vertical displacement leading to additional down-drag forces at the soil-pile interface. Unrealistically large penalties were required to reduce the penetration to acceptable levels, which resulted in convergence issues.

3.3.5. Run Set-up

The simulation with nonlinear material parameters requires a specific procedure before the actual monopile response analysis can be performed. This is due to the problem that incorrect loading of nonlinear materials in the time domain can lead to unwanted irreversible effects. The necessity for the run set-up in this model is due to the two-phase material model (discussed in detail in section 5.5.1) and the contact elements describing the soil-pile interface.

In the case of a nonlinear analysis, the procedure of a run set-up is as follows:

1. Preprocessor

   - build the model
   - apply dummy soil material with high permeability
   - apply pre-stress

2. Set-up

   - apply pore-fluid gravity[2]

---

[2]Gravity in a two-phase system is considered independent of the structural gravity and needs to be accounted for by the SSOPT

        • apply structural gravity
        • Wait for system to settle
        • apply actual soil material
        • Wait for system to settle

3. Perform analysis

3.4. Validation

The full 3D ANSYS FE model is validated for the static case by comparing it to the response of a similar model developed by (112). The model developed by Versteijlen is a linear elastic finite element model of a embedded monopile, also in the FE software ANSYS. The model is fully linear, as the his research focuses on the identification of effective 1D soil models for large diameter monopiles within the soil's small-strain regime.

The 3D seismic response model as presented in this section is modified to be similar to Versteijlen's model. The considered monopile (MP45) is embedded 24 m in the soil and has a diameter of 5 m with a constant wall thickness of 50 mm. The considered soil volume has a vertical dimension of 50 m and a radius of 40 times the pile radius. The soil parameters were obtained from cone penetration test (CPT) tests (SCPT45) and can be found in the Phd covering the model (112). A horizontal load of 1 N is applied at the top of the monopile, which is located 9.85 m above the mudline.

Figure 3.4 shows the monopile's displacement and cross-section angle (Timoshenko beam constants) as a function of depth. The values are for static loading generated by the model presented in this chapter and the model developed by (112). The two models show a near identical response, especially for the displacement and the cross-section angle, validating the model. The derivatives produced with the model as presented in this section show some deviations (y') and numerical jumps (ϕ'). The origin of the jumps was traced back to the ANSYS model, were the cause could not be identified.
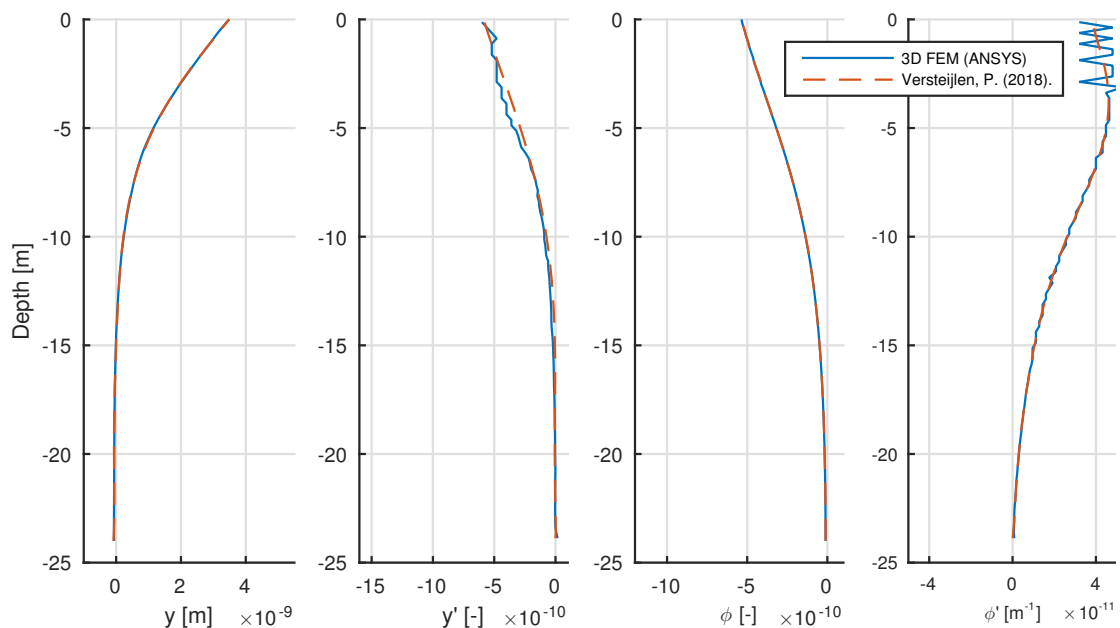
Figure 3.4: Comparison between the Developed seismic monopile response model and the model developed by (112). The figures show from left to right the displacement, slope, angle and curvature of the monopiles. The presented values are obtained for a static horizontal load of 1 N at the top of the monopile, at 9.85 m above the mudline.

The displacement, y, is determined as the average lateral displacement of the two outermost elements in the pile. The cross-section rotation, ϕ, is obtained from the FE model as the difference between the

option in ANSYS.

vertical displacements of the two outermost elements of the pile divided by the diameter of the pile. Their derivatives are numerically obtained as approximate partial derivatives in MATLAB.

3.5.   Summary

In this chapter, a 3D seismic monopile response model was presented. The model was developed in the FE software ANSYS, and consists of a monopile embedded in a soil medium. Only half of the monopile and soil is modelled due to the symmetry of the situation. The model is full 3D and is meshed with shell and solid elements for the monopile and soil respectively. The model is used for the validation and tuning of the 1D Winkler foundation developed in this thesis.

Chapter 4

Seismic Winkler-Beam Model

4.1.   Introduction

This chapter presents the development of a 1D seismic Winkler foundation that can be used to determine earthquake loading on monopile foundations. First, the ground response model is presented in section 4.2. This is followed by the numerical formulation of the combined ground response and Winkler-beam model in section 4.3. Methods to implement the ssi in such a seismic response model is covered in section 4.4.

4.2.   Ground Response Model

The loading in a seismic analysis originates from ground motions. Therefore, to be able to accurately determine any seismically induced loads on a monopile, a proper description of the ground motions is required. To determine the ground motions at a certain location a PSHA can be performed. Databases with large sets of recorded earthquakes are available online.

If the variation of ground motions over the depth of the foundation are of interest for the seismic analysis, a seismic ground response model can be used to determine these subsurface ground motions. The local ground response model has been introduced in section 2.5.1.4. The soil column is modelled as a shear beam, fixed to the bedrock at the bottom and having a free end at the Earth's surface. The beam model is capable of determining the stresses and strains in the soil due to seismic waves[1]. Various (commercial) software exists for this purpose. However, this thesis uses a self-developed 1D local ground response model. In the first place to be able to real-time link boundary conditions of the 3D model to the far-field motions as determined with the 1D ground response model, and secondly due to the unavailability of the commercial software.

The 1D ground response model has been developed in both ANSYS and MATLAB. The model has a simple geometry consisting of only one vertical beam representing the soil column. An impression of the soil column as modelled in the ANSYS models is presented in the figures 4.1 and 4.2. Semi-empirical or constitutive soil models can be used to determine the behaviour of the soil column for shear and pressure waves[2]. A variation of the soil parameters over the height allows for the modelling of different soil strata. The model characteristics are discussed in the following subsections.

4.2.1.   Soil Model

The behaviour of the soil column is determined by the material model used to represent the soil. The situation is simplified by assuming that there is no variation in soil characteristics in the horizontal plane, leading to the reduction of the model to 1 dimension. The only property required for the dynamic analysis is the shear modulus, since only shear waves are considered. The shear modulus is a

---

[1] Limited to vertically travelling P- and S-waves
[2] This thesis only considers shear waves.
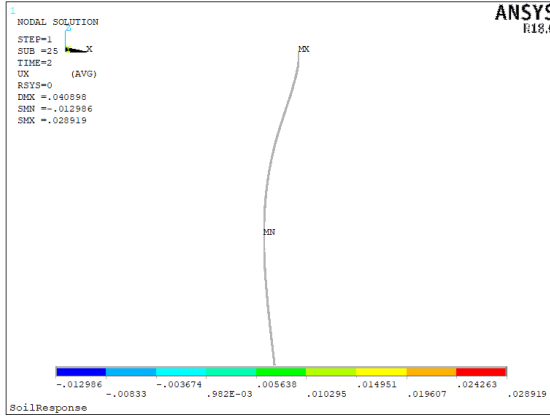
Figure 4.1: Impressions of the spring-mass-damper version of the local ground response model.
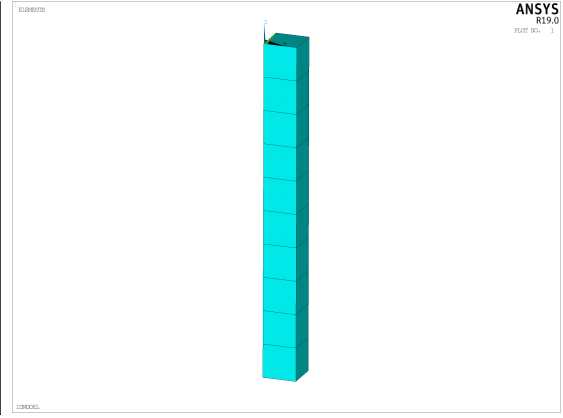
Figure 4.2: Impression of the volume element with constitutive soil model version of the local ground response model.

function of several parameters, as discussed in section 2.3. The semi-empirical formulations used to capture the cyclic characterisation of liquefiable sands are presented in the following sections.

Estimating Pore Pressure Build-up

Semi-empirical models have been developed by several authors to estimate the state of the soil. These formulations are usually fitted to experimental data. The formulations are based on certain soil or dynamical parameters which have been identified to be correlated to liquefaction. Empirical models often predict the excessive pore pressure in the sand by the pore pressure ratio (equation 2.15). This ratio can be related to shear strength or directly used for effective stress reduction. There have been several approaches in defining parameters for empirical models. Two methods have been applied in the ground response models: a cyclic ratio dependent model and a energy based model. Stress based models are not covered in this thesis.

- Cyclic ratio dependant models. Here, the buildup of pore pressure is related to the number of loading cycles and the number of equivalent cycles needed to initiate liquefaction[3]. As one was interested in determining the liquefaction susceptibility of actual locations, the model parameters of this type were often related to data from the standard penetration test (SPT) and CPT. The models were often fitted to field observations which could be linked to the number of cycles from recorded earthquake histories. One of the earliest models of this type was developed by (100):

$$r_u = 0.5 + \frac{1}{\pi} arcsin(2\left(\frac{N}{N_I}\right)^{1/\alpha} - 1) \tag{4.1}$$

Here:
N	=	the number of cycles	(-)
N_I	=	the number of cycles till initial liquefaction	(-)
α	=	a fitting parameter	(-)

Liquefaction models based on cyclic ratio are still in use, by e.g. Deepsoil (1).

- Energy based models. (36) developed the GMP (Green, Mitcher, and Politio) model for cohesionless soils. This model predicts the pore-pressure buildup based on the dissipated plastic energy as reference parameter. The relation between the work and pore pressure ratio is expressed as:

$$r_u = \sqrt{\frac{W_s}{PEC}} = \alpha W_s^\beta \tag{4.2}$$

---

[3]Note that this method is in many ways analogous to the nominal stress method in the fatigue prediction of steel.

Figure 4.3: Example of (A) excess pore-pressure build-up and (B) backbone degradation during cycling loading of Santa Monica Beach sand by (77).
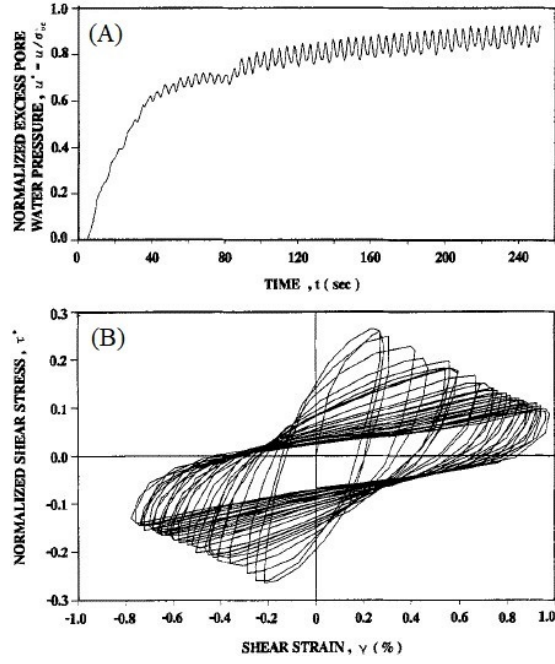
The dissipated energy, W_s, is defined as the area under the stress strain graph. The *PEC* parameter is called the pseudo energy capacity. This value has to be fitted to data or can be estimated from the relative density D_r.

Nonlinear Cyclic Soil Degradation

The nonlinear response of saturated sands during earthquakes is a combination of several phenomena. One of these phenomena is the shear strength reduction due to pore pressure build-up, for which empirical estimation functions are presented above. The (cyclic) shear resistance can be conveniently described by shear strength, τ, versus shear strain, γ. The pore-pressure build-up results in a shear strength reduction due to the decrease in effective stress. A typical change in shear strength due to pore-pressure build-up for sand is presented in figure 4.3.

The cyclic degradation of the soil can be constructed from the backbone curve. The strength reduction is obtained from the degradation of the initial backbone curve due to e.g. pore-pressure build-up. A hyperbolic function to describe the stress strain curve for undrained sand was proposed by (64). Later, (47) added two constant for improved accuracy. The expression then takes the form of:

$$\tau = \frac{G_0 \gamma}{1 + \beta \left(\dfrac{G_0}{\tau_0} \gamma \right)^s} \tag{4.3}$$

where:

G_0	=	Initial shear modulus	(Pa)
γ	=	Shear strain	(-)
τ_0	=	Maximum shear strength	(Pa)
β, s	=	Curve fitting constants	(-)

The stress-strain behaviour during cyclic loading is described by the degradation of the backbone curve formulation in equation 4.3. This is achieved by introducing a pore-pressure based reduction factor. The adopted method in this thesis follows the expressions as given by (77):

$$G_m = G_0 \sqrt{\frac{\sigma_c - u}{\sigma_c}} = G_0 \sqrt{1 - r_u} \tag{4.4a}$$

$$\tau_m = \tau_0 \frac{\sigma_c - u^v}{\sigma_c} = \tau_0 (1 - r_u^v) \tag{4.4b}$$

Figure 4.4: Example of (A) backbone degradation as a function of excess-pore pressure and (B) the change in strain-stress diagram due to pore-pressure build-up. (77)
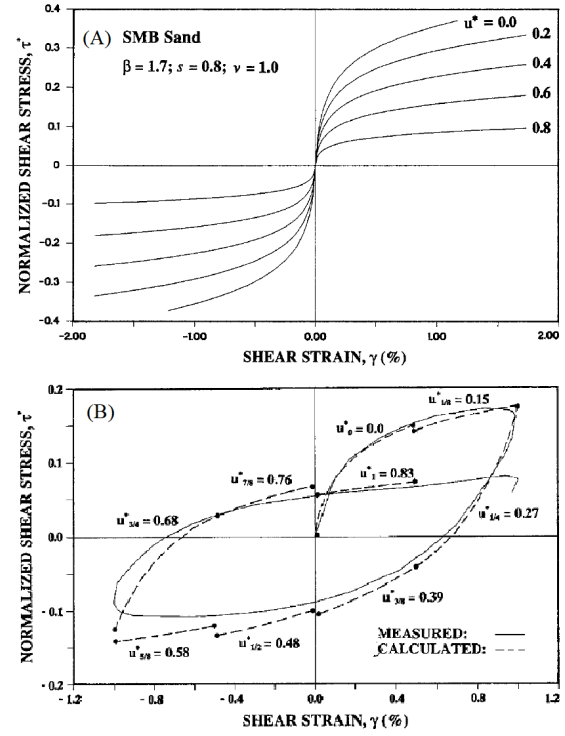
where:

σ_c	=	Confining stress	(Pa)
u	=	residual pore-pressure	(Pa)
v	=	Pressure dependent fitting constant	(-)

The behaviour of the cyclic soil degradation model is presented in figure 4.4. The upper pane presents an impression of the degradation of the backbone curves for Santa Monica beach sand parameters. Increasing the excess pore-pressure leads to a decrease in shear strength. The lower pane shows a cycle modelled with the pore pressure dependent shear strength formulation as presented in this section. The model uses a cyclic implementation:

1. Determine displacements
2. Determine pore-pressure build-up
3. Update soil parameters
4. continue to next time step

The backbone curve reduction method as presented by (77) can be extended to account for confining pressure effects. The expression proposed by (40) uses fitting parameters, *a* and *b*, and a reference confining pressure. They replace the initial sub-grade modulus over max shear strength ratio term in the denominator of equation 4.3:

$$\frac{G_0}{\tau_0} \rightarrow a \left(\frac{\sigma'}{\sigma_{ref}} \right)^{-b} \tag{4.5}$$

4.2.2.   Element Types

The MATLAB model uses discretised shear beam elements based on equation 2.19. The nonlinear behaviour and the pore pressure buildup effect are incorporated into the model by updating the soil parameters in the numerical ordinary differential equation (ODE) solver.

The two ANSYS models are based on different modelling concepts and use different element types:

- The shear beam variant as presented in figure 4.1 uses non-linear springs based on the soil degradation formulation as presented in the section above. ANSYS provides nonlinear springs

as COMBIN39 elements. This is a unidirectional spring element, based on nonlinear force-deflection capabilities with Masing effect.

The COMBIN39 element has a few downsides when it comes to nonlinear dynamic analysis. The spring resistance can not be changed and the element can not be turned on or off during a transient analysis. A solution to this was to use linear COMBIN14 spring elements which have the option to be changed during a analysis. A linear and nonlinear spring were implemented in series, where the linear spring had either a really large stiffness (nonlinear spring activated) or a zero spring stiffness (nonlinear spring deactivated). Since the springs could only be on or off, the degradation of the backbone curve could only be modelled step-wise. The size of the steps is determined by the number of spring connections between beam nodes. E.g. 20 spring connections result in a step of 5% soil degradation per deactivated spring connection.

- The shear beam variant as presented in figure 4.2 uses a regular solid element or a two phase mechanical-pore fluid element. The FE software ANSYS provides these element types as SOLID185 and CPT215 (linear), or SOLID186 and CPT216 (quadratic). These elements were previously discussed in chapter 3 and their geometries are presented in figure 3.3. The soil column is meshed with full cubic brick elements, as these provide the highest accuracy for the considered situation.

4.2.3. Mesh Size

The mesh sizes for both the ANSYS and the MATLAB models are based on Cook's approximation (93). For accurate results, the maximum element size should be smaller than a tenth of the wave length[4], e.g. for a maximum frequency input of 10 Hz in a soil with a shear wave velocity of 50 m/s, the maximum element size in the soil column should be 0.5 m or less in the direction of wave propagation.

The bedrock layer can be situated quite deep in the Earth's crust, resulting in large models. To minimise the computational time of the local site response model, the mesh size can be varied over the height. The element size is chosen as a function of soil parameters and maximum loading frequency, which usually results in a course mesh at the bottom as the shear wave velocity increases with depth. A finer mesh is preferred at the top of the soil column since the shear wave velocities here are lowest, and the model has to accurately capture the reflection of the wave at the surface.

4.2.4. Boundary Conditions

The boundary conditions applied in the model are based on the uniform behaviour of a horizontal soil layer, i.e. all points in a horizontal plane at a specific height have identical motions. This is implemented in ANSYS by restricting any nodal rotations and coupling all the nodal translations at the horizontal planes.

The seismic excitation is implemented as forced ground motions at the bedrock level. This excitation can be applied in different ways: as displacement, velocity or acceleration of the bedrock layer. ANSYS provides the options for for forced displacement and velocity.

The top of the soil column is considered to be a free end and has no additional boundary conditions.

4.3. Seismic Winkler-Beam Model

The model exists of a single beam representing the monopile. The model is illustrated in figure 4.5. The soil structure interaction is modelled by springs or more elaborate macro-elements. The model characteristics are discussed in the following subsections.

---

[4]This approximation is based on the use of first-order elements.

Figure 4.5: Impression of the combined ground response model and Winkler-beam model for seismic analysis. (source: unknonw)
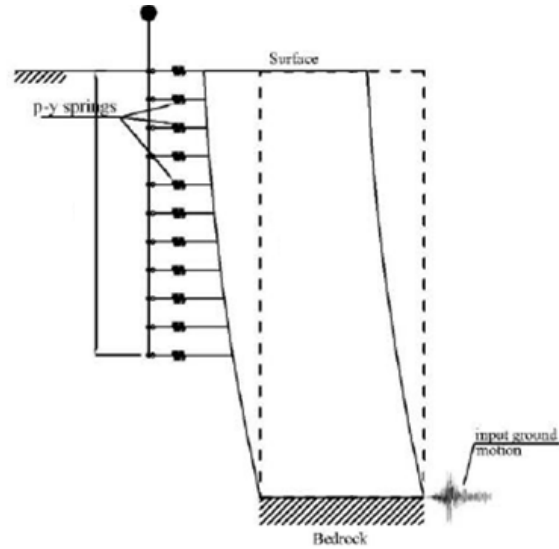
4.3.1.   Element Types

The monopile is modelled as a discrete Timoshenko beam. The choice for this element type is based on the monopiles relatively large area moment of inertia to shear area, resulting in a combination of both shear and bending deformations. The Timoshenko beam couples these shear and bending deformations, implementing shear stiffness and rotational inertia into the EOM. These additional variables allow the cross-section to have a angle φ relative to the neutral axis of the beam. The EOM for a Timoshenko beam are based on the shear and moment equilibrium and can be expressed as:

$$G\kappa A\left(\frac{\partial^2 y}{\partial z^2} - \frac{\partial \varphi}{\partial z}\right) - \rho A\frac{\partial^2 y}{\partial t^2} - py + q(z,t) = 0 \tag{4.6a}$$

$$G\kappa A\left(\frac{\partial y}{\partial z} - \varphi\right) - \rho I\frac{\partial^2 \varphi}{\partial t^2} + EI\frac{\partial^2 \varphi}{\partial z^2} = 0 \tag{4.6b}$$

where:

E, G	=	the moduli of elasticity and shear	(-)
A, I	=	the cross section area and moment of inertia	(-)
κ	=	the Timoshenko shear coefficient	(-)
p	=	the foundation stiffness	(-)

ANSYS provides circular Timoshenko beam elements that account for shear deformations effects as PIPE289 elements. This element is a quadratic three-node pipe element. The element has three translational dof (x,y,z) and 3 rotational DOF (xx,yy,zz) at each node.

In MATLAB the Timoshenko beam elements are defined through matrix formulation. The continuous partial differential equations 4.6a and 4.6b have been discretised into a 6 DOF matrix format by (88), which can be found in appendix A. The matrix form of the Timoshenko beam accounts for the coupling between bending and shearing through a pre-defined coupling parameter:

$$P_c = \frac{12EI}{G\kappa Al^2} \tag{4.7}$$

A discretised beam based on the Timoshenko beam model shows for short elements more accurate results. Note that for long beams, the Timoshenko beam acts as Euler-Bernoulli beam. Therefore, the use of the Timoshenko beam elements is valid for both situations.

The foundation is modelled with macro-elements. These are discussed in further detail in section 4.4.

Figure 4.6: The frequency dependency of the wave numbers for the considered monopile as represented with a dispersive beam on linear Winkler foundation. the variable p represents the foundation stiffness. Only a single wave mode is presented as the cut-off frequency of the other mode is above the considered frequency range.
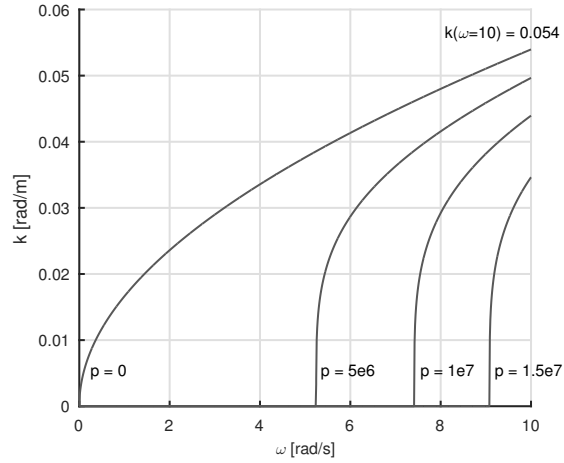
4.3.2. Mesh Size

The seismic Winkler-beam model is 1 dimensional and only the length of the elements in vertical direction have to be determined. The mesh size of the ground response model was already covered in section 4.2. The mesh for the monopile is based on the same principle. However, in contrast to the shear beam formulation of the ground response model, the Timoshenko beam formulation leads to wave dispersion. I.e. the wave length is not linearly proportional to the frequency.

The two partial differential equations 4.6a and 4.6b can be rewritten as a single expression by substituting the differentiated parts. Assuming no forcing, $q = 0$, the expression becomes:

$$EI\frac{\partial^4 y}{\partial z^4} - \rho I\left(1 + \frac{E}{\kappa G}\right)\frac{\partial^4 y}{\partial z^2 \partial t^2} + \frac{\rho^2 I}{\kappa G}\frac{\partial^4 y}{\partial t^4} + \rho A\frac{\partial^2 y}{\partial t^2} + py + \frac{\rho Ip}{\kappa GA}\frac{\partial^2 y}{\partial t^2} - \frac{EIp}{\kappa GA}\frac{\partial^2 y}{\partial z^2} = 0 \qquad (4.8)$$

The dispersion relation can be found by substituting $y = Ye^{i(kx-\omega t)}$:

$$EIk^4 - \rho I\left(1 + \frac{E}{\kappa G}\right)k^2\omega^2 + \frac{\rho^2 I}{\kappa G}\omega^4 - \rho A\omega^2 + p - \frac{\rho Ip}{\kappa GA}\omega^2 + \frac{EIp}{\kappa GA}k^2 = 0 \qquad (4.9)$$

The wave lengths corresponding to certain frequencies are found by solving for the roots of the dispersion relation. Figure 4.6 shows the wave numbers as a function of frequency for the monopile and soil situation as presented in section 3.2. Only one of the two physical roots is shown. The four lines show different foundation stiffnesses, with $p = 0$ representing an unsupported Timoshenko beam. The supported beam sections show a start frequency at $k = 0$, the so-called cut-off frequency, below which no travelling waves are generated and only static elastic displacement of the beam occurs. This is the reason that only 1 of the roots is shown in the figure, as the cut of frequencies of the other wave mode are far above the considered 10 Hz.

The required mesh size is based on Cook's approximation (93), which states that the maximum element size should be smaller than a tenth of the wave length. For the Timoshenko beam considered, the element size should be smaller than: $2\pi/0.054/10 = 11.64$ m. This condition is easily met as the applied element length is chosen as 0.5 m to match the shear beam length of the soil column.

4.3.3. Boundary Conditions

The boundary conditions for the ground response part of the model were previously presented in section 4.2.4.

No specific boundary conditions apply to the structural model of the monopile. The constraints applied for the foundation is modelled with macro-element formulations as covered in section 4.4. The top of the pile is free.

Table 4.1: Soil reduction factors D_e according (54)

Safety factor F_L	depth [m]	Reduction factor D_e	
		R ≤ 0.3	R > 0.3
$0 \leq F_L < 1/3$	$0 \leq d < 10$	0	1/6
	$10 < d \leq 20$	1/3	1/3
$1/3 \leq F_L < 2/3$	$0 \leq d < 10$	1/3	2/3
	$10 < d \leq 20$	2/3	2/3
$2/3 \leq F_L < 1$	$0 \leq d < 10$	2/3	1
	$10 < d \leq 20$	1	1

4.4. Seismic Soil-Structure Interaction

Combining of the ground response and the Winkler-beam models requires the formulation of the Winkler springs. Expressions for frequency dependent foundation impedances have been developed by (85) and (5). These are covered in more detail in chapter 5. These models are derived for the frequency domain and are therefore not easily implemented in a time domain analysis. Frequency independent derivations of the spring models have been developed based on the separation of near field and far field stiffness. However, all the models are unable to determine the SSI during soil liquefaction. A crude method to implement this soil degradation is by using pore-pressure based reduction coefficients on the P-Y curves. However, these models still fail in medium dense sands when displacement hardening is observed (109).

There are three major approaches to account for soil liquefaction in a Winkler-foundation (109; 74):

1. Apply a limit pressure to account for flow liquefaction. This approach is mainly intended for the quasi-static analysis of lateral spreading soil and may not be suitable for harmonic motions.

2. The use of P-Y curves for undrained soft clay for liquefied soil layers.

3. Using standard P-Y curves which are corrected for soil degradation by a p-multiplier based on the state of the soil. Often, these reduction factors are based on the pore-pressure build-up in the soil. Predefined reduction factors based on soil characteristics are provided by several Guidelines (see section 4.4.1). Another method is the use of macro-elements, which are basically more elaborate P-Y formulations which account for nonlinear soil effects in a direct manner.

The approaches mentioned in item 3 are presented in the subsections below.

4.4.1. P-Y Reduction Factors

A quick and simple method to account for the loss of strength in the soil is to directly relate this to a reduction in foundation stiffness. This can be achieved by a so-called p-multiplier which changes the displacement resistance of the Winkler-foundation parameters. P-Y reduction factors for liquefiable soils are provided by several codes and studies (54; 69; 119).

The (54) uses a safety factor, F_L, based on fineness content and excitation amplitude, to determine a reduction coefficient, D_e, which is to be used in e.g. earthquake analyses. This safety factor is defined as the ratio between a liquefaction susceptibility term, R, and a excitation term, L. The reduction coefficients as proposed by (54) are presented in table 4.1. Note that these factors are predefined based on liquefaction susceptibility of the soil column and do not take any pore-pressure build-up during the excitation into account. This method can therefore be used for ultimate limit state (ULS) and accidental limit state (ALS) predictions, where the soil is assumed to be liquefied. This method is less useful for fatigue limit state (FLS) analyses as it does not consider any transition phase.

() developed p-multipliers based on real-time pore-pressure build-up. They were able to reasonably predict the stress ranges in the pile using a linear relation between the pore-pressure ratio and the soil stiffness. The changing foundation parameters allow for the evaluation of the stresses during the process of liquefaction. they found the reduction factor for liquefaction to be around 0.9.

4.4.2.   Macro-Elements for Seismic Analysis

The P-Y reduction factors simply scale the existing backbone curve. However, it has been shown that this method is only valid for certain soil characteristics. Studies by (107; 13) find that back calculated P-Y curves show a increase in stiffness for large deflections. This behaviour is similar to the strain hardening phenomenon of undrained dense soils. A relation between the foundation resistance and the relative density of the soil can therefore be made (118). Various macro-elements have been developed to include the dependency of factors besides the pore-pressure ratio.

Macro-elements are basically element formulations that capture the global behaviour of a system. They are derived by integrating the material behaviour over the locally affected volume and represent the global stress-strain response at the soil-structure interface based on the externally applied loading (109). A major advantage of the macro-element is that nonlinear phenomena are reduced to global response, allowing for the efficient implementation of these phenomena into a larger model.

Three aspects of SSI can be identified for seismic analysis:

1. Nonlinear constitutive soil behaviour (Liquefaction i.a.)

2. Geometric nonlinearity

3. Frequency/rate dependency.

Various attempts to develop macro-element formulations for these aspects have been done. It is important to note that these aspects are not independent of each other.

Nonlinear Constitutive Soil Behaviour

Attempts to extend the refular P-Y method for liquefied soils has been done by adapting the P-Y curves (97). However, this pseudo-static approach fails to capture the dynamics and the degradation of soil properties during earthquakes (115). Dynamic (monotonic) P-Y formulations have been proposed by (13; 72; 74). These are nonlinear spring-dashpot systems based on free field effective stress and soil stiffness degradation to account for soil liquefaction.

Investigations into the SSI and the effect of liquefaction on pile foundations have been performed by (13; 28; 106; 15). These studies either tuned element formulations to results obtained with model tests or used back-calculation methods to determine the experienced force-displacement.

Geometric Nonlinearity

Geometric nonlinearity is related to the soil-structure interface. Forced pile motions can lead to gap formation between the pile wall and the soil.

Macro-element formulations for pile foundations have been developed by (30; 13; 83). These formulations are primarily based on the lack of tension on the lee side of the pile and are based on mass, spring and damper systems with gap functionality.

The true occurrence of gap formation at the soil-pile interface is hard to predict as the formation and size also depends on the rate at which the negative and positive pressure in the formed gap can dissipate. The most accurate method to date is a hydrodynamic analysis which takes both the soil permeability as the soil-structure interface into consideration (41).

Frequency/Rate Dependency

The nonlinearities described in the subsections above are frequency dependent. This means that frequency independent foundation parameters are unable to describe the complete dynamics during a seismic analysis as earthquakes contain a spectrum of frequencies. However, it is argued by some that the contribution of non-interesting frequencies is negligible in seismic analysis (66).

The frequency dependency of the foundation parameters can be contributed to various phenomena occurring in the soil. One of these is related to the hydraulic conductivity of the soil, as discussed in section 2.3. It was found that a low hydraulic conductivity can result in significant resistance (22).

Another cause for the change in response for varying frequencies is the inertia associated with the soil surrounding the foundation. The stiffness and associated mass of the soil result in a frequency dependent response, similar to that of a mass spring system. Moreover, the soil column can be excited in its natural frequencies, resulting in resonance effects. The frequency dependent SSI is covered in more detail in chapter 5.

4.5.   Summary

In this chapter, two numerical models were presented. The first model is a nonlinear ground response model. This model has been developed in three different ways: spring elements (MATLAB and ANSYS) and solid elements (ANSYS). The semi-empirical formulations on which the soil degradation during an earthquake is based were presented. The second model covered in this chapter was the so-called seismic Winkler-beam model. This model is a BNWF directly coupled with the nonlinear ground response model previously defined. The coupling of the model is realised by macro elements. Possible formulations for these elements, which could incorporate soil degradation and other nonlinear effects into the model, was presented in the last section.

Chapter 5

Soil-Structure Interaction

5.1.   Introduction

As discussed in chapter 4, one of the major uncertainties in the seismic analysis of monopile foundations is in the SSI. This chapter investigates the soil response to harmonic pile displacements to boost the understanding of the mechanisms involved in the soil during dynamic loading. The obtained response of the foundation to the harmonic excitation is used to determine the frequency dependent foundation properties. This will eventually be used in a hybrid frequency-time domain model in chapter 6.

The soil response will be determined for a cross section of the embedded monopile with a plane strain and plane stress approach. The difference between the plane stress and plane strain assumptions, and the derivation for the linear small-strain case, are presented in section 5.2. This is followed by the presentation of the FE plane strain model in section 5.3. Finally, the sections 5.4 and 5.5 cover the results obtained for the linear and nonlinear material models respectively.

5.2.   Analytical Plane Stress/Strain Formulation

The Winkler-beam model, as presented in chapter 4, is often used for the analysis of piles under lateral loads. The accuracy in predicting the response of a pile to dynamic loading is strongly dependent on the description of the soil in which the pile is embedded. The Winkler foundations is usually discretised as uncoupled springs, representing the resistance of the soil at various depths. Under the assumption that these springs act indeed uncoupled, an SSI analysis can be performed using a 2D plane strain approach which represents such a soil layer. Figure 5.1 shows an illustration of the 2D discretisation of an 3D soil volume.

Various researchers have investigated the resistance of soils to the lateral harmonic loading of piles. One of the first was (8), who derived a function based on the assumption that there is no interaction between the layers in the vertical direction. This method can therefore be categorised as a plane strain model. Although this model forms the basis for many methods, it has been shown that this approach is only valid for the high frequency range above the cut-off frequencies of the soil (5). Moreover, (110; 111) show that the plain strain condition accurately describes the stress field for long slender piles, but that this assumption no longer holds for large diameter tubulars like the monopile considered in this thesis.

An alternative solution is based on the plane stress approach, where the soil is considered in 3 dimensions. Here, the normal stresses in the vertical direction are ignored but the variation in shear force in the vertical direction is included to come to a closed-form solution. This method is worked out by i.a. (5; 85). The plane-stress approach has been shown to be superior for large diameter cylinders as these provoke, in contrast to flexible slender piles, a more global soil response (110; 111).

The small-strain assumption assures that the problem is linear. Therefore, analytical solutions can be
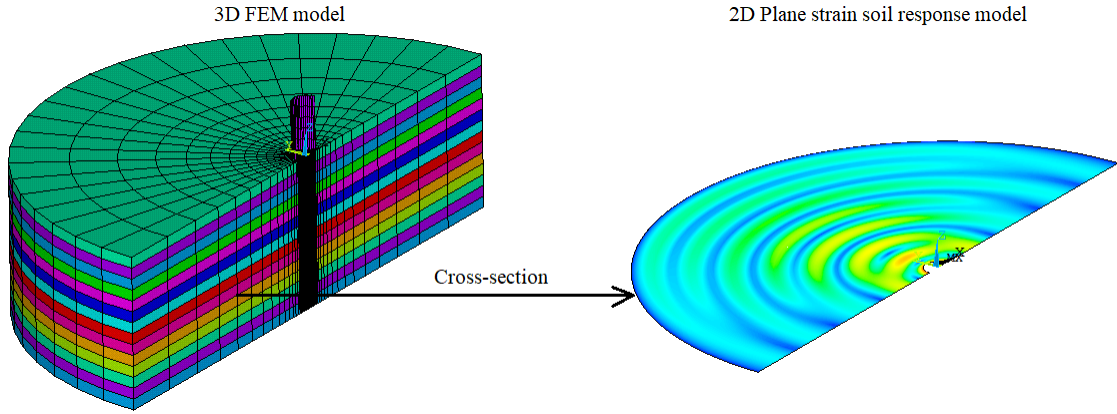
Figure 5.1: Plane strain simplification of the considered situation. The left shows the full 3D FE model and the right is a 2D cross-section of this model. The 2D plane strain model shows waves radiating from a harmonically displaced pile.

derived for the small-strain response of a pile to harmonic lateral loading. The analytical derivation for the plane stress and plane strain models are presented below.

5.2.1.   Plane Strain: Baranov-Novak Layer

The plane strain methods assumes the soil to be a stacked column of independent thin soil layers. Such a layer is often referred to as a Baranov-Novak layer, after (8; 86). The resistance of the soil is determined from the steady-state response of the layer to a harmonic motions.

The impedance of the soil is determined from a stress equilibrium in a linear elastic disc with plane strain constraints. The derivation and the expression of the Baranov-Novak layer is in many aspect similar to that of the plane stress method, and can be found by eliminating all the vertical dependent terms from the expressions. Due to this similarity is only the derivation of the more elaborate 3 directional plane stress method presented in this report.

5.2.2.   Plane Stress: Shear Interacting Layer

The plane stress method assumes a pile embedded in a soil layer fixed to a rigid base. The plane stress refers to the capability of the soil layers to transfer shear forces in the vertical direction. This allows for closed form solutions to be obtained.

Equation of Motions

The EOM for the plane stress soil response are based on the equilibrium equations for stresses on a soil element in the cylindrical coordinate system:

$$\frac{\partial \sigma_r}{\partial r} + \frac{1}{r}\frac{\partial \tau_{r\theta}}{\partial \theta} + \frac{\sigma_r - \sigma_\theta}{r} + \frac{\partial \tau_{rz}}{\partial z} = \rho_s \frac{\partial^2 u_r}{\partial t^2} \tag{5.1a}$$

$$\frac{1}{r}\frac{\partial \sigma_\theta}{\partial \theta} + \frac{\partial \tau_{r\theta}}{\partial r} + \frac{2\tau_{r\theta}}{r} + \frac{\partial \tau_{\theta z}}{\partial z} = \rho_s \frac{\partial^2 u_\theta}{\partial t^2} \tag{5.1b}$$

The equations above can be written in terms of displacement by assuming harmonic soil motions: $u_r = u_r(r,\theta,z,\omega)e^{i\omega t}$ and $u_\theta = u_\theta(r,\theta,z,\omega)e^{i\omega t}$. Substituting the stress-strain relations for cylindrical coordinates, equations 5.1 can be expressed as:

$$(\lambda + 2\mu)\frac{\partial}{\partial r}\left[\frac{1}{r}\left(\frac{\partial r u_r}{\partial r} + \frac{\partial u_\theta}{\partial \theta}\right)\right] - \mu\frac{1}{r}\frac{\partial}{\partial \theta}\left[\frac{1}{r}\left(\frac{\partial r u_\theta}{\partial r} - \frac{\partial u_r}{\partial \theta}\right)\right] + \mu\frac{\partial^2 u_r}{\partial z^2} + \rho\omega^2 u_r = 0 \tag{5.2a}$$

$$(\lambda + 2\mu)\frac{1}{r}\frac{\partial}{\partial \theta}\left[\frac{1}{r}\left(\frac{\partial r u_r}{\partial r} + \frac{\partial u_\theta}{\partial \theta}\right)\right] + \mu\frac{\partial}{\partial r}\left[\frac{1}{r}\left(\frac{\partial r u_\theta}{\partial r} - \frac{\partial u_r}{\partial \theta}\right)\right] + \mu\frac{\partial^2 u_\theta}{\partial z^2} + \rho\omega^2 u_\theta = 0 \tag{5.2b}$$

Where the Lamé parameters are complex valued according to $1+2\beta i$, with β being the critical damping ratio of the soil.

The displacements can be expressed in terms of the two potential functions representing the longitudinal and shear waves:

$$u_r = \frac{\partial \Phi}{\partial r} + \frac{1}{r} \frac{\partial \Psi}{\partial \theta} \tag{5.3a}$$

$$u_\theta = \frac{1}{r} \frac{\partial \Phi}{\partial \theta} - \frac{\partial \Psi}{\partial r} \tag{5.3b}$$

Substituting equations 5.3 in equations 5.2 results in two uncoupled differential equations:

$$(\lambda + 2\mu) \nabla^2 \Phi + \mu \frac{\partial^2 \Phi}{\partial z^2} + \rho \omega^2 \Phi = 0 \tag{5.4a}$$

$$\mu \nabla^2 \Psi + \mu \frac{\partial^2 \Psi}{\partial z^2} + \rho \omega^2 \Psi = 0 \tag{5.4b}$$

Where:

$$\nabla^2 = \frac{\partial^2}{\partial r^2} + \frac{1}{r} \frac{\partial}{\partial r} + \frac{1}{r^2} \frac{\partial^2}{\partial \theta^2} \qquad \text{the Laplacian operator for cylindrical coordinates} \tag{5.5}$$

The potential functions can be written as the products of 3 functions, describing the dynamics in the radial, tangential and vertical directions:

$$\Phi(r, \theta, z) = R_1(r)\, \Theta_1(\theta)\, Z_1(z) \tag{5.6a}$$

$$\Psi(r, \theta, z) = R_2(r)\, \Theta_2(\theta)\, Z_2(z) \tag{5.6b}$$

Substituting these expressions in equations 5.4 gives:

$$(\lambda + 2\mu) \frac{1}{R_1} \left[\frac{\partial^2 R_1}{\partial r^2} + \frac{1}{r} \frac{\partial R_1}{\partial r} \right] + (\lambda + 2\mu) \frac{1}{r^2} \frac{1}{\Theta_1} \frac{\partial^2 \Theta_1}{\partial \theta^2} + \mu \frac{1}{Z_1} \frac{\partial^2 Z_1}{\partial z^2} + \rho \omega^2 = 0 \tag{5.7a}$$

$$\mu \frac{1}{R_2} \left[\frac{\partial^2 R_2}{\partial r^2} + \frac{1}{r} \frac{\partial R_2}{\partial r} \right] + \mu \frac{1}{r^2} \frac{1}{\Theta_2} \frac{\partial^2 \Theta_2}{\partial \theta^2} + \mu \frac{1}{Z_2} \frac{\partial^2 Z_2}{\partial z^2} + \rho \omega^2 = 0 \tag{5.7b}$$

These expressions can be decomposed in three different partial differential equations describing the dynamics in one of the three directions:

$$\frac{\partial^2 R}{\partial r^2} + \frac{1}{r} \frac{\partial R}{\partial r} - \left(q^2 + \frac{n^2}{r^2} \right) R = 0 \tag{5.8a}$$

$$\frac{\partial^2 \Theta}{\partial \theta^2} + n^2 \Theta = 0 \tag{5.8b}$$

$$\frac{\partial^2 Z}{\partial z^2} + a^2 Z = 0 \tag{5.8c}$$

Where:

$$q = \frac{1}{\eta} \sqrt{a^2 - \frac{\omega^2}{V_s^2}} \qquad \text{for} \quad \Phi \tag{5.9a}$$

$$q = \sqrt{a^2 - \frac{\omega^2}{V_s^2}} \qquad \text{for} \quad \Psi, \quad \text{from now on referred to as } s \tag{5.9b}$$

The equations 5.8 are ordinary differential equations and can be solved. The potential functions can then be expressed in terms of these solutions as follows:

$$\Phi = \left[A_1 I_n(qr) + B_1 K_n(qr) \right] \left[A_2 \sin(n\theta) + B_2 \cos(n\theta) \right] \left[A_3 \sin(az) + B_3 \cos(az) \right] \tag{5.10a}$$

$$\Psi = \left[A_4 I_n(sr) + B_4 K_n(sr) \right] \left[A_5 \sin(n\theta) + B_5 \cos(n\theta) \right] \left[A_6 \sin(az) + B_6 \cos(az) \right] \tag{5.10b}$$

where:

A_i, B_i	=	Integration constants	(-)
I_n	=	N-th order Bessel function of the first kind	(-)
K_n	=	N-th order Bessel function of the second kind	(-)

The integration constants are to be determined from the boundary conditions. At the boundary away from the pile ($r \rightarrow \infty$), the soil motions should vanish. Therefore, the integration constants A_1 and A_4 are 0. For the case where the pile motions are in the direction of $\theta = 0$, the constants A_2 and B_5 are 0 to satisfy the zero radial displacement condition at $\theta = 0$ and $\theta = \pi/2$. The order of the functions can be determined from the requirement that the tangential motion u_θ is positive for $0 \le \theta \le \pi$ and negative for $\pi \le \theta \le 2\pi$. Finally, the boundary conditions stating that the bedrock is fixed and that the sea bed is stress free results in the contstants A_3 and A_6 are 0 and requires $\cos(aH) = 0$.

Based on the above, the potential functions become:

$$\Phi_m = A \cos(\theta) \, K_1(q_m r) \, \cos(a_m z) \tag{5.11a}$$

$$\Psi_m = B \sin(\theta) \, K_1(s_m r) \, \cos(a_m z) \tag{5.11b}$$

The displacements and the stresses in the soil can then be determined by substituting the potential functions into equations 5.3 to get:

$$u_r = \cos(\theta) \sum_{m=1}^{\infty} \left(-A_m \left[\frac{1}{r} K_1(q_m r) + q_m K_0(q_m r) \right] + B_m \frac{1}{r} K_1(s_m r) \right) \tag{5.12a}$$

$$u_\theta = \sin(\theta) \sum_{m=1}^{\infty} \left(-A_m \frac{1}{r} K_1(q_m r) + B_m \left[\frac{1}{r} K_1(s_m r) + s_m K_0(s_m r) \right] \right) \tag{5.12b}$$

The lateral displacement of the pile in the soil can be described by the summation of the harmonic amplitudes:

$$U = \sum_{m=1}^{\infty} U_m \tag{5.13}$$

Combining equations 5.12 and 5.13 for the conditions $u(r = r_0, \theta = 0) = U$ and $u(r = r_0, \theta = \pi/2) = -U$ gives:

$$\sum_{m=1}^{\infty} \left(-A_m \left[\frac{1}{r_0} K_1(q_m r_0) + q_m K_0(q_m r_0) \right] + B_m \frac{1}{r_0} K_1(s_m r_0) \right) = \sum_{m=1}^{\infty} U_m \tag{5.14a}$$

$$\sum_{m=1}^{\infty} \left(-A_m \frac{1}{r_0} K_1(q_m r_0) + B_m \left[\frac{1}{r_0} K_1(s_m r_0) + s_m K_0(s_m r_0) \right] \right) = -\sum_{m=1}^{\infty} U_m \tag{5.14b}$$

Solving equations 5.14 for A_m and B_m finally gives:

$$A_m = -\frac{(2/r_0) K_1(s_m r_0) + s_m K_0(s_m r_0)}{(q_m/r_0) K_0(q_m r_0) K_1(s_m r_0) + (s_m/r_0) K_1(q_m r_0) K_0(s_m r_0) + q_m s_m K_0(q_m r_0) K_0(s_m r_0)} U_m \tag{5.15a}$$

$$B_m = -\frac{(2/r_0) K_1(q_m r_0) + q_m K_0(q_m r_0)}{(q_m/r_0) K_0(q_m r_0) K_1(s_m r_0) + (s_m/r_0) K_1(q_m r_0) K_0(s_m r_0) + q_m s_m K_0(q_m r_0) K_0(s_m r_0)} U_m \tag{5.15b}$$

Resistance of the Soil Layer

The lateral resistance of the soil from harmonic excitation at the soil-pile interface can be determined by integration of the stresses over the circumference of the pile. For an harmonic excitation of the form $U e^{i\omega t}$, the amplitude of the soil resistance p is:

$$p = -\int_0^{2\pi} r_0 \left[\sigma_r(r_0) \cos(\theta) - \tau_{r\theta}(r_0) \sin(\theta) \right] d\theta \tag{5.16}$$

The relevant stresses at $r = r_0$ can be found by the stress strain relations and the solutions to the potential functions:

$$\sigma_r = \cos(\theta) \frac{2G_s}{r_0} \sum_{m=1}^{\infty} U_m \left(-A_m \left[s_m K_0(s_m) + \frac{s_m^2 \eta_\sigma^2}{2} K_1(s_m) + 2K_1(s_m) \right] + \right.$$
$$\left. B_m \left[s_m \eta_s K_0(s_m \eta_s) + 2K_1(s_m \eta_s) \right] \right) \tag{5.17}$$

$$\tau_{r\theta} = \sin(\theta) \frac{2G_s}{r_0} \sum_{m=1}^{\infty} U_m \left(-A_m \left[s_m K_0(s_m) + 2K_1(s_m) \right] + \right.$$
$$\left. B_m \left[s_m \eta_s K_0(s_m \eta_s) + \frac{s_m^2 \eta_\sigma^2}{2} K_1(s_m \eta_s) + 2K_1(s_m \eta_s) \right] \right) \tag{5.18}$$

Substituting equations 5.17 and 5.18 into equation 5.16, leads to a frequency dependent expression for the soil resistance:

$$p(\omega, z) = \pi G_s \sum_{m=1}^{\infty} R_m U_m \cos(a_m z) \tag{5.19}$$

Where:

$$R_m = \frac{4K_1(q_m r_0) K_1(s_m r_0) + s_m r_0 K_1(q_m r_0) K_0(s_m r_0) + q_m r_0 K_0(q_m r_0) K_1(s_m r_0)}{q_m K_0(q_m r_0) K_1(s_m r_0) + s_m K_1(q_m r_0) K_0(s_m r_0) + q_m s_m r_0 K_0(q_m r_0) K_0(s_m r_0)} \tag{5.20}$$

As mentioned in the section on the Baranov-Novak layer, the expressions are similar. The Baranov-Novak expression is obtained by setting the variable a equal to zero, eliminating any shear interaction between the layers.

5.3.   Numerical Soil-Structure Interaction Model

The 2 dimensional plane strain model for determining the lateral response of the soil for harmonic loading is based on a cross section of the full 3D situation (figure 5.1). The finite element model of the cross-section has been developed in ANSYS. Small adaptions have been made to the geometry and mesh to optimise the model for the analysis of the frequency dependent foundation reaction.

The model is a 2 dimensional representation of a horizontal cross-section of the embedded monopile. The model is presented in figure 5.2. Only the outer soil medium is modelled to be able to identify the lateral response from the surrounding soil. The missing added mass from the inner volume of the pile has to be added separately in the case of a soil filled hollow cylinder. The pile is considered to be rigid as actual ovalisation or deformation is unknown in the 2D plane model. The model characteristics are discussed in the following subsections.

The model is build up of a rigid half cylinder surrounded by a soil medium. The model makes use of the symmetry axis in the y-plane for reduced computational time, basically making the model a half annular disk. The dimensions of the model are based on the ratio between the outer soil radius and the monopile radius. A radii ratio of 40 has been applied in the harmonic analyses. This ratio is based on the required number of elements. As discussed in the section below, a dense mesh is required leading to a unrealistic number number of elements for ratios larger than 40. Use is made of an viscous boundary to mimic a boundary infinitely far away. This boundary is discussed in further detail in the boundary conditions section below.

5.3.1.   Element Types

Similar to the 3D FE model, two types of elements are used. The element choice is based on the type of analysis: small-strain or nonlinear soil regime. Both linear as well as higher-order elements used in the different analysis. The two types are:

Figure 5.2: Impression of the 2D plane strain model developed in ANSYS. The inner purple semi-circle is the monopile wall and the cyan elements are the soil. Only half the cross-section is modelled as use is made of the symmetry plane of the situation.
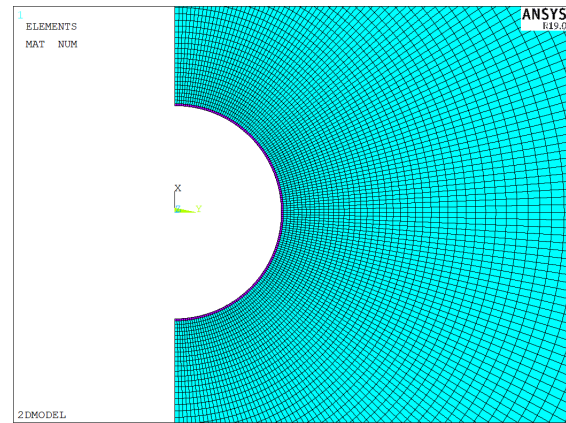
1. The linear small-strain analysis is performed with regular plane elements. ANSYS provides this element as first order PLANE182 element with linear displacement behaviour or as higher order PLANE183 element with quadratic displacement behaviour. The element nodes each have 2 translational DOF (x,y).

2. The non-linear analysis is performed with coupled pore-pressure mechanical solid elements. Again, ANSYS provides this element as first order CPT212 element with linear displacement behaviour or as higher order CPT213 element with quadratic displacement behaviour. The element nodes each have 2 translational DOF (x,y). The corner nodes have a additional pore-pressure DOF. The theory behind the coupled pore-pressure mechanical elements is covered in section 5.5.1.

The geometries of the regular plane and the coupled pore-pressure mechanical elements are identical. The geometry of the linear elements is made up of 4 corner nodes as presented in figure 3.3a. The higher-order elements make use of an additional 4 midside nodes. The geometries of the higher order element types is presented in figure 3.3d. The soil volume is primarily[1] meshed with the cubic shape option, as these provide the highest accuracy.

5.3.2.   Mesh and Mesh Size

The mesh layout of the model is produced with a mapped mesh type resulting in tangential symmetric elements. The mesh size is based on an approximation by (93). The maximum element length is taken to be around a tenth of the wave length. For e.g. a maximum frequency input of 10 Hz in a soil with a shear wave velocity of 100 m/s, the maximum element size in the soil should be 1.0 m or less in the direction of wave propagation. The soil element sizes grows linearly in the radial direction. Therefore, using this requirement up to 40 radii away from the pile requires approximately 460 square elements around the semi-circle.

5.3.3.   Boundary Conditions

The monopile is modelled as a rigid ring as the local dynamics of the monopile tubular is unknown in the 2D harmonic analysis of the foundation. The rigidity is achieved by coupling the degrees of freedom of the nodes on the inside of the pile with the master-slave method. This approach also eliminates the need to sum the load responses to harmonic displacements over the pile wall to find the global foundation response.

The model uses the symmetry axis in the y-direction for reduced computational effort. The symmetry is achieved by constraining the out of plane motions and rotations. No constraint has to be used for the pore pressure degree of freedom as the symmetry axis will act as an impermeable boundary.

Two far field boundary conditions are applied in the model, depending on the type of analysis. The

---

[1]Completely meshed with the cubic shape option in case of plastic material behaviour or linear elements.

first type is a non-reflective viscous boundary based on the method as described in section 3.3.3.1. The second method is fixing the DOF of the boundary. The latter was used in the attempts to capture the cut-off frequency and static response in the FE plane strain model.

5.4. Small-Strain Response

The strains in the soil due to lateral pile displacement stay in the small-strain regime for the majority of the load cases for a monopile foundation. For this reason, this section will cover the SSI for a pile harmonically excited in the lateral direction.

Several assumptions have been made in this section to determine the small-strain repsonse of the soil. These assumptions are:

1. The pile is a perfectly elastic circular cylinder (rigid in the cross-sectional plane).
2. The soil-pile interface is perfectly bonded.
3. The soil is a linear homogeneous isotropic material with hysteretic material damping.
4. The excitation type is harmonic.

5.4.1. Finite Element Method

Besides the analytical expressions as presented in section 5.2, the response of the soil to harmonic loading also determined with the 2 dimensional SSI FE model introduced in section 5.3. The model uses a plain strain approach with a non-reflective viscous boundary layer at the outer radius of the soil. This makes the situation identical to that of a Baranov-Novak layer.

As discussed in section 5.2, the Baranov-Novak method is not applicable for the low frequency range as it does not take the response below the cut-off frequency correctly into account. Moreover, the Baranov-Novak method has an asymptotically declining response for $\omega \to 0$, meaning that this method results in no static resistance. An attempt has been made to correctly model the static response and the cut-off frequency effect by fixing the boundary of the outer soil diameter. This resulted however in a couple of issues:

1. The cut-off frequency is determined by the fundamental eigenfrequency of the soil disc. Tuning the dimensions of the disc to achieve a realistic natural frequency resulted in a diameter that was significantly smaller than necessary for a correct static response. Tuning the disc to get the correct static response resulted in an incorrect cut-off frequency.

2. The fixed outer boundary makes the model a finite system with natural frequencies. Above the fundamental natural frequency (the cut-off frequency), these higher natural frequencies result in resonance which influence the results.

3. As can be understood from the plane stress approach, the static response of the soil is based on the transfer of the load via the shear stresses in the layers to the rigid bedrock. This is a different mechanism than that considered in the SSI FE model, which transfers the load to the outer edge of the soil circle.

No realistic results were obtained from the plane strain model with fixed boundaries due to these issues.

5.4.2. Harmonic Small-Strain Soil Response

The impedance of the soil for lateral harmonic excitation is determined with the analytical plane stress and plane strain approaches, as well as with the plain strain FE model. The frequency response functions are presented in figure 5.3. The real part of the plot shows the dynamic storage stiffness (in-phase stiffness and 180 degree out-of-phase inertia) of the soil response, and the imaginary part represents the damping. The figure clearly shows the difference between the plane strain and plane stress approach. Note that the plane stress plot only shows the results of a single soil response mode. Two important features are present in the plot:
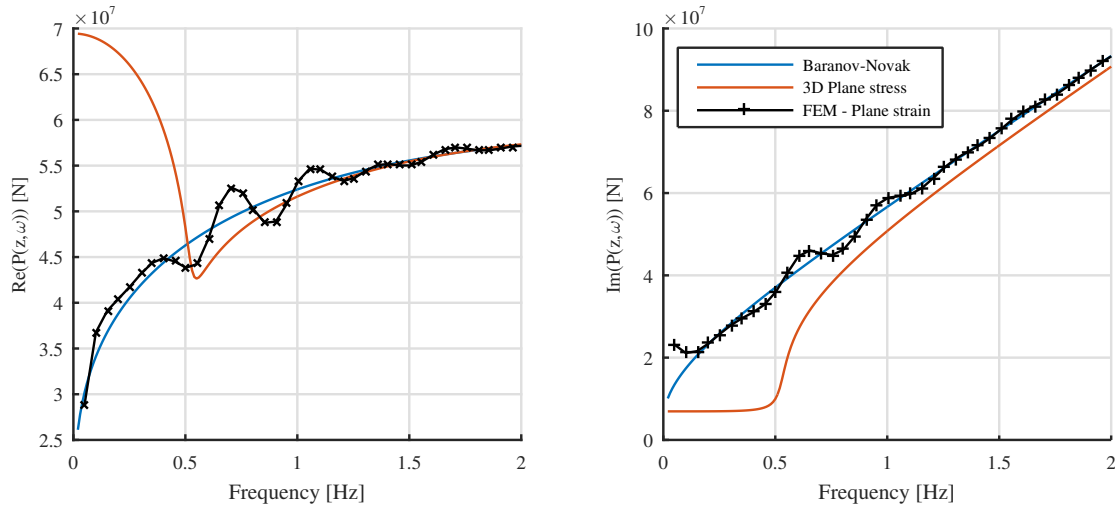
Figure 5.3: Foundation impedance for linear elastic material. The left pane shows the real component of the impedance. The right pane shows the imaginary part which represents the damping.

1. The plane strain and plane stress approach are identical for the frequency range well above the cut-off frequency of the system.

2. The plane strain method approaches 0 for $\omega \rightarrow 0$, in contrast to the plane stress approach which reaches a non-zero kinematic stiffness.

The plane stress method shows some characteristic behaviour for an elastic medium. Three response cases can be distinguished:

1. $\omega < \omega_{cut-off}$: The energy associated with the displacement of the pile is stored as elastic potential in the surrounding soil.

2. $\omega = \omega_{cut-off}$: The soil medium is excited in its resonance frequency. This leads to standing waves in the soil column (vertical direction). The real part of the impedance shows a dip as the displacement resistance falls. This point indicates the highest associated added mass in the system.

3. $\omega > \omega_{cut-off}$: The harmonic displacement of the pile leads to the generation of waves. These waves carry away energy, which is felt by the system as a damping force. Figure 5.3 shows clearly the significant increase in damping for the range above the cut-off frequency of the system.

Note that the presented plane stress results are only for a single soil response mode shape. Multiple modes shapes in the system can be contributed for by taking the linear superposition of the contributions of each mode.

The figures show a good fit between the analytical expression and the FE plane strain results. The FE model shows a perturbation in the frequency response compared to the analytical solution. This is due to natural frequencies related to dynamic modes occurring in the soil disc, which should not be present for a system with finite boundaries. This indicates that the applied non-reflective viscous boundary is imperfect. The numerical model shows to be sensitive to errors in this boundary, as small changes of about 1% in the viscous damper constant leads to more than a doubling of the perturbation as shown in figure 5.3.

Figure 5.4 shows the variation of the soil response parameters over the depth of the monopile foundation. Deeper layers show a generally stiffer response. Not only shows the figure an increase in the response parameters for increasing depth, it also shows the shift of the cut-off frequency to the right. The first is directly related to the increase of the soil stiffness (shear modulus) while the latter is a result of the increased shear wave velocity, which is in turn again related to the soil stiffness. The soil stiffness for the presented analytical methods is primarily dependent on the soil characteristics such as the shear modulus, material damping and Poisson's ratio. The only pile related parameter present
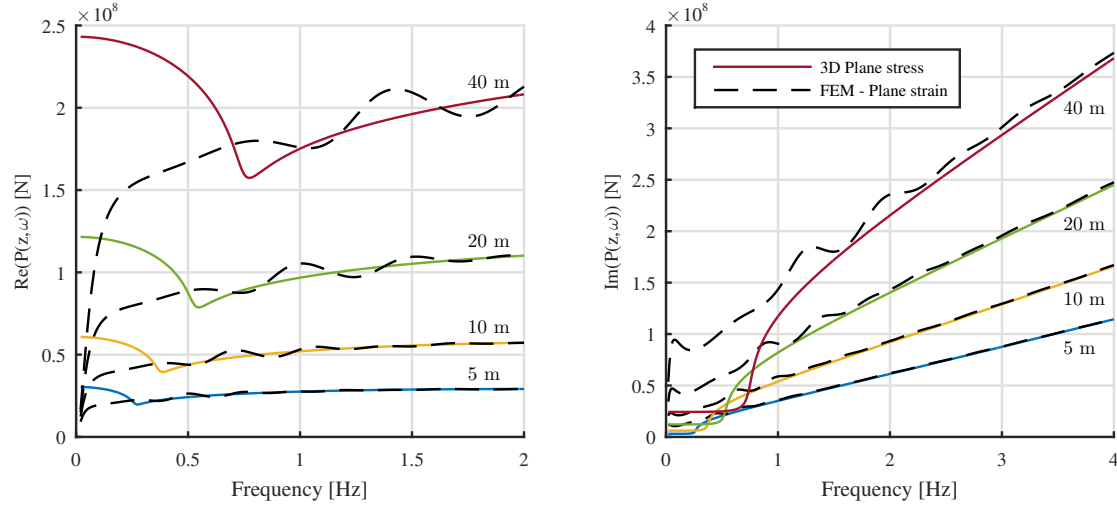
Figure 5.4: Depth dependency of the soil response. Left pane is the real component of the impedance. The right pane shows the imaginary part which represents the damping.

in the analytical expressions is the pile radius. However, the pile radius is considered constant over the depth in this thesis and does therefore not contribute to the change in soil repsonse.

5.4.3.   Added Mass, Added Damping and Stiffness

The time domain EOM used for structural dynamics are based on inertia terms (acceleration), viscous/drag terms (velocity) and stiffness terms (displacement). In order to be able to describe the obtained harmonic soil response, these terms have to be determined.

Method

The added mass, added damping and stiffness parameters of the soil layer are determined for the plane stress approach. This is based on the plane strain approach only being valid for the frequency range above the cut-off frequency and the higher accuracy of the plane stress method for large diameter tubulars (110; 111). Note that for the latter to be true, the Fourier composition of the pile motions should be known.

- The stiffness K, or the in-phase real part of the soil response, is determined from the static resistance of the pile. The stiffenss is considered to be independent of frequency as this simplifies the implementation of springs in the Winkler-type foundation.

$$K(z,\omega) = \mathbb{Re}(P(z,\omega = 0)) \tag{5.21}$$

- The (added) damping in the system is the 90 degree out-of-phase component of the soil response. The viscous damping constant B can then found by the following expression due to the harmonic nature of the response:

$$B(z,\omega) = \frac{\mathbb{Im}(P(z,\omega))}{i\omega u} \tag{5.22}$$

Where u is the displacement amplitude.

- The added mass is the 180 degree out-of-phase component of the soil response has to be determined from the real part. However, since the added mass and stiffness are both real vlues, these have to be separated from one another. Since the stiffness has already been defined as the static response (equation 5.21), the added mass parameter then takes the form of:

$$A(z,\omega) = \frac{\mathbb{Re}\left(P(z,\omega) - P(z,\omega = 0)\right)}{-\omega^2 u} \tag{5.23}$$
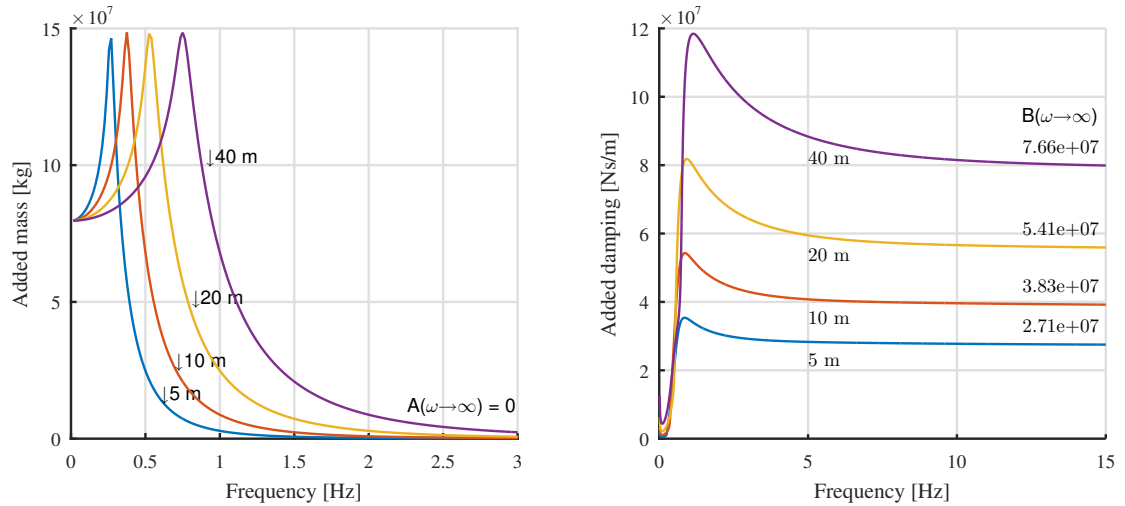
Figure 5.5: Foundation constants derived from the lateral soil response. Left pane shows the added mass and the right pane shows the added damping values as a function of frequency.

Result

Figure 5.5 shows the frequency dependent added mass and added damping values for various depths. The values have been determined with the above presented equations 5.22 and 5.23. Both the added mass and added damping have again three distinct point that characterise the soil behaviour: below cut-off frequency, cut-off frequency and above cut-off frequency. The plotted values are again for only a single soil response mode shape.

The added mass characteristics for the regions is defined as:

1. $\omega < \omega_{cut-off}$: All the depths show the same constant value for $\omega \to 0$. However, note that this is not for the true static situation as the quadratic frequency term in equation 5.23 leads to a non-defined value. The horizontal part at $\omega \to 0$ is because the inertia force resulting from the soil's mass associated with its displacement field is proportional to the quadratic frequency term.

2. $\omega = \omega_{cut-off}$: The added masses show to have different cut-off frequencies, however, the peak values are similar. This is because the inertia term is related to the associated displacement field, which is quadraticcaly dependent on the shear wave velocity. The added mass term is obtained by dividing it by the cut-of-frequency, which is also quadraticcaly dependent on the shear wave velocity.

3. $\omega > \omega_{cut-off}$: The added mass shows a asymptotic decay to zero for $\omega \to \infty$. An increase in frequency decreases the associated displacement area.

The added damping characteristics for the regions is defined as:

1. $\omega < \omega_{cut-off}$: The added damping is small for $\omega \to 0$. However, figure 5.5 shows a (small) quadratic decay for this region as the applied method captures the frequency independent hysteretic soil damping in its viscous equivalent.

2. $\omega = \omega_{cut-off}$: The added damping shows a strong increase at the cut-off frequency and has a peak closely to the right.

3. $\omega > \omega_{cut-off}$: The added damping shows a asymptotic decay to a constant value for $\omega \to \infty$.

5.4.4.   Discussion

The results obtained for the small-strain linear case are based on several simplifications and assumptions that do not represent reality. Major points that need to be considered when using the results are:

- The plane stress model assumes a homogeneous soil column with constant stiffness over the depth. The response function over the depth is identical, only being scaled by the vertical amplitude function due to the equation 5.6.

- The lateral resistance of the soil is due to the transfer of the load to the bedrock instead of to the far-field edge of the 2D plane strain model. This results in incorrect soil response for the plane strain model for the frequency range below the cut-off frequency.

- The cut-off frequencies are the natural frequencies of the soil response modes. These are dependent on the characteristics of the soil column, which are incorrectly assumed (as discussed in the first bullet).

- The 3D plane stress method results in mode dependent soil resistance. The resistance experienced by the pile is therefore a superposition of the response associated with the present pile modes. Again, these pile modes depend on the characteristics of the soil column.

5.5.   Nonlinear Soil Response

The strains in the soil around a monopile stay withing the small-strain regime for the majority of the load cases. However, earthquakes considered in the seismic ULS analysis are often ELE or even ALE events. These types of loading would excite the soil far beyond its linear regime. For this reason, attempts to model the nonlinear soil behaviour and SSI were done with the 2 dimensional FE plane strain model of the SSI. The nonlinear material model and the analysis is presented in the following section. Attempts to incorporate pore-pressure based liquefaction effects into the material model produced no results. The attempts are presented in appendix C.

5.5.1.   Soil Material Model

The applied soil model is based on a two-phase material model with stress dependent Mohr-Coulomb plasticity. The specifications are presented below.

Mohr-Coulomb Plasticity Model

The soil type used in this thesis is based on a medium fine liquefiable sand. The accuracy and value of the results is directly dependent on how realistic the material model captures true sand behaviour. For this reason, several material models have been considered, implemented and tested. The considered geomechanical material models provided by ANSYS where:

1. Mohr-Coulomb model for granular materials
2. Drucker-Prager material model for concrete

Neither of the material models provided the full desired plastic behaviour. The shear and volumetric stresses and strains could not be coupled in a controlled stable manner. This coupling is required for the contractive behaviour necessary for modelling possible liquefaction. The Mohr-Coulomb model was chosen as this was easiest implementable model with the best stability results in single element tests.

The stress strain behaviour of the soil skeleton is described by a linear isotropic stress-strain equation. The linear behaviour of the soil is capped by the pressure dependent Mohr-Coulomb yield criterion. The Mohr-Coulomb model is bases the deviatoric stress resistance on the friction resistance of the soil particles, as described by equation 2.10. The generalised Mohr-Coulomb yield surface and flow potential are defined by equations 5.24 and 5.25 respectively:

$$f_s = \frac{I_1}{3}\sin(\phi) + \sqrt{J_2}\left[\cos(\theta) - \frac{1}{\sqrt{3}}\sin(\theta)\sin(\phi)\right] \tag{5.24}$$

$$Q_s = \frac{I_1}{3}\sin(\psi) + \sqrt{J_2}\left[\cos(\theta) - \frac{1}{\sqrt{3}}\sin(\theta)\sin(\psi)\right] \tag{5.25}$$

where:

I_1, J_2, J_3	=	Stress invariants	(Pa)
θ	=	Lode angle	(deg)
ϕ	=	Internal friction angle	(deg)
ψ	=	Dilation angle	(deg)

The material parameters used in the model are presented in table 3.3. A dilatancy angle that is different from the friction angle results in a non-associated flow potential.

Various hardening rules have been implemented and tested. However, in combination with the two-phase elements, many of these led to convergence problems. For this reason, no hardening rule has been implemented in the final model. Eventually, the convergence issues could be assigned to numerical instability in the coupled pore-pressure mechanical elements, as discussed in appendix B. The hardening rules have not been investigated again after solving the instability issue.

Two-Phase Porous Media Mechanics

Saturated soil can be considered as a two phase system; the solid skeleton consisting of particles and the fluid in the pores. The analysis of such a two phase system includes both the structural analysis of the stress-strain behaviour of the soil skeleton as well as the flow of the fluid in the pores. The two are linked by (1) the change in volume as fluid is pressed out of the volumetric deformed element, (2) the effective stress due to the change in pore pressure. The dissipation of pore fluid is not relevant to describe full undrained soil behaviour as the dissipation rate is negligible small compared to the rate of loading. However, two phase analysis might hold more accurate results for moderately permeable soil types where pore pressure dissipation might influence the soil's behaviour.

A soil analysis can be performed in ANSYS with the use of the so called coupled pore-pressure mechanical elements. These elements are capable of determining both the structural stresses and strains, as well as the pore pressure and fluid flow. The element relations are based on the extended Biot consolidation theory, which considers the medium as a multi-phase material (6). The mechanical strain behaviour is described by the effective stress principle, while the fluid flow is based on a continuity equation for the mass of the fluid in a unit volume of the medium.

The strains occurring in the elements are the result of the stress-strain relation of the applied material model, using the effective stress components (equation 2.13). The deformation of the soil skeleton is determined using Hooke's law:

$$\sigma' = \mathbf{D} : (\epsilon - \epsilon_{pl}) \tag{5.26}$$

where:

σ'	=	Effective stress	(Pa)
$\mathbf{D}$	=	Elastic tangent stiffness matrix	(Pa)
ϵ	=	Strain tensor	(-)

The continuity equation as used in the coupled pore pressure mechanical elements is Darcy's law. In ANSYS, this equation is implemented as:

$$q = \frac{\kappa}{\gamma_f} \left(-\nabla p + \rho_f g \right) \tag{5.27}$$

where:

κ	=	Permeability of the soil	(m/s)
γ_f	=	Specific fluid weight	(kg/m^3)
g	=	Gravity acceleration vector	(m/s^2)

The structural behaviour and the fluid flow are connected with each other through the mass balance equation:

$$\nabla \left[\frac{\kappa}{\gamma_f} \left(-\nabla p + \rho_f g \right) \right] + \alpha \mathbf{I} \dot{\epsilon} + \frac{1}{k_m} \dot{p} = 0, \quad \text{where,} \quad \frac{1}{k_m} = \frac{\alpha - n}{K_s} + \frac{n}{K_f} \tag{5.28}$$
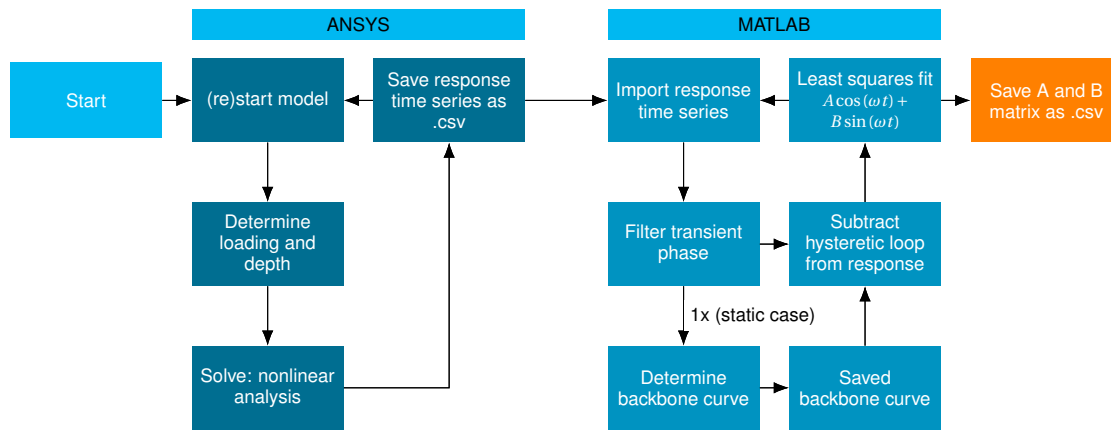
Figure 5.6: Flowchart of the nonlinear analysis procedure. The process exists of two parts: first the nonlinear analysis in the FE ANSYS, and second the post-processing in MATLAB.

where:

α	=	Biot coefficient	(-)
k_m, K_s, K_f	=	Biot, soil and fluid bulk modulii	(Pa)

The coupled pore-pressure mechanical elements showed numerical instability in the nonlinear analyses. The source of the instability was related to a by ANSYS redefined Biot coefficient, based on the bulk modulii of the soil and fluid. The issue is discussed in more detail in appendix B.

5.5.2. Harmonic Nonlinear Soil Response

This section presents the response of the nonlinear two-phase soil model for excitation in the lateral direction. First, the procedure that is used to extract the nonlinear soil response is presented. This is followed by the static and harmonic response.

The results presented in this section are determined with the 2D plane strain FE model, using the fixed outer boundary condition.

Analysis Procedure

The nonlinear soil response can not be obtained with a linear harmonic analysis, as performed in the previous section. The response is therefore determined with a implicit numerical solver in the time domain. Time series are generated in ANSYS and afterwards post-processed in MATLAB. The process to determine the nonlinear added mass and added damping parameters is presented as flowchart in figure 5.6.

The procedure for the analysis of the frequency impact of the soil response is as follows:

1. Force displacement time series are generated with the 2D plain strain FE model. These time series describe the force to displacement ratio and phase shift for various frequencies and amplitudes at various depths.

2. The time series are processed to obtain the steady state solution to the harmonic displacement input.

3. The static P-Y curve for the current soil and foundation characteristics is determined from a static load situation.

4. All the force displacement time series are corrected by subtracting the hysteretic loop generated with the static backbone curve from the response time series. This is done to be able to separate the spring and added mass terms. These are otherwise inseparable due to their 180 degrees phase difference. The term that is left after the subtraction is from here on referred to as added mass, even though this term can still contain stiffness response since the foundation stiffness can be dependent on other mechanisms, e.g. strain rate.

Figure 5.7: Force-displacement curves (P-Y) for the considered monopile with nonlinear soil behaviour.
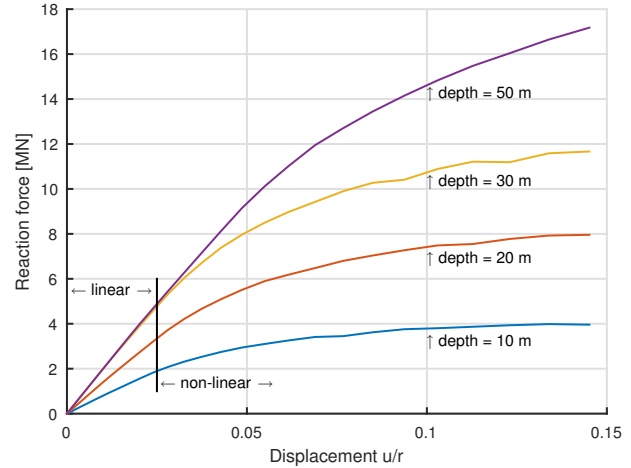
5. The resulting force displacement series are decomposed into a linear damping and added mass component.

Harmonic Soil Response

The static P-Y response of the foundation, which is used for the correction of the harmonic response, is presented in figure 5.7. It is seen in the figure that the stiffness of the foundation increases with depth[2]. The curves show to be linear for displacements smaller than ~0.02 u/r. For the considered monopile with a diameter of 7.4 m, this is ~8 cm. The results presented in

Figure 5.8 shows a selected number of force displacement curves. The presented data is for a foundations cross-section at 20 m depth with a shear wave velocity of 50 m/s, internal friction angle of 30° and a permeability of 1e-5 m/s. The remaining soil parameters are presented in table 3.3. The red line is the static P-Y curve as presented in figure 5.7, the blue line is the force-displacement curve determined with the FE model and the yellow line is the remaining force after the subtraction of the static hysteretic loop.

A couple of conclusions can be drawn from the force displacement plots. The static P-Y curve is capable of capturing the foundations response of low frequency motions. The static and the low frequency dynamic forces are nearly equal. Increasing the frequency results in an increasing influence from other mechanisms. The amplitude of the harmonic motion shows to have impact on the maximum force, but not on the shape of the force displacement curve.

The magnitude and phase of the remaining forces from the obtained force displacement curves (yellow in figure 5.8) are plotted on logarithmic scale in figure 5.9 and 5.10 respectively. It was found that the magnitude of the force is almost linearly dependent on the magnitude of the pile displacement, and quadratically dependent on the frequency of this excitation. This could indicate the dependency of the response to the acceleration term, as the expression for the acceleration is given as:

$$\ddot{x} = \omega^2 \left(u/D \right) \sin \left(\omega t \right) \tag{5.29}$$

The results are obtained for the fixed far-field boundary conditions. The results show for this case similar behaviour in wave radiation as for the linear analysis. The phase of the remaining force shows a sharp peak at about 0.2 Hz, after which it gradually increases from 0 to 120 degrees. This indicates a transition from static elastic response below 0.2 Hz to wave radiation above this value.

5.5.3.   Added Mass, Added Damping and Stiffness

The added mass, and added damping parameters are determined in the same manner as for the linear analysis, as presented in section 5.4.3. Only the stiffness of the nonlinear response is determined with

---

[2]Note that the depths differs form the linear analysis.
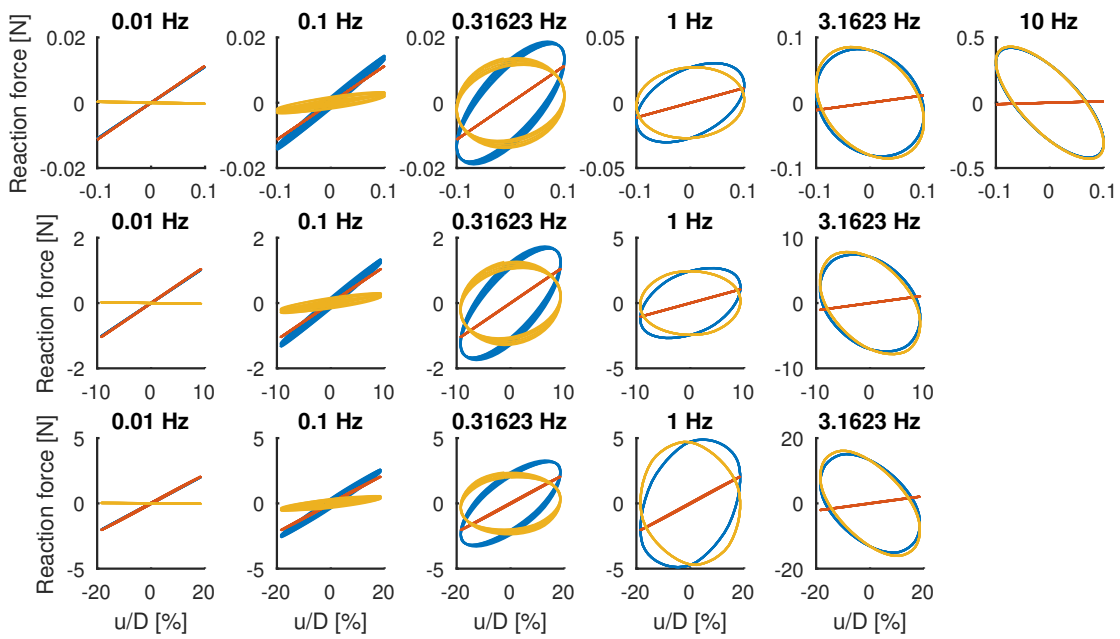
Figure 5.8: Force displacement curves obtained with the nonlinear FE model. The curves are generated for a cross-section at 20 m depth, for a soil with a shear wave velocity of 50 m/s. The two curves under 10 Hz are not included as the model could not converge for these combinations of high frequencies and large displacements.

Figure 5.9: Magnitude of the force component remaining after the subtraction of the P-Y curve determined for the static condition. The figure shows the remaining force for a depth of 20 m, for a soil with a shear wave velocity of 50 m/s.

Figure 5.10: Phase of the force component remaining after the subtraction of the P-Y curve determined for the static condition. The figure shows the remaining force for a depth of 20 m, for a soil with a shear wave velocity of 50 m/s.

Figure 5.11: text text text text text text text text text text text text text text text text text text text text text text text text text text text
.

a different method as this reaction curve is shaped as a hyperbolic tangent instead of a linear function. The static stiffness of the foundation is presented in figure 5.8. The added mass and added damping values are presented in the figures 5.11 and 5.12 respectively. The figures show resemblance to the added mass and added damping curves obtained in the linear analysis.

The added mass starts at a constant value for $\omega \to 0$. The value then increases to a maximum at the cut-off frequency (0.2 Hz), after which it drops to 0. An amplitude dependency can be observed for the frequency range below the cut-off frequency, but this seems to be minimally present in the region above this point.

The added damping starts with a amplitude dependency at $\omega \to 0$. This is related to the hysteretic and hydraulic[3] damping in the soil. The added damping contribution then falls to 0 around the cut-off frequency region, after which it sharply increases. This is because the soil shows resonance at the cut-off frequency, after which the pile starts to radiate-out waves. The added damping slowly decreases after the peak, as the damping increases slower than the frequency value. The added damping shows the increase again towards the higher frequencies. This is different from the linear results.

5.5.4.   Discussion

The results obtained for the small-strain linear case are based on several simplifications and assumptions that do not represent reality. Major points that need to be considered when using the results are:

- The applied soil model is a simplification of the actual soil behaviour. The applied nonlinear material characteristics are (1) the Mohr-Coulomb failure criteria and (2) the two-phase material properties. The first of the two only contributes when the shear strength is exceeded. This property is therefore not present in the small-strain regime. The two-phase material model adds a viscous damping to the model. The combination of the Mohr-Coulomb failure criteria with

---

[3]Hydraulic damping is related to the strain rate and would decrease to 0 for pure static loading. However, the hydraulic conductivity applied in the FE model is small enough to be still present for the lowest considered frequency (0.01 Hz).

Figure 5.12: text text text text text text text text text text text text text text text text text text text text text text text text text text
.

the coupled pore-pressure mechanical analysis could be used to model soil degradation as the excess pore pressure is determined in the soil. However, this mechanism is not present in this thesis as the model could not converge for these situations.

- The results are obtained with the 2D plane strain FE model, using a fixed far-field boundary. The model was tuned to have a cut-off frequency similar to that of the first mode of the linear plane stress model. Fixing the boundary results in resonance issues related to the natural frequencies of the considered soil disc. The nonlinear material properties showed to suppress the higher resonant frequencies quite well. The contribution of the higher modes should be further investigated.

- The linear analysis showed that the soil response is a superposition of several response modes. Possible shape modes of the soil column are not accounted for in the nonlinear analysis. The possible contribution of response modes is unknown as the superposition principle is invalid for the nonlinear case.

- The soil-pile interaction is implemented as perfectly bonded. However, the soil-pile interface could behave completely different for a nonlinear analysis. The impact of the soil-pile interface could not be investigated due to convergence issues[4].

- The presented added mass and added damping are based on the steady state response of the soil to harmonic loading. Transient effects are therefore not incorporated in the foundation parameters. This could lead to errors in a seismic analysis which is of relative short duration.

---

[4]It was found that the convergence issues were not related to the soil-pile interface conditions, but rather to a numerical instability related to the two-phase material model.

5.6.   Summary

In this chapter, the SSI for an embedded pile to harmonic motion was investigated. First, a derivation of the linear elastic lateral resistance of a soil layer was performed. This analytical expression was used to validate the 2D FE plane strain SSI model. This validation showed that the FE model correctly predicts the soil response for high frequencies, but fails to capture the response for the static case and frequencies below the cut-off frequency of the soil response mode. This is because the lateral resistance is transferred through shear stresses in the vertical direction instead of in the horizontal plane. The same analysis was performed with a nonlinear two-phase Mohr-Coulomb material model to represent the soil.

Chapter 6

Frequency-Time Domain Winkler Foundation

6.1.   Introduction

The dynamic response of systems can be analysed in both the frequency and time domain. Analysis in the frequency domain proves to be a fast and effective method for linear(ised) systems, and is therefore often preferred over the much slower time domain analysis methods. However, when nonlinear forces play a dominant role in the analysis, the linear superposition principle on which the frequency domain analysis method is based is no longer valid[1]. Moreover, frequency domain approaches are limited to a steady-state analysis (105).

When both frequency dependent as well as nonlinear properties are to be considered in a system, neither the frequency nor time domain analysis correctly captures the dynamics of the system. An option for this situation is to combine the methods in a convolution integro-differential equation, where the nonlinear effects can be added to the system at a later stage (122). Section 6.2 presents the theory behind this combined frequency-time domain modelling. In section 6.3, this so-called hybrid frequency-time domain modelling method will be used together with the frequency dependent foundation parameters as obtained in chapter 5, to simulate the response of the monopile to harmonic lateral loading. This response and the overall performance is compared to the full 3D FE model in section 6.4.

6.2.   Time-Domain Formulation of a Frequency Dependent System

This section presents the theory on which the hybrid frequency-time domain model is based. First is the time-domain formulation for a system with frequency dependent properties presented. This is followed by the state-space representation of linear systems which is used to incorporate the load-memory effect into the time domain model. There exist several methods to determine the linear system representation of the load-memory. Three of these methods are presented.

6.2.1.   Frequency-Time Relation by Convolution

The EOM for a system in the frequency domain is given as:

$$-\omega^2 \left[\mathbf{M} + \mathbf{A}(\omega)\right] \vec{X}(i\omega) + i\omega \left[\mathbf{C} + \mathbf{B}(\omega)\right] \vec{X}(i\omega) + \mathbf{K}\vec{X}(i\omega) = \vec{F}(i\omega) \tag{6.1}$$

where:

$\mathbf{M}, \mathbf{C}, \mathbf{K}$	=	Mass, damping and stiffness matrices	(-)
$\mathbf{A}(\omega), \mathbf{B}(\omega)$	=	Added mass and damping matrices	(-)
$\vec{X}$	=	Complex response amplitude	(m)
$\vec{F}$	=	External force	(N)

---

[1]Higher order frequency domain methods exist based on multilinear frequency response functions. However, these methods are often impractical.

In the case of nonlinear analysis, equation 6.1 has to be converted into the time domain form. In this form, nonlinear and time dependent effects can be added to the EOM. However, the time domain formulation as in equation 6.1 cannot be directly converted into this form as the added mass and added damping matrices, **A** and **B**, are frequency dependent. A different approach is therefore necessary.

Based on the assumption that the system is an initial value problem, equation 6.1 is considered to be dependent of the general Laplacian state parameter s. Written out, the equation takes the form of:

$$s^2 \mathbf{M} \vec{X}(s) + s^2 \mathbf{A}(s) \vec{X}(s) + s\mathbf{C} \vec{X}(s) + s\mathbf{B}(s) \vec{X}(s) + \mathbf{K} \vec{X}(s) = \vec{F}(s) \tag{6.2}$$

Considering:

$$\mathscr{L}^{-1}\{s^n F(s)\}(t) = \frac{\mathrm{d}^n}{\mathrm{d}t^n} f(t) \tag{6.3}$$

$$\mathscr{L}^{-1}\{G(s) \cdot F(s)\}(t) = \int_0^t g(t-\tau) f(\tau) d\tau, \qquad 0 \le t < \infty \tag{6.4}$$

equation 6.2 can be transferred to the time domain by applying the inverse Laplace transform, making it a vector integro-differential equation:

$$\mathscr{L}^{-1}\{s^2 \mathbf{M} \vec{X}(s) + s^2 \mathbf{A}(s) \vec{X}(s) + s\mathbf{C} \vec{X}(s) + s\mathbf{B}(s) \vec{X}(s) + \mathbf{K} \vec{X}(s)\}(t) = \mathscr{L}^{-1}\{\vec{F}(s)\}(t) \tag{6.5a}$$

$$\mathbf{M} \ddot{\vec{x}}(t) + \int_0^t \mathbf{A}(t-\tau) \ddot{\vec{x}}(\tau) d\tau + \mathbf{C} \dot{\vec{x}}(t) + \int_0^t \mathbf{B}(t-\tau) \dot{\vec{x}}(\tau) d\tau + \mathbf{K} \vec{x}(t) = \vec{F}(t) \tag{6.5b}$$

Here, the convolution integrals account for the so-called load memory effect of the system, as these describe how an impulse loading at a particular point in time affects the response from there on. It must be noted that the response is the summation of the interaction of the DOF with the harmonics from the impulse responses. Meaning that the DOF is loaded with the response from all frequencies, but that the loading corresponding to frequencies not present in the DOF are counterbalanced.

Equation 6.5b contains two convolution integrals, which is from a computational view undesirable for 2 reasons:

- Methods for the analysis of the convolution integrals in e.g. finite element software require often additional computational power.
- The convolution integral describing the load memory effect of the added mass component contains a second time derivative term of the perturbation. In the time integration method applied in a FEA, this is the state calculated from the EOM. Having a term in the EOM dependent on the to be determined acceleration vector requires an iterative procedure, leading to an significant increased computational time (51).

Since the convolutions are linear operations and therefore commutative, equation 6.5b can be simplified for increased computational efficiency. Using the relationship for convolution differentiation, the acceleration dependent term can be rewritten as a function of the velocity state of the system:

$$\frac{\partial}{\partial t}(A * \dot{x}) = \int_0^t \mathbf{A}(\tau) \frac{\partial}{\partial t} \dot{\vec{x}}(t-\tau) d\tau = \int_0^t \frac{\partial}{\partial t} \mathbf{A}(t-\tau) \dot{\vec{x}}(\tau) d\tau \tag{6.6}$$

The convolution terms in equation 6.5b can then be rearranged using the distributivity of the terms:

$$\int_0^t \mathbf{A}(t-\tau) \ddot{\vec{x}}(\tau) d\tau + \int_0^t \mathbf{B}(t-\tau) \dot{\vec{x}}(\tau) d\tau = \int_0^t \left[\frac{\partial}{\partial t} \mathbf{A}(t-\tau) + \mathbf{B}(t-\tau) \right] \dot{\vec{x}}(\tau) d\tau \tag{6.7}$$

It is convenient to replace the two impulse response terms in the right hand side of equation 6.7 with a single response function **R**, known as the retardation function (105). The complete EOM from equa-

tion 6.5b can then be expressed by only a single convolution integral:

$$\mathbf{M}\ddot{\vec{x}}(t) + \mathbf{C}\dot{\vec{x}}(t) + \mathbf{K}\vec{x}(t) + \int_0^t \mathbf{R}(t-\tau)\dot{\vec{x}}(\tau)d\tau = \vec{F}(t) \tag{6.8}$$

$$\mathbf{R}(t-\tau) = \frac{\partial}{\partial t}\mathbf{A}(t-\tau) + \mathbf{B}(t-\tau) \tag{6.9}$$

When the frequency dependent values of the system are obtained in the frequency domain with e.g. a FEA, the retardation function can be constructed directly from the data. This follows from rearranging the terms in equation 6.2 leading to the convolution integrals:

$$s^2\mathbf{A}(s)\vec{X}(s) + s\mathbf{B}(s)\vec{X}(s) \tag{6.10}$$

$$[s\mathbf{A}(s) + \mathbf{B}(s)]\,s\vec{X}(s) \tag{6.11}$$

Replacing the general Laplacian state parameter s with the harmonic frequency parameter, $i\omega$, the real valued retardation function is then obtained via the Bromwich integral:

$$\mathbf{R}(t) = \mathbb{Re}\left\{\frac{1}{2\pi i}\int_0^\infty e^{i\omega t}\,[i\omega\mathbf{A}(\omega) + \mathbf{B}(\omega)]\,d\omega\right\} \tag{6.12}$$

The EOM as in the form of equation 6.8 is usually the basis for time domain models of marine structures based on frequency domain data (105). For marine structures, the hydrodynamic damping can be fully described by the radiation forces and the added mass approaches a asymptote for $\omega \to \infty$. The EOM in hydrodynamic analysis is therefore often represented by equation 6.13, known as the Cummins equation (20).

$$[\mathbf{M} + \mathbf{A}(\infty)]\,\ddot{\vec{x}}(t) + \int_0^t \mathbf{R}(t-\tau)\dot{\vec{x}}(\tau)d\tau + \mathbf{K}\vec{x}(t) = \vec{F}(t) \tag{6.13}$$

Where the relations between the time and frequency domain parameters are given by the Kramers-Kronig relations:

$$\mathbf{R}(t) = \frac{2}{\pi}\int_0^\infty \mathbf{B}(\omega)\cos(\omega t)d\omega \tag{6.14a}$$

$$\mathbf{A}(\omega) = \mathbf{A}(\infty) - \frac{1}{\omega}\int_0^\infty \mathbf{R}(t)\sin(\omega t)dt \tag{6.14b}$$

$$\mathbf{B}(\omega) = \int_0^\infty \mathbf{R}(t)\cos(\omega t)dt \tag{6.14c}$$

Properties of the Convolution

The retardation function, equation 6.12, represents the systems response to a unit impulse load in the case of perturbations form the equilibrium position. The presented form combines both the added mass effect as the frequency dependent damping component. This is possible as the velocity is the anti-derivative of the acceleration. Since the physical meaning of the function is the impulse response, there are properties that have to be satisfied for a stable system.

Time Domain Properties

The required properties of the retardation function in the time domain are based on the stability of the convolution terms.

- The impulse response has to be real valued.

$$\mathbf{R}(t) < \infty, \qquad \text{for } t \in [0, \infty\rangle \tag{6.15}$$

- The impulse response should vanish at $t \to \infty$.

$$\lim_{t \to \infty} \mathbf{R}(t) = 0 \tag{6.16}$$

This is true for Fourier and Laplace transforms according to the Riemann-Lebesque lemma (105).

In a general sense, these criteria state that the impulse response should not lead to an infinite force input in the convolution terms.

Frequency Domain Properties

The properties of the retardation function in the frequency domain are directly related to the added mass and potential damping functions. Characteristics of the Cummins' equation, which also hold for the general case, are given in a paper by (105). These are:

- The value of the retardation function for the static case ($\omega \to 0$) should approach 0.

$$\lim_{\omega \to 0} \mathbf{R}(\omega) = \lim_{t \to 0} [i\omega \mathbf{A}(\omega) + \mathbf{B}(\omega)] = 0 \tag{6.17}$$

This is true when:

$$\lim_{\omega \to 0} i\omega \mathbf{A}(\omega) = 0 \tag{6.18a}$$

$$\lim_{\omega \to 0} \mathbf{B}(\omega) = 0 \tag{6.18b}$$

- The value of the retardation function for $\omega \to \infty$ should approach 0 to ensure the convergence of the transformation integral.

$$\lim_{\omega \to \infty} \mathbf{R}(\omega) = \lim_{t \to \infty} [i\omega \mathbf{A}(\omega) + \mathbf{B}(\omega)] = 0 \tag{6.19}$$

This is true when:

$$\lim_{\omega \to \infty} \mathbf{B}(\omega) = 0 \tag{6.20}$$

The value of the added mass contribution when the limit approaches ∞ can be found as:

$$\lim_{\omega \to \infty} \mathbf{A}(\omega) = \lim_{\omega \to \infty} \frac{1}{i\omega} [\mathbf{R}(\omega) - \mathbf{B}(\omega)] = \lim_{\omega \to \infty} \frac{-1}{2\pi\omega} \int_0^\infty e^{-i\omega t} [\mathbf{R}(t) - \mathbf{B}(t)] \, dt = 0 \tag{6.21}$$

This also follows from the Riemann-Lebesque lemma.

Passivity and Stability of the Retardation Function

The convolution part has to be stable for a proper implementation of the extra frequency dependent term in the EOM. A usefull feature for this is to examine the passivity of the system. A passive system, in contrary to an active system, can only store or dissipate energy. This means that the systems states will stay constant or eventually return to the equilibrium position.

The transfer function, $\mathbf{H}(s)$, of a linear system is given by:

$$\vec{Y}(s) = \underbrace{\left[\mathbf{C}' \left(s\mathbf{I} - \mathbf{A}' \right)^{-1} \mathbf{B}' + \mathbf{D}' \right]}_{H(s)} \vec{U}(s) \qquad \underset{\longleftrightarrow}{\text{transform}} \qquad \begin{array}{l} \dot{\vec{x}}(t) = \mathbf{A}' \vec{x}(t) + \mathbf{B}' u(t) \\ y(t) = \mathbf{C}' \vec{x}(t) + \mathbf{D}' u(t) \end{array} \tag{6.22}$$

The system is said to be passive if the poles of the frequency response function, $\mathbf{H}(s)$, have a zero or negative real part. This is achieved when the matrix is positive and real. Thus, the retardation function is passive if the matrix is positive real:

$$\mathbf{R}(i\omega) + \mathbf{R}^*(i\omega) \geq 0, \qquad \forall \omega \in \mathbb{R} \tag{6.23}$$

Since the retardation function is a combination of the added mass derivative and the added damping, the passivity of the system is guaranteed when the added damping matrix is positive real, as presented in equations 6.24-6.25.

$$\mathbf{R}(\omega) = i\omega\mathbf{A}(\omega) + \mathbf{B}(\omega) \tag{6.24}$$

$$\mathbf{B}(\omega) = \mathbf{B}^{\mathsf{T}}(\omega) \geq 0 \tag{6.25}$$

6.2.2. State-Space Representation of Linear Systems

The state-space representation is popular in control engineering as it is a convenient way of describing a linear system as a set of first order ODE. The variable in the first order ODE is referred to as a state variables of the system. The state variables are the smallest possible subset of system variables that can represent the state of a system.

The State-Space Model

A linear dynamic system can be represented in various ways. The classical way is in the form of a (non-homogeneous) ODE. For a single input single output (SISO) system, as the case for the retardation function, the ODE could take the form of:

$$\frac{d^n y(t)}{dt^n} + \ldots + a_1 \frac{dy(t)}{dt} + a_0 y(t) = b_n \frac{d^n u(t)}{dt^n} + \ldots + b_1 \frac{du(t)}{dt} + b_0 u(t) \tag{6.26}$$

where:

u	=	Excitation (SISO system)	(-)
y	=	Response (SISO system)	(-)

Taking the Laplace transform of equation 6.26 gives:

$$Y(s)\left(s^n + \ldots + sa_1 + a_0\right) = U(s)\left(s^n b_n + \ldots + sb_1 + b_0\right) \tag{6.27}$$

with its corresponding transfer function:

$$\frac{Y(s)}{U(s)} = H(s) = \frac{s^n b_n + s^{n-1} b_{n-1} + \ldots + sb_1 + b_0}{s^n + s^{n-1} a_{n-1} + \ldots + sa_1 + a_0} \tag{6.28}$$

This transfer function holds the characteristics of the system and is therefore extensively used in control engineering. The roots of the polynomials in the numerator and denominator of equation 6.28 hold the zeros and the poles of the system respectively.

The order of the system is given by the highest degree in the denominator of the transfer function. This order gives the required number of degrees or states to represent the dynamics of the system. The difference in order between the numerator and the denominator is called the relative degree of the system. This relative degree can be used to determine the initial value of the impulse response (105). Using the initial value theorem of the Laplace tranfsorm gives:

$$\lim_{t \to 0} h(t) = \lim_{s \to \infty} sH(s) \tag{6.29}$$

From this equation it follows that $h(0)$ is non-zero only for a relative degree of 1.

As mentioned before, the order of the transfer function gives the number of states in the system. These states can be conveniently found by decomposing the higher order ODE into a set of first order ODEs. The SISO system from equation 6.26 would take the form:

$$\dot{\vec{z}}(t) = \mathbf{A}'\vec{z}(t) + \mathbf{B}'u(t)$$
$$y(t) = \mathbf{C}'\vec{z}(t) + \mathbf{D}'u(t) \tag{6.30}$$

where:

$\mathbf{A}', \mathbf{B}', \mathbf{C}', \mathbf{D}'$	=	State-space linear relation matrices	(-)
$\vec{z}$	=	State variables of the system	(-)

The state-space representation of linear system can be easily[2] obtained from the higher order ODE or transfer function by rewriting it in the controllable canonical form (CCF). Doing this leads to the following expressions for the state's linear relation matrices:

$$\mathbf{A}' = \begin{bmatrix} 0 & 1 & 0 & \ldots & 0 \\ 0 & 0 & 1 & \ldots & 0 \\ \vdots & \vdots & \vdots & \ddots & \vdots \\ 0 & 0 & 0 & \ldots & 1 \\ -a_0 & -a_1 & -a_2 & \ldots & -a_{n-1} \end{bmatrix}, \quad \mathbf{B}' = \begin{bmatrix} 0 \\ 0 \\ \vdots \\ 0 \\ 1 \end{bmatrix}, \quad \mathbf{C}' = \begin{bmatrix} b_0 & b_1 & \ldots & b_{n-1} \end{bmatrix}, \quad \mathbf{D}' = \begin{bmatrix} b_n \end{bmatrix}$$

$$\text{(6.31)}$$

Note that there is an infinite number of equivalent space state models which hold the same model characteristics. Implementation is therefore not limited to the presented canonical form.

The transfer function of the state-space representation (equation 6.30) can be obtained with the Laplace transform and was given in equation 6.22. Applying the inverse Laplace transformation to this transfer function results in the impulse response of the system based on the state-space representation:

$$H(s) = \mathbf{C}' \left(s\mathbf{I} - \mathbf{A}' \right)^{-1} \mathbf{B}' + \mathbf{D}' \tag{6.32}$$

$$h(t) = \int_0^\infty e^{st} \mathbf{C}' \left(s\mathbf{I} - \mathbf{A}' \right)^{-1} \mathbf{B}' \, ds = \mathbf{C}' e^{\mathbf{A}' t} \mathbf{B}' \tag{6.33}$$

The general solution can be found in a similar form based on the method of solving a set of non-homogeneous first order ODEs with the matrix exponential:

$$y(t) = \mathbf{C}' e^{\mathbf{A}' t} z(0) + \int_0^t \mathbf{C}' e^{\mathbf{A}'(t-\tau)} \mathbf{B}' u(\tau) \, d\tau \tag{6.34}$$

6.2.3.   State-Space Convolution Representation

The implementation of a convolution integral in time domain models can be computationally inefficient due to the required integration of the loading history. For this reason, state-space description of the convolution part in the EOM is a convenient method as it only requires the current states for the time integration method.

Various representations exist for the replacement of the convolution with a state-space model. The general higher order method is presented in equation 6.35a. The alternative representations are lower order approximations or often dedicated to a specific analysis case.

$$(\mathbf{M} + \mathbf{A}(\infty)) \ddot{\vec{x}}(t) + (\mathbf{C} + \mathbf{B}(\infty)) \dot{\vec{x}}(t) + \mathbf{K} x(t) + \vec{F}_R(t) = \vec{F}(t) \tag{6.35a}$$

$$\dot{\vec{z}}(t) = \mathbf{A}' \vec{z}(t) + \mathbf{B}' \dot{\vec{x}}(t)$$
$$\vec{F}_R(t) = \mathbf{C}' \vec{z}(t) + \mathbf{D}' \dot{\vec{x}}(t) \tag{6.35b}$$

where:

$\vec{x}$	=	State variables of the str	(-)
$\vec{F}_R$	=	Retardation's force component	(-)

The state-space's of the system can be solved directly linked in a single matrix. Note that there is not a single convolution replacement model, but that there is a separate model for every convolution term in the EOMs.

---

[2]In the case of a strictly proper transfer functions.

Since the model is directly linked, the solution found with equation 6.30 is mathematically exact. However, this does not imply that the represented physical model is exact as well. The accuracy of the model is strongly dependent on how well the physical system can be described with a linear model and how well the impulse response is represented.

6.2.4. System Identification

As mentioned in the previous section, the accuracy of the state space model depends on the quality of the systems reproduced characteristics. Various methods exist to get to a state-space representation of the systems. Usually, these methods exist of the following steps:

1. Analyse systems response data
2. Determine model order
3. Perform parameter estimation
4. Check stability of state-space representation

This thesis focuses on the approach that makes use of the frequency response function of the convolution terms.

The systems response data can be obtained from test or FE simulations. This data should contain sufficient information to be able extract the impulse response and transfer function.

Transfer Function Estimation

Systems show similar behaviour when the transfer functions are similar. Therefore, the parameter estimation methods as applied in the replacement of convolution integrals is based on the fitting of this transfer function. (105) presents 3 methods to determine the unknown model parameters. These are:

1. Frequency domain regression
2. Impulse response fitting
3. System realisation

The methods are discussed in the following sections.

Frequency Domain Regression

The frequency domain regression method is based on the minimisation of polynomial fitting of the transfer function. The transfer function, defined as:

$$\frac{Y(s)}{U(s)} = H(s) = \frac{s^n b_n + s^{n-1} b_{n-1} + \ldots + s b_1 + b_0}{s^n + s^{n-1} a_{n-1} + \ldots + s a_1 + a_0} \tag{6.36}$$

has the unknown parameters:

$$\theta = \begin{bmatrix} b_n & \ldots & b_0 & a_{n-1} & \ldots & a_0 \end{bmatrix}^\mathsf{T} \tag{6.37}$$

The system's states can then be found by performing non-linear least-squares fitting to the desired frequency response function. (105) present the following least-squares function:

$$\theta^* = \arg \min_\theta \sum_j w_j \left| H(i\omega_j) - \frac{Y(i\omega_j, \theta)}{U(i\omega_j, \theta)} \right|^2 \tag{6.38}$$

Since the problem is nonlinear of nature, the minimisation has to be performed in an iterative manner. Various algorithms exist to perform this operation. Also, when this method is applied the user has to manually decide on the order of the polynomial to fit the curve. This is a matter of trial and error and the users own judgement. When choosing an order, one has to keep in mind: the stability of the model, the accuracy of the model and the computational time required for the total number of DOF.

Impulse Response Fitting

The impulse response fitting approach is in many ways similar to the transfer function response fitting method. Here, the systems parameters are fitted to the impulse response in the time-domain instead of the transfer function in the frequency domain. As presented in section 6.2.2.1, the impulse response of a state space model is given as equation 6.32. The impulse response of a general state-space model[3] with parameters defined as in equation 6.37 is given as:

$$h(t,\theta) = \mathbf{C}'(\theta) e^{\mathbf{A}'(\theta)t} \mathbf{B}'(\theta) \tag{6.39}$$

Similar to the transfer function approach, the parameters can be determined with a non-linear least-squares method. In this case, the minimisation function would take the form of:

$$\theta^* = \operatorname*{argmin}_{\theta} \sum_j w_j \left| h(t_j) - h(t_j, \theta) \right|^2 \tag{6.40}$$

Again, for this method, the order of the system has to be manually chosen beforehand. Keeping the same requirements in mind as stated in the frequency domain regression methods section.

System Realisation

The system realisation method is based on the minimisation of the Markov parameters (43). The method is based on finding the minimal discrete state matrices that result in the wanted impulse response when used in a first order Markov chain. The discrete state matrices (or Markov parameters) show similarity. The difference is that the discrete state-space system gives the new states of the system as a matrix multiplication of the previous state, making it an operation, while an operation of the continuous system would result in the derivatives. The latter requires therefore an integration scheme or e.g. a solution based on the matrix exponential. The systems Markov parameters are given by:

$$h_d(N) = \bar{\mathbf{C}}\bar{\mathbf{A}}^{N-1}\bar{\mathbf{B}} + \bar{\mathbf{D}}, \qquad N = 1, 2, \dots \tag{6.41}$$

where:

$\bar{\mathbf{A}}, \bar{\mathbf{B}}, \bar{\mathbf{C}}, \bar{\mathbf{D}}$	=	Markov parameter matrices	(-)
h_d	=	Discrete impulse response	(-)

The discrete state-space system then becomes:

$$x(N+1) = \bar{\mathbf{A}}x(N) + \bar{\mathbf{B}}u(N) \tag{6.42a}$$

$$y(N) = \bar{\mathbf{C}}x(N) + \bar{\mathbf{D}}u(N) \tag{6.42b}$$

An approximate minimal state-space realisation of the wanted impulse response can be obtained though the Hankel singular value decomposition (SVD) method, as proposed by (68). The hankel matrix, and its Markov parameter factorisation, are defined as:

$$\Gamma = \begin{bmatrix} H_1 & H_2 & H_3 & \dots & H_N \\ H_2 & H_3 & H_4 & \dots & 0 \\ H_3 & H_4 & H_5 & \dots & 0 \\ \vdots & \vdots & \vdots & \ddots & 0 \\ H_N & 0 & 0 & \dots & 0 \end{bmatrix} = \begin{bmatrix} \bar{\mathbf{C}} \\ \bar{\mathbf{C}}\bar{\mathbf{A}} \\ \bar{\mathbf{C}}\bar{\mathbf{A}}^2 \\ \vdots \\ \bar{\mathbf{C}}\bar{\mathbf{A}}^{N-1} \end{bmatrix} \begin{bmatrix} \bar{\mathbf{B}} & \bar{\mathbf{A}}\bar{\mathbf{B}} & \bar{\mathbf{A}}^2\bar{\mathbf{B}} & \dots & \bar{\mathbf{A}}^{N-1}\bar{\mathbf{B}} \end{bmatrix} \tag{6.43}$$

There are several algorithms to determine the discrete state space realisations. A popular approach is the SVD of the Hankel matrix:

$$\Gamma = \mathbf{U}\Sigma\mathbf{V}^* = \begin{bmatrix} \mathbf{U}_1 & \mathbf{U}_2 \end{bmatrix} \begin{bmatrix} \Sigma_1 & 0 \\ 0 & \Sigma_2 \end{bmatrix} \begin{bmatrix} \mathbf{V}_1^* \\ \mathbf{V}_2^* \end{bmatrix} \approx \mathbf{U}_1\Sigma_1\mathbf{V}_1^* \tag{6.44}$$

---

[3]In the case of a strictly proper transfer functions.

where:

$\mathbf{U}, \mathbf{V}$	=	Mode shapes of the singular values	(-)
Σ	=	Singular values	(-)

The separation into the submatrices 1 and 2 in equation 6.44 allow for a order reduction based on the weight of the calculated singular values. Usually, the size of Σ would give the order of the system. However, possible nonlinearity and numerial errors can result in a matrix of full rank. A desired order can therefore be chosen based on the weight of the singular values, as long as it results in a stable system.

Next, the discrete state-space are to be computed from the SVD matrices. The description proposed by (68) is:

$$\bar{\mathbf{A}} = \Sigma_1^{-\frac{1}{2}} \bar{\mathbf{U}} \Sigma_1^{-\frac{1}{2}}, \qquad \bar{\mathbf{B}} = \Sigma_1^{-\frac{1}{2}} \mathbf{V}_{11}^*, \qquad \bar{\mathbf{C}} = \mathbf{U}_{11} \Sigma_1^{-\frac{1}{2}}, \qquad \bar{\mathbf{D}} = H_0 \tag{6.45}$$

where:

$$\bar{\mathbf{U}} = \begin{bmatrix} \mathbf{U}_{11} \\ \mathbf{U}_{12} \end{bmatrix}^\top \begin{bmatrix} \mathbf{U}_{12} \\ \mathbf{U}_{13} \end{bmatrix}, \qquad \mathbf{U}_1 = \begin{bmatrix} \mathbf{U}_{11} \\ \mathbf{U}_{12} \\ \mathbf{U}_{13} \end{bmatrix}, \qquad \mathbf{V}_1 = \begin{bmatrix} \mathbf{V}_{11} \\ \mathbf{V}_{12} \\ \mathbf{V}_{13} \end{bmatrix} \tag{6.46}$$

Finally, the discrete state-space realisation has to be converted to a continuous time system to be able to implement it in the EOM. This can be done with the inverse Tustin transform, or bilinear transformation (2).

6.3. Hybrid Frequency-Time Domain Model

The method as presented in the previous section is applied to the Winkler-beam model which was introduced in chapter 4. The retardation functions for the various soil layers are obtained from the frequency response of the soil as determined in chapter 5. This retardation function is then represented by a linear system which is integrated into the Winkler-beam model.

6.3.1. Retardation Function

The retardation functions for the foundation elements are found by applying the discrete Fourier transform, equation 6.47, to the soil response parameters obtained in chapter 5. The small-strain soil response is used to determine the retardation function as applied in this chapter.

$$R(t) = \frac{1}{n} \sum_{j=1}^{n} \left(i\omega_j \mathbf{A}(\omega_j) + \mathbf{B}(\omega_j) \right) e^{2\pi i \omega_j t} \tag{6.47}$$

The retardation function represents the impulse response from the soil to a unit velocity loading. Figure 6.1 shows the functions for various depths. The shown plots are the "actual" or continuous time retardation functions based on the generated response data.

The retardation functions in figure 6.1 show a high level of similarity between them. The magnitude of the functions varies with depth while the shapes are almost the same. The curves decay to 0 in approximately 6 seconds. The discrete time step of the impulse response is chosen to be 0.005 seconds, which is based on 20 times the highest considered frequency.

6.3.2. System Identification

The convolution term containing the retardation function is represented by a linear system in the hybrid model. The convolution term represents a force in the EOM. This force is taken as the output of the to be determined dynamic system. Various methods exist to determine this system, as presented in chapter 3. The method applied in this thesis is the system realisation method.

Figure 6.1: The retardation functions for various depths with corresponding damping constant.
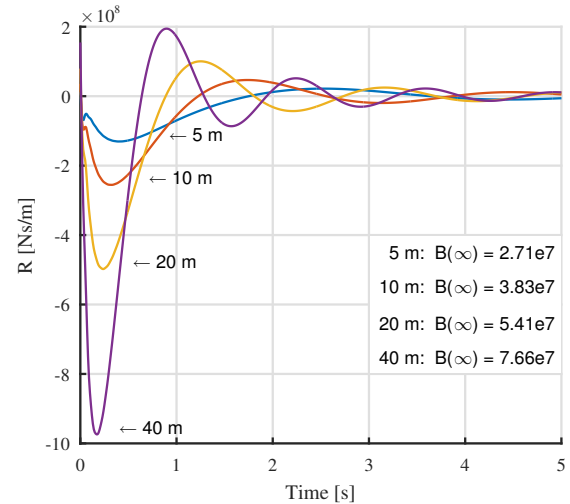
Figure 6.2: The singular values for the Hankel SVD of the retardation function. Upper pane shows the singular values and the bottom pane shows the cumulative energy contribution of the associated dynamic modes.
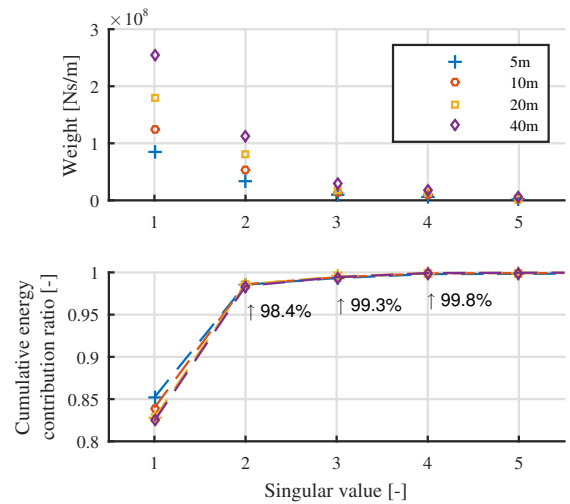

Model Order

The Hankel matrix is constructed from a discretisation of the retardation functions as presented in figure 6.1. A Hankel SVD is performed on this matrix to decompose the function into its principal dynamic components. From these components, the discrete time Markov parameters can be constructed. The decomposition leads to a dynamic system with an order equal to the size of the discrete impulse series. The model can be reduced by ignoring any non-significant modes. The importance or weight of the modes is given by the singular values obtained from the SVD decomposition. The singular values obtained from the decomposition of the retardation functions are presented in figure 6.2.

The figure shows that the largest weight of the retardation function's singular values is in the first two modes. This makes sense as the response of the soil was determined from a linear harmonic closed-form solution. The singular values for the retardation function based on the nonlinear foundation parameters are without a clear transition between principal components and noise. This can be the case for non-linear systems whose behaviour shows transitions from one state to another. Since the order of the system is in that case not clear from the singular values, an energy based method is used. The singular values are defined as the rooted eigenvalues of the co-variance matrix of the Hankel matrix. Meaning that they represent the variance of the dynamic motions in the system. An energy based comparison between the relative contribution of each mode can be made by squaring the singular values. The normalised cumulative contribution is presented in the lower graph of figure 6.2. The order of the dynamic system representing the retardation function is based on a 99% energy basis. This results in models of the order 3 for the linear foundation parameters and 8 for the nonlinear foundation

Figure 6.3: Poles and zeros for the Winkler-beam model combined with the linear representation of the retardation function. All the values are located in the left half plane.
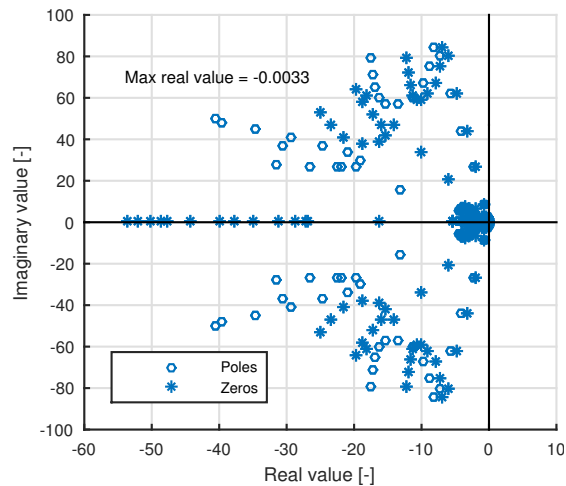
parameters.

6.3.3. State-Space Representation

The 3 and 8 order state-space representations are generated from the continuous time retardation function with the method as proposed by (68). This is done for the depths of 5, 10, 20 and 40 meter. However, the number and the location of the nodes is dependent of user input and therefore not constant. A linear interpolation of the polynomial parameters of the retardation function is used to determine the systems parameters for the intermediate elements. The interpolation of the polynomial parameters gives the shifting of peaks in the retardation function, instead of averaging them between two data sets. There is a state-space system generated for every foundation beam element in this way.

The elements between the seabed and 5 meter depth are interpolated between the 5 meter data set and a "static" model which results in 0 output force. The validity of this approach is unknown, but, since other SSI mechanisms, e.g. wedging, are expected near the surface was this considered to be of minor concern.

Implementation

- matrix

Stability and Quality of the Representations

The internal stability of a state space system, as in equation 6.30, is guaranteed when the eigenvalues of the matrix $\mathbf{A}'$ are all stable. This means that all eigenvalues should have a negative real component. In the case of a transfer function, the stability can be determined from the roots of the polynomials. The poles and zeros for the generated state-space representations are plotted in figure 6.3. All values are located in the left half plane, and are therefore stable.

6.4. Laterally Loaded Monopile Behaviour

This section presents the results generated with the hybrid frequency-time domain Winkler foundation. The results are compared to the results of the linearised 3D FE model and the regular Winkler foundation model.

6.4.1. Static Pile Deflection

The static pile deflection for the Frequency-time domain Winkler-beam model, the linearised 3D FE model and the regular Winkler-beam model is presented in figure 6.4a. The deflection is purely based

on the stiffness matrices of the models as the mass and damping terms are not present in a static analysis. The two Winkler foundation models show therefore identical response.

(a) Uncorrected   (b) Corrected for the longer soil column.
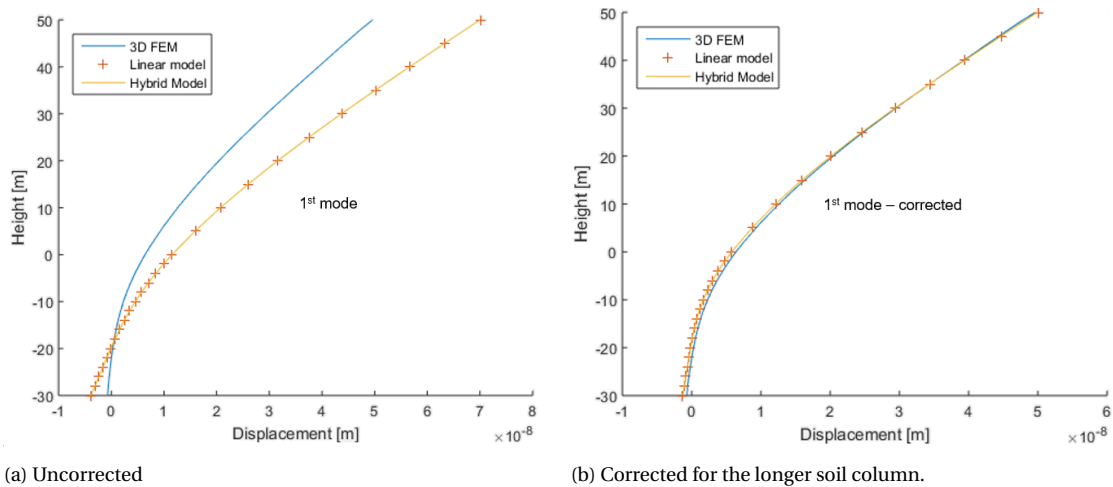
Figure 6.4: Pile displacements for a static loading of 1 N at the top of the monopile (50 above mudline).

The foundation stiffnesses for the models in figure 6.4a are based on the assumption that only the first soil resistance mode is present. The figure shows a difference between the deflection curves, implying that the foundation stiffness of that of the Winkler type models is lower than that of the full 3D model. A possible explanation could be the way the soil column is accounted for in the plane stress SSI model. Since the soil column continues below the bottom of the pile instead of being a rigid base, the implemented soil response is too low. Applying a correction factor based on the overestimated column deflection would lead to the scaling of the stiffness associated with the mode. However, note that for the static case the scaling of a single mode or the superposition of various is identical as they are collinear for a single frequency. The pile deflections for the corrected soil stiffness is presented in figure 6.4b.

Figure 6.4b shows a good fit between the static deflection the Winkler-beam model and the full 3D FE model. This implies that the beam elements match the stiffness of the with shell elements modelled monopile and that the linear Winkler springs match the full 3D foundation resistance.

### 6.4.2.   Harmonic Pile Response

The frequency response functions of the three models are plotted in figure 6.5. The response functions represent the amplitude at the top of the monopile (+50 m above seabed) to harmonic lateral loading at this same location.

The frequency response function of the combined frequency-time domain Winkler model is based on the assumption that only the first mode shape is present in the system. This assumption could be considered valid for the frequency range below the first natural frequency of the system, in case the monopile (MP) acts stiff. From the figure it becomes clear that the implementation of the frequency dependent foundation parameters introduces a significant amount of damping into the system. The peak of the undamped Winkler foundation is reduced and shifted to the right past the resonance peak of the 3D FE model. The response of the models for the higher frequencies converge to 0, as the behaviour is dominated by the inertia of the pile.

6.5.   Summary

In this chapter, the implementation of the frequency dependent foundation properties into the BNWF was presented. First, the theory behind time domain analysis with frequency dependent parameters was discussed. The used method is based on the representation of the convolution terms, emerging from the Laplace transform, by a state-space description of a linear system. This theory was applied to

Figure 6.5: Comparison of the frequency response between the combined frequency-time domain Winkler model, the 3D FE model and the regular Winkler-beam model. The response was determined for the same location the load was applied, in the horizontal direction at the top of the monopile.
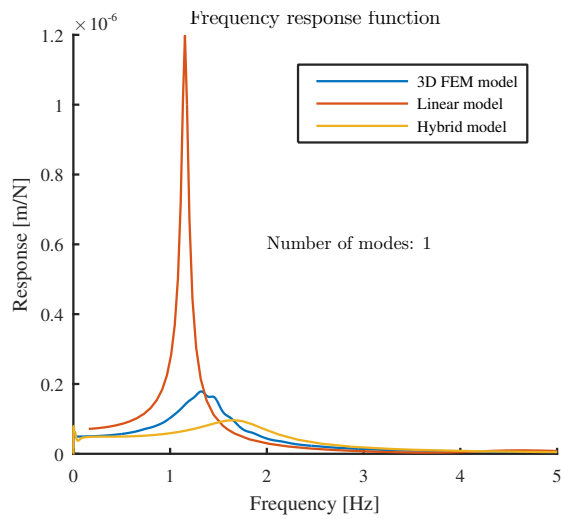
develop a combined frequency-time domain extension for the seismic Winkler-beam model. Finally, the response to harmonic loading was compared for this combined frequency-time domain model, the full 3D FE model and a regular Winkler-beam model.

Chapter 7

Conclusions, Discussion and Recommendations

7.1. Conclusions

This thesis investigated a 1D seismic Winkler foundations that is able to represent the SSI during an earthquake. The implementation of the seismic loads was achieved by coupling a BNWF with a non-linear ground response model. This approach showed to be a computationally efficient and reliable. The uncertainty in this method lies primarily within the formulation of the nonlinear soil and SSI behaviour. Although various SSI formulations have been developed, no complete satisfactory description for piles in liquefiable grounds exists. This is due to the high complexity of the nonlinear soil behaviour during seismic loading. Developed macro-element formulations are limited to a single situation as they are tuned to full 3D FE modelling or experiments. The use of a p-multiplier can represent the stress ranges of a pile in a liquefied soil column, but fails to capture any transient effects.

One of the major uncertainties in the seismic analysis of piles is identified to be related to the SSI. In order to assess these uncertainties, the dynamic properties of a 2D horizontal cross-section of an embedded monopile were determined. It was found that the developed 2D plane strain FE model was unable to capture the complete response of the soil. The model with viscous non-reflecting boundaries could not provide any static resistance, while attempts to fix the boundaries led to resonance issues. Further investigation with a 3D (plane stress) model showed that the lateral force is transferred through shear forces to the bedrock instead of to the outer edge of the considered cross-section. Therefore, a 3D analysis needs to be performed to determine the static resistance of the foundation. However, the plane strain and plane stress approach show the same response for high frequencies, indicating that the soil layers behave uncoupled for the frequency range above the natural frequencies of any distinct eigenmodes of the soil column.

The results from the harmonic plane stress analysis could not be directly implemented in a time-domain analysis, as the response of the soil is based on the superposition of the excited soil modes. The excitation of these modes is in turn related to the modes of the pile, which is a function of the response of the soil. An iterative procedure is therefore required. Moreover, the mode superposition principle does not hold for nonlinear analysis, making the applicability of the plane stress approach questionable for nonlinear seismic analysis.

A 2D plane strain FE model was used to determine the nonlinear response of a two-phase soil model with a Mohr-Coulomb yield surface. Two issues were identified for this method. The first issue was addressed above: the model could not determine the static resistance. Using fixed boundary conditions at the far-field edge of the soil in order to solve this resulted in resonance issues. The eigenmodes of the model with finite boundaries become present in the harmonic response. The second issue is the loss of any transient information. The foundation parameters are determined from the steady-state response of the soil. The transient effect, which might be important for seismic analysis, is therefore not included in the model.

A combined frequency-time domain extension for the Winkler foundation was developed to incorporate the obtained frequency-dependent foundation properties into a time-domain analysis. It was

found that the extended model reasonably predicts the dynamics of the system in case of a linear analysis. However, the method as applied in this thesis is unable to capture the true dynamics of a 3D soil medium. This is due to the dependency of the response on the excited modes. In its current form, the method can only determine the dynamics when the Fourier composition of the modes is known over time.

Using the foundation parameters obtained from the nonlinear harmonic analysis in the combined frequency-time domain extension resulted in a significant difference in behaviour compared to the full 3D FE model. The method requires multiple processing steps, which results in the accumulation of errors and complicates tracing their origin. One of the possible reasons for the difference in dynamic response could be assigned to the steady-state response of the foundation parameters. This is to be investigated. In its current form, the combined frequency-time domain method is impractical for the analysis of the transient behaviour during seismic loading.

In conclusion: The seismic analysis of monopile foundations can be performed quite accurately in 1D for the linear small-strain regime. Closed-form solution of the foundation's response can be used to determined the dynamics of the structure and the soil in the frequency domain. However, considering the nonlinear cyclic loading effects in the soil highly complicates the analysis. The response needs to be determined in the time domain, where the SSI is represented by nonlinear macro-element formulations. The main issues in the development of these SSI formulations can be assigned to:

- The soil layers can not be considered uncoupled for large diameter monopiles in the low-frequency range.

- The behaviour of saturated sands under cyclic loading is a highly complex phenomenon. The change in properties depends on various factors such as the type of loading and the state of the soil.

7.2.   Discussion

The results presented in this thesis are obtained on the basis of various assumptions and simplifications. This section presents a discussion of these points.

The soil motions in the 1D seismic Winkler-beam model are based on a ground response model. This model simplifies the soil as a 1D shear beam. The restriction of such a shear beam is that only the shear waves travelling in the vertical direction are modelled. Pressure waves, surface waves and inclined shear waves are not present in the analysis. Although the vertical travelling shear waves carry most of the energy, the other wave types could play a role (58).

The closed-form solutions of the soil response are based on the assumption that the soil is a linear elastic homogeneous isotropic material. This assumption can be used for many offshore wind load cases, but is expected to be incorrect for a seismic response analysis. Nonlinear cyclic loading effects are expected during significant ground motions, especially near the mudline. The effect of this nonlinear soil behaviour should be assessed with a FEA with a constitutive soil material model. Moreover, the soil stiffness usually varies with depth. Accounting for this variation heavily complicates the derivation of the soil response equation. The response modes and corresponding cut-off frequencies obtained from the linear closed-form solution are not correct for a realistic soil column. The variation in stiffness been implemented afterwards in this thesis.

The nonlinear soil material model used in the 3D FE model and the 2D plane strain FE model is a simplification of actual soil behaviour. The soil is modelled as a two phase material with a Mohr-Coulomb yield surface. The solid component of the two-phase material is linear isotropic. Changing the hydraulic conductivity coefficient allows for both drained and undrained analysis. The magnitude of the Mohr-Coulomb failure criteria is a function of the effective stress, which is determined in the two-phase analysis. The coupling of the Mohr-Coulomb yield surface with the two-phase material therefore allows soil failure due to excess pore-pressure buildup. However, there is no coupling between the shear and volumetric strains. The gradual accumulation of irreversible strains due to cyclic loading can therefore not be captured. More advanced constitutive models are required for this type of analysis.

The hybrid frequency-time domain Winkler extension is based on linear theory. The use of the non-linear foundation properties is therefore incorrect. The nonlinear amplitude dependency could not be included in the model as the pile's displacement amplitude is not known beforehand in a time domain analysis. Also, transient foundation response was not included in the model since the obtained foundation properties are based on the steady-state harmonic response.

The soil response obtained from the analyses is a function of relative distance between the pile and the soil. The functions in this thesis have been obtained for the harmonic excitation of the pile. However, the soil also experiences lateral displacement during an earthquake. The mechanism related to the soil displacement might be different from that of the pile displacement.

Performing the FEA with the nonlinear soil properties showed to be computationally demanding. The preferred mesh density could not be realised as this resulted in unrealistic computational times. The mesh density for the nonlinear models has been reduced in order to limit the computational time of the analyses to 3 days. The coarsening of the mesh showed little change in a convergence study. However, the results have not been validated with external results as these were not available.

The FE models developed in ANSYS are either validated by analytical expressions or with the results from a model in a similar research. However, the results obtained from the dynamic and nonlinear analysis have not been properly validated. This should be done with other models and, preferably, test data from experiments.

7.3. Recommendations for Further Work

This thesis investigated several aspects of a SSI representation for a 1D Winkler foundation that can be used for the seismic analysis of monopiles. The complexity of this extensive topic requires further research as there is still a lot of uncertainty in the mechanisms involved. Topics that require further investigation are presented below.

The plane strain and plane stress method showed that the response of the soil is determined by both 2D as well as 3D mechanisms, depending on the excitation frequency. Extending the 2D harmonic response analysis, as presented in this thesis, to a full 3D analysis could yield valuable insights into the global SSI response during an earthquake. The use of a 3D model is already the recommended approach according to the DNV-GL guideline for static analysis.

The investigation of the nonlinear response in this thesis was limited to a two-phase material model with a pressure dependent yield surface. True cyclic soil behaviour is much more complex, and there are several other mechanisms that could play a role in a seismic SSI description. It would be interesting to first of all, determine which mechanisms play a dominant role, and secondly, model the complex nonlinear soil response. Several academic constitutive soil models are available that could be used for such an investigation.

The hybrid frequency-time domain Winkler model showed to perform poorly for the nonlinear soil parameters. The exact reason for this is not determined, but it could be due to the use of steady-state foundation parameters. A method that would allow the implementation of nonlinear and transient effects into the combined frequency-time domain method could therefore be of value. An example would be the use of a feedback loop in the model which accounts for transient effects, by e.g. changing the retardation function. A proper implementation of such a solution is to be investigated.

Bibliography

[1] A Hashash, Y. M. (2016). DEEPSOIL USER MANUAL. Technical report.

[2] Al-Saggaf, U. and Franklin, G. (1987). An error bound for a discrete reduced order model of a linear multivariable system. *IEEE Transactions on Automatic Control*, 32(9):815–819.

[3] Alati, N., Failla, G., and Arena, F. (2015). Seismic analysis of offshore wind turbines on bottom-fixed support structures. *Philosophical Transactions of the Royal Society A: Mathematical, Physical and Engineering Sciences*, 373(2035):20140086–20140086.

[4] Andersen, L. V., Vahdatirad, M. J., Sichani, M. T., and Sørensen, J. D. (2012). Natural frequencies of wind turbines on monopile foundations in clayey soils-A probabilistic approach. *Computers and Geotechnics*, 43:1–11.

[5] Anoyatis, G., Mylonakis, G., and Lemnitzer, A. (2016). Soil reaction to lateral harmonic pile motion. *Soil Dynamics and Earthquake Engineering*, 87:164–179.

[6] ANSYS Inc (2018). No TitleANSYS Mechanical APDL Users Guide. Technical report.

[7] API (2000). Recommended Practice for Planning, Designing and Constructing Fixed Offshore PlatformsWorking Stress Design. Technical report, American Petroleum Institute.

[8] Baranov, V. (1967). On the calculation of an embedded foundation. *Voprosy Di- namiki i Prochnosti*, 14:195209.

[9] Bazeos, N., Hatzigeorgiou, G. D., Hondros, I. D., Karamaneas, H., Karabalis, D. L., and Beskos, D. E. (2002). Static, seismic and stability analyses of a prototype wind turbine steel tower. *Engineering Structures*, 24(8):1015–1025.

[10] Been, K. and Jefferies, M. (1985). A state parameter for sands, Geotechnique, 35(2), 99112. *Geotechnique*, 35(2):99–112.

[11] Bhattacharya, S. (2014). Challenges in Design of Foundations for Offshore Wind Turbines. *Engineering & Technology Reference*.

[12] Boulanger, R. and Ziotopoulou, K. (2017). A sand plasticity model for earthquake engineering applications. UCD/CGM-17(May):1–114.

[13] Boulanger, R. W., Curras, C. J., Kutter, B. L., Wilson, D. W., and Abghari, A. (1999). Seismic Soil-Pile-Structure Interaction Experiments and Analyses. *Journal of Geotechnical and Geoenvironmental Engineering*, 125(9):750–759.

[14] Bozorgnia, Y. and Bertero, V. V. (2006). *Earthquake engineering*. Taylor & Francis e-Library.

[15] Brandenberg, S. J., Boulanger, R. W., Kutter, B. L., and Chang, D. (2005). Behavior of Pile Foundations in Laterally Spreading Ground during Centrifuge Tests. *Journal of Geotechnical and Geoenvironmental Engineering*.

[16] BRUNE, J. N. (1970). Tectonic Stress and the Spectra of Seismic Shear Waves from Earthquakes. *Physics*, 75(26).

[17] Byrne, B., McAdam, R., Burd, H., Houlsby, G., Martin, C., C, L., Taborda, D., Potts, D., Jardine, R., Sideri, M., Schroeder, F., Gavin, K., Doherty, P., Igoe, D., Wood, A., Kallehave, D., and Gretlund, J. (2015). New design methods for large diameter piles under lateral loading for offshore wind applications. In *Frontiers in Offshore Geotechnics III*, pages 705–710.

[18] Carter, J. M. F. (2007). North Hoyle offshore wind farm: design and build. *Proceedings of the ICE - Energy*, 160(1):21–29.

[19] Cook, M. F. and Vandiver, J. K. (1982). Measured and Predicted Dynamic Response of a Single Pile

Platform to Random Wave Excitation. *Offshore Technology Conference*.

[20] Cummins, W. (1962). The impulse response function and ship motions. *Schiffstechnik*, 9(1661):101–109.

[21] Dafalias, Y. F. and Manzari, M. T. (2004). Simple plasticity sand model accounting for fabric change effects. *Journal of Engineering Mechanics, ASCE*, 130(6):622–634.

[22] Damgaard, M., Bayat, M., Andersen, L. V., and Ibsen, L. B. (2014a). Assessment of the dynamic behaviour of saturated soil subjected to cyclic loading from offshore monopile wind turbine foundations. *Computers and Geotechnics*, 61:116–126.

[23] Damgaard, M., Zania, V., Andersen, L. V., and Ibsen, L. B. (2014b). Effects of soil-structure interaction on real time dynamic response of offshore wind turbines on monopiles. *Engineering Structures*, 75:388–401.

[24] Dash, S. and Bhattacharya, S. (2015). Pore water pressure generation and dissipation near to pile and far-field in liquefiable soils. *International Journal of GEOMATE*.

[25] De Risi, R., Bhattacharya, S., and Goda, K. (2018). Seismic performance assessment of monopile-supported offshore wind turbines using unscaled natural earthquake records. *Soil Dynamics and Earthquake Engineering*, 109(March):154–172.

[26] Di Laora, R., Mylonakis, G., and Mandolini, A. (2017). Size Limitations for Piles in Seismic Regions. *Earthquake Spectra*.

[27] DNV (2014). DNV-OS-J101: Design of Offshore Wind Turbine Structures. Technical report, Det Norske Veritas.

[28] Dobry, R., Abdoun, T., ORourke, T. D., and Goh, S. H. (2003). Single Piles in Lateral Spreads: Field Bending Moment Evaluation. *Journal of Geotechnical and Geoenvironmental Engineering*.

[29] Dong, Y., Lu, N., and McCartney, J. S. (2018). Scaling Shear Modulus from Small to Finite Strain for Unsaturated Soils. *Journal of Geotechnical and Geoenvironmental Engineering*, 144(2):04017110.

[30] E. Taciroglu, C. Rha, J. W. (2006). A robust macroelement model for soil-pile interaction under cyclic loads. *Geotech Geoenviron*, 132:1304–1314.

[31] Eurocode 8 (2004). Design of structures for earthquake resistance - Part 1 : General rules, seismic actions and rules for buildings. Technical report.

[32] Gazetas, G. (1984). Seismic response of end-bearing single piles. *International Journal of Soil Dynamics and Earthquake Engineering*.

[33] Ghosh, B., Mian, J., and Lubkowski, Z. (2012). Design of piles in liquefiable soil: A review of design codes and methodologies. *Wcee*, pages 1–10.

[34] GL (2010). Guideline for the Certification of Wind Turbines. Technical report, Germanischer Lloyd, Hamburg, Germany.

[35] GovindaRaju, L., Ramana, G., HanumanthaRao, C., and Sitharam, G. (2004). Site-specific ground response analysis. *Current Science*, 87(10):1354–1362.

[36] Green, R., Mitchell, J., and Polito, C. (2000a). An Energy-Based Pore Pressure Generation Model for Cohesionless Soils. *Proceedings: John Booker Memorial Symposium, Melbourne, Australia*, pages 16–17.

[37] Green, R. A., Mitchell, J. K., and Polito, C. P. (2000b). An energy-based excess pore pressure generation model for cohesionless soils. In *John Booker memorial symposium*.

[38] Grelle, G., Bonito, L., Lampasi, A., Revellino, P., Guerriero, L., Sappa, G., and Guadagno, F. M. (2016). SiSeRHMap v1.0: A simulator for mapped seismic response using a hybrid model. *Geoscientific Model Development*, 9(4):1567–1596.

[39] GWEC (2017). Global Wind Report 2016. Technical report, Global Wind Energy Council, Brussel.

[40] Hashash, Y. M. and Park, D. (2001). Non-linear one-dimensional seismic ground motion propagation in the Mississippi embayment. *Engineering Geology*, 62:185–206.

[41] Hermans, K. W. and Peeringa, J. M. (2016). Future XL monopile foundation design for a 10 MW wind turbine in deep water. (December).

[42] Herrera, J., Aznárez, J. J., Padrón, L. A., and Maeso, O. (2017). Observations on the influence of

soil profile on the seismic kinematic bending moments of offshore wind turbine monopiles. In *Procedia Engineering*.

[43] Ho, B. and Kalman, R. (1966). Effective reconstruction of linear state-variable models from input/output functions. *Regelungstechnik*, 14(12):417441.

[44] Hongwang, M. (2012). Seismic analysis for wind turbines including soil-structure interaction combining vertical and horizontal earthquake. *15th World Conference on Earthquake Engineering*, (2009).

[45] Idriss, I. and Boulanger, R. W. (2008). *Soil liquefaction during earthquakes*. EERI.

[46] IEC (2005). IEC 61400-1: Wind turbines - Part 1: Design requirements. Technical report, International Electrotechnical Commission, Geneva, Switzerland.

[47] Ishihara, K., Yoshida, N., and Tsujino, S. (1985). Modelling of stress-strain relations of soils in cyclic loading. *Proc. 5th Int. Conf. on Numer. Meth. in Geomech. , Nagoya, Japan*, pages 373–380.

[48] Ishihara, T. and Sawar, M. W. (2008). Numerical and Theoretical Study on Seismic Response of Wind Turbines. *European Wind Energy Conference and Exhibition*.

[49] ISO (2004). ISO 19901-2:2004. Technical report, International Organization for Standardization.

[50] ISO (2005). ISO 23469:2005. Technical report.

[51] Jefferys, E. R. (1984). Simulation of wave power devices. *Applied Ocean Research*, 6(1):31–39.

[52] Jin, X., Liu, H., and Ju, W. (2014). Wind turbine seismic load analysis based on numerical calculation. *Strojniski Vestnik/Journal of Mechanical Engineering*, 60(10):638–648.

[53] Jonkman, J., Butterfield, S., Musial, W., and Scott, G. (2009). Definition of a 5-MW Reference Wind Turbine for Offshore System Development. (February).

[54] JRA (2002). Specifications for highway bridges. Japan Road Association. Technical report.

[55] Kallehave, D., Byrne, B. W., LeBlanc Thilsted, C., and Mikkelsen, K. K. (2015). Optimization of monopiles for offshore wind turbines. *Philosophical Transactions of the Royal Society A: Mathematical, Physical and Engineering Sciences*, 373(2035).

[56] Katsanos, E. I., Thöns, S., and Georgakis, C. (2016). Wind turbines and seismic hazard: a state-of-the-art review. *Wind Energy*, 19(11):2113–2133.

[57] Kavvads, M. and Gazetas, G. (1993). Kinematic seismic response and bending of free-head piles in layered soil. *Géotechnique*.

[58] Kaynia, A. M. (2017). Earthquake response of offshore wind turbines.

[59] Kaynia, A. M. (2018). Seismic considerations in design of offshore wind turbines. *Soil Dynamics and Earthquake Engineering*, (September 2017):0–1.

[60] Kim, D. H., Lee, S. G., and Lee, I. K. (2014). Seismic fragility analysis of 5MW offshore wind turbine. *Renewable Energy*, 65:250–256.

[61] Kiyomiya, O., Rikiji, T., and Van Gelder, P. H. A. J. M. (2002). Dynamic Response Analysis of Onshore Wind Energy Power Units during Earthquakes and Wind. In *Proceedings of The Twelfth (2002) International Offshore and Polar Engineering Conference*, pages 520–526.

[62] Kjørlaug, R. A. and Kaynia, A. M. (2015). Vertical earthquake response of megawatt-sized wind turbine with soil-structure interaction effects. *Earthquake Engineering and Structural Dynamics*, 44(13):2341–2358.

[63] Kjørlaug, R. A., Kaynia, A. M., and Elgamal, A. (2014). Seismic Response of Wind Turbines due to Earthquake and Wind Loading. *Eurodyn 2014: Ix International Conference on Structural Dynamics*, (July):3627–3634.

[64] Kondner, R. L. and Zelasko, J. S. (1963). A hyperbolic stress-strain formulation of sands. *Proc. 2nd Pan Am. Conf. on Soil Mech. and Found. Engrg.*, pages 289–324.

[65] KOST, C., JÜLCH, S. S. V., and SCHLEGL, H.-T. N. T. (2018). LEVELIZED COST OF ELECTRICITY RENEWABLE ENERGY TECHNOLOGIES. Technical report.

[66] Kourkoulis, R., Gelagoti, F., Georgiou, I., Karamanos, S., and Gazetas, G. (2017). On the adequacy of existing foundation schemes for offshore wind turbines subjected to extreme loading. In *Proceedings of the International Conference on Offshore Mechanics and Arctic Engineering - OMAE*,

volume 10.

[67] Kramer, s. L. (1996). *Geotechnical Earthquake Engineering*. Pearson Education Limited, Essex, new intern edition.

[68] Kung, S. (1978). A new identification and model reduction algorithm via singular value decompositions. *Twelfth Asilomar Conference on Circuits, Systems and Computers*, page pp. 705714.

[69] L. Liu, R. D. (1995). Effect of liquefaction on lateral response of piles by centrifuge model tests. *National Center for Earthquake Engineering Research (NCEER) Bulletin*, 9:7–11.

[70] Lade, P. V. (2005). Overview of Constitutive Models for Soils. *Soil Constitutive Models*, 40771(January 2005):1–34.

[71] Lavassas, I., Nikolaidis, G., Zervas, P., Efthimiou, E., Doudoumis, I. N., and Baniotopoulos, C. C. (2003). Analysis and design of the prototype of a steel 1-MW wind turbine tower. *Engineering Structures*, 25(8):1097–1106.

[72] Liyanapathirana, D. S. and Poulos, H. G. (2005). Pseudostatic approach for seismic analysis of piles in liquefying soil. *Journal of Geotechnical and Geoenvironmental Engineering*.

[73] Lombardi, D., Bhattacharya, S., and Muir Wood, D. (2013). Dynamic soil-structure interaction of monopile supported wind turbines in cohesive soil. *Soil Dynamics and Earthquake Engineering*, 49:165–180.

[74] Lombardi, D., Dash, S. R., Bhattacharya, S., Ibraim, E., Muir Wood, D., and Taylor, C. A. (2017). Construction of simplified design <i>p</i> <i>y</i> curves for liquefied soils. *Géotechnique*.

[75] Mar, M. and Novak, M. (1991). Piles Under Dynamic Loads.

[76] Mardfekri, M., Gardoni, P., and Roesset, J. M. (2013). Modeling Laterally Loaded Single Piles Accounting for Nonlinear Soil-Pile Interactions. *Journal of Engineering (United States)*, 2013.

[77] Matasovic, N. and Vucetic, M. (1993). CYCLIC CHARACTERIZATION OF LIQUEFIABLE SANDS. *J. Geotech. Engrg.*, 119(11):1805–1822.

[78] Mo, R., Kang, H., Li, M., and Zhao, X. (2017). Seismic Fragility Analysis of Monopile Offshore Wind Turbines under Different Operational Conditions. *Energies*, 10(7):1037.

[79] Mostafa, Y. E. and El Naggar, M. H. (2004). Response of fixed offshore platforms to wave and current loading including soil-structure interaction. *Soil Dynamics and Earthquake Engineering*, 24(4):357–368.

[80] Musial, W., Beiter, P., Schwabe, P., Tian, T., Stehly, T., and Spitsen, P. (2017). 2016 Offshore Wind Technologies Market Report. Technical report, U.S. Department of Energy, Washington D.C.

[81] Mylonakis, G. and Gazetas, G. (2002). Kinematic Pile Response to Vertical P-wave Seismic Excitation. *Journal of Geotechnical and Geoenvironmental Engineering*.

[82] Mylonakis, G., Nikolaou, A., and Gazetas, G. (1997). Soil-pile-bridge seismic interaction: Kinematic and inertial effects. Part I: Soft soil. *Earthquake Engineering and Structural Dynamics*.

[83] N. Gerolymos, G. G. (2006). Development of Winkler model for static and dynamic response of caisson foundations with soil and interface nonlinearities. *Soil Dyn Earthq Eng*, 26:363–376.

[84] Nielsen, A. H. (2006). <Architecture_Absorbing_Auc06_Babtie.Pdf>. pages 359–376.

[85] Nogami, T. and Novak, M. (1977). Resistance of soil to a horizontally vibrating pile. *Earthquake Engineering & Structural Dynamics*, 5(3):249–261.

[86] Novak, M. (1974). Dynamic Stiffness and Damping of Piles. *Canadian Geotechnical Journal*, 11(4):574–598.

[87] Nuta, E., Christopoulos, C., and Packer, J. A. (2011). Methodology for seismic risk assessment for tubular steel wind turbine towers: application to Canadian seismic environment. *Canadian Journal of Civil Engineering*, 38(3):293–304.

[88] Panzer, H., Eid, R., and Lohmann, B. (2009). Generating a Parametric Finite Element Model of a 3D Cantilever Timoshenko Beam Using Matlab. (January):1–8.

[89] Polito, C. P., Green, R. A., and Lee, J. (2008). Pore Pressure Generation Models for Sands and Silty Soils Subjected to Cyclic Loading. *Journal of Geotechnical and Geoenvironmental Engineering*.

[90] Prowell, I. (2011). *An Experimental and Numerical Study of Wind Turbine Seismic Behavior*. PhD

thesis, University of California, San Diego.

[91] Prowell, I. and Veers, P. (2009). Assessment of Wind Turbine Seismic Risk: Existing Literature and Simple Study of Tower Moment Demand. Technical report, Sandia National Laboratories, Albuquerque, New Mexico and Livermore, California.

[92] Prowell, I., Veletzos, M., Elgamal, A., and Restrepo, J. (2009). Experimental and numerical seismic response of a 65 kW wind turbine. *Journal of Earthquake Engineering*, 13(8):1172–1190.

[93] R. D. Cook, D. S. Malkus, M. E. P. and Witt, R. J. (2002). *Concepts and Applications of Finite Element Analysis*. John Wiley & Sons, Inc., Hoboken, NJ, USA,, 4 edition.

[94] Randolph, M. and Gourvenec, S. (2011). *Offshore Geotechnical Engineering*. CRC Press LLC.

[95] Risø (2002). Guidelines for Design of Wind Turbines. Technical report, Wind Energy Department of Risø National Laboratory and Det Norske Veritas, Copenhagen, Denmark.

[96] Ritschel, U., Warnke, I., Kirchner, J., and Meussen, B. (2003). Wind turbines and earthquakes. *2nd World Wind Energy Conference*, pages 1–8.

[97] Rollins, K. M., Gerber, T. M., Lane, J. D., and Ashford, S. a. (2005). Lateral Resistance of a Full-Scale Pile Group in Liquefied Sand. *Journal of Geotechnical and Geoenvironmental Engineering*.

[98] Roscoe, K. H., Schofield, A. N., and Wroth, C. P. (1958). On The Yielding of Soils. *Géotechnique*, 8(1):22–53.

[99] Sapountzakis, E. J., Dikaros, I. C., Kampitsis, A. E., and Koroneou, A. D. (2015). Nonlinear Response of Wind Turbines Under Wind and Seismic Excitations With SoilStructure Interaction. *Journal of Computational and Nonlinear Dynamics*, 10(4):041007.

[100] Seed, H., Martin, P., and Lysmer, J. (1975). The generation and dissipation of pore water pressures during soil liquefaction. *Rep. No. EERC*, 75(26).

[101] Seidel, M., Voormeeren, S., and van der Steen, J.-B. (2016). State-of-the-art design processes for offshore wind turbine support structures. *Stahlbau*, 85(9):583–590.

[102] sif (2018). sif visit statement.

[103] Stamatopoulos, G. N. (2013). Response of a wind turbine subjected to near-fault excitation and comparison with the Greek Aseismic Code provisions. *Soil Dynamics and Earthquake Engineering*.

[104] Stehly, T., Heimiller, D., and Scott, G. (2017). 2016 Cost of Wind Energy Review. Technical Report December, National Renewable Energy Laboratory, Golden.

[105] Taghipour, R., Perez, T., and Moan, T. (2008). Hybrid frequency-time domain models for dynamic response analysis of marine structures. *Ocean Engineering*, 35(7):685–705.

[106] Tokimatsu, K., Suzuki, H., and Sato, M. (2005). Effects of inertial and kinematic interaction on seismic behavior of pile with embedded foundation. *Soil Dynamics and Earthquake Engineering*.

[107] Tokimatsu, K., Suzuki, H., and Suzuki, Y. (2001). Back-Calculated p-y Relation of Liquefied Soils from large Shaking Table Tests. *International Conferences on Recent Advances in Geotechnical Earthquake Engineering and Soil Dynamics*, pages 1–6.

[108] Valamanesh, V. and Myers, A. T. (2014). Aerodynamic Damping and Seismic Response of Horizontal Axis Wind Turbine Towers. *Journal of Structural Engineering*, 140(11):04014090.

[109] Varun (2010). *A NON-LINEAR DYNAMIC MACROELEMENT FOR SOIL STRUCTURE INTERACTION ANALYSES OF PILES IN LIQUEFIABLE SITES*. PhD thesis, Georgia Institute of Technology.

[110] Veletsos, A. and Younan, A. H. (1994a). Dynamic Soil Pressures on Rigid Retaining Walls. *Earthquake Engineering and Structural Dynamics*, 23(July 1993):275–301.

[111] Veletsos, A. S. and Younan, A. H. (1994b). Dynamic Modeling and Response of SoilWall Systems. *Journal of Geotechnical Engineering*, 120(12):2155–2179.

[112] Versteijlen, P. (2018). *Identification of effective 1D soil models for large-diameter offshore wind turbine foundations based on in-situ seismic measurements and 3D modelling*.

[113] Versteijlen, W., Metrikine, A., Hoving, J., Smid, E., and De Vries, W. (2011). Estimation of the vibration decrement of an offshore wind turbine support structure caused by its interaction with soil. *Proceedings of the EWEA Offshore 2011 Conference, Amsterdam, The Netherlands, 29 November-1 December 2011*.

[114] Vestas (2011). Vestas V164-8.0 MW Brochure.

[115] Wang, R. (2016). *Single Piles in Liquefiable Ground: Seismic Response and Numerical Analysis Methods*. Springer Nature, Berlin.

[116] Wang, W., Gao, Z., Li, X., Moan, T., and Wang, B. (2016). Model Test and Numerical Analysis of an Offshore Bottom Fixed Pentapod Wind Turbine under Seismic Loads. In *Proceedings of the ASME 2016 35th International Conference on Ocean, Offshore and Arctic Engineering*, pages 1–11.

[Whyte] Whyte, S. Foundation Optimisation for Ever Larger Offshore Wind Turbines: Geotechnical Perspective: KIVI lecture Fugro.

[118] Wilson, D. (1998). *Soil-Pile-Superstructure Interaction in Liquefying Sand and Soft Clay*. PhD thesis.

[119] Wilson, D. W., Boulanger, R. W., and Kutter, B. L. (2000). OBSERVED SEISMIC LATERAL RESISTANCE OF LIQUEFYING SAND. *J. Geotech. Geoenviron. Eng.*, 126(10):898–906.

[120] WindEurope (2017). Floating Offshore Wind Vision Statement. Technical Report June, WindEurope, Brussels.

[121] WindEurope (2018). Offshore Wind in Europe - Key trends and statistics 2017. Technical report, WindEurope, Brussels.

[122] Wu, M., M. T. (1996). Linear and nonlinear hydroelastic analysis of high-speed vessels. *Journal of Ship Research*, 40:149163.

[123] Yu, H., Zeng, X., Neff, F. H., Li, B., and Lian, J. (2015). Centrifuge modeling of offshore wind foundations under earthquake loading. *Soil Dynamics and Earthquake Engineering*.

[124] Zania, V. (2014). Natural vibration frequency and damping of slender structures founded on monopiles. *Soil Dynamics and Earthquake Engineering*, 59:8–20.

[125] Zhao, X. and Maißer, P. (2006). Seismic response analysis of wind turbine towers including soil-structure interaction. *Proceedings of the Institution of Mechanical Engineers, Part K: Journal of Multi-body Dynamics*, 220(1):53–61.

[126] Zheng, X. Y., Li, H., Rong, W., and Li, W. (2015). Joint earthquake and wave action on the monopile wind turbine foundation: An experimental study. *Marine Structures*.

Appendix A

Mathematical Expressions

A.1. Relationships in Elasticity Theory

A.1.1. Strain-Displacement Equations

Cartesian Coordinates

$$\epsilon_x = \frac{\partial u}{\partial x} \tag{A.1a}$$

$$\epsilon_y = \frac{\partial v}{\partial y} \tag{A.1b}$$

$$\epsilon_z = \frac{\partial w}{\partial z} \tag{A.1c}$$

$$\gamma_{xy} = \frac{\partial v}{\partial x} + \frac{\partial u}{\partial y} \tag{A.1d}$$

$$\gamma_{yz} = \frac{\partial w}{\partial y} + \frac{\partial v}{\partial z} \tag{A.1e}$$

$$\gamma_{xz} = \frac{\partial u}{\partial z} + \frac{\partial w}{\partial x} \tag{A.1f}$$

Cylindrical Coordinates

$$\epsilon_r = \frac{\partial u}{\partial r} \tag{A.2a}$$

$$\epsilon_\theta = \frac{\partial u}{\partial r} + \frac{1}{r}\frac{\partial v}{\partial \theta} \tag{A.2b}$$

$$\epsilon_z = \frac{\partial w}{\partial z} \tag{A.2c}$$

$$\gamma_{r\theta} = \frac{\partial v}{\partial r} + \frac{1}{r}\frac{\partial u}{\partial \theta} - \frac{v}{r} \tag{A.2d}$$

$$\gamma_{yz} = \frac{1}{r}\frac{\partial w}{\partial \theta} + \frac{\partial v}{\partial z} \tag{A.2e}$$

$$\gamma_{xz} = \frac{\partial u}{\partial z} + \frac{\partial w}{\partial r} \tag{A.2f}$$

A.1.2. Equilibrium Equations

Cartesian Coordinates

$$\frac{\partial \sigma_{xx}}{\partial x} + \frac{\partial \sigma_{xy}}{\partial y} + \frac{\partial \sigma_{xz}}{\partial z} + F_x = 0 \tag{A.3a}$$

$$\frac{\partial \sigma_{yy}}{\partial y} + \frac{\partial \sigma_{xy}}{\partial x} + \frac{\partial \sigma_{yz}}{\partial z} + F_y = 0 \tag{A.3b}$$

$$\frac{\partial \sigma_{zz}}{\partial z} + \frac{\partial \sigma_{xz}}{\partial x} + \frac{\partial \sigma_{yz}}{\partial y} + F_z = 0 \tag{A.3c}$$

Cylindrical Coordinates

$$\frac{\partial \sigma_{rr}}{\partial r} + \frac{\sigma_r r - \sigma_\theta \theta}{r} + \frac{1}{r}\frac{\partial \sigma_{r\theta}}{\partial \theta} + \frac{\partial \sigma_{rz}}{\partial z} + F_r = 0 \tag{A.4a}$$

$$\frac{1}{r}\frac{\partial \sigma_{\theta\theta}}{\partial \theta} + \frac{\partial \sigma_{r\theta}}{\partial r} + \frac{2\sigma_{r\theta}}{r} + \frac{\partial \sigma_{\theta z}}{\partial z} + F_\theta = 0 \tag{A.4b}$$

$$\frac{\partial \sigma_{zz}}{\partial z} + \frac{1}{r}\frac{\partial \sigma_{z\theta}}{\partial \theta} + \frac{\partial \sigma_{rz}}{\partial r} + \frac{\sigma_{rz}}{r} + F_z = 0 \tag{A.4c}$$

A.1.3. Hooke's Law for Isotropic Materials

$$\begin{bmatrix} \sigma_{11} \\ \sigma_{22} \\ \sigma_{33} \\ \sigma_{12} \\ \sigma_{13} \\ \sigma_{23} \end{bmatrix} = \begin{bmatrix} \lambda+2\mu & \lambda & \lambda & 0 & 0 & 0 \\ \lambda & \lambda+2\mu & \lambda & 0 & 0 & 0 \\ \lambda & \lambda & \lambda+2\mu & 0 & 0 & 0 \\ 0 & 0 & 0 & 2\mu & 0 & 0 \\ 0 & 0 & 0 & 0 & 2\mu & 0 \\ 0 & 0 & 0 & 0 & 0 & 2\mu \end{bmatrix} \begin{bmatrix} \epsilon_{11} \\ \epsilon_{22} \\ \epsilon_{33} \\ \epsilon_{12} \\ \epsilon_{13} \\ \epsilon_{23} \end{bmatrix} \tag{A.5}$$

A.2. Discrete Timoshenko-Beam Matrix Formulation

Discrete 6 DOF matrix format of the Timoshenko beam formulation (88).

$$\mathbf{M}^e = \begin{bmatrix} \mathbf{M}_{11}^e & \mathbf{M}_{12}^e \\ \mathbf{M}_{21}^e & \mathbf{M}_{22}^e \end{bmatrix}, \quad \mathbf{K}^e = \begin{bmatrix} \mathbf{K}_{11}^e & \mathbf{K}_{12}^e \\ \mathbf{K}_{21}^e & \mathbf{K}_{22}^e \end{bmatrix}$$

$$\mathbf{M}_{11}^e = m_e \begin{bmatrix} \frac{1}{3} & 0 & 0 & 0 & 0 & 0 \\ 0 & \frac{13}{35}+\frac{6I_z}{5Al^2} & 0 & 0 & 0 & \frac{11l}{210}+\frac{I_z}{10Al} \\ 0 & 0 & \frac{13}{35}+\frac{6I_y}{5Al^2} & 0 & -\frac{11l}{210}-\frac{I_y}{10Al} & 0 \\ 0 & 0 & 0 & \frac{I_p}{3A} & 0 & 0 \\ 0 & 0 & -\frac{11l}{210}-\frac{I_y}{10Al} & 0 & \frac{l^2}{105}+\frac{2I_y}{15A} & 0 \\ 0 & \frac{11l}{210}+\frac{I_z}{10Al} & 0 & 0 & 0 & \frac{l^2}{105}+\frac{2I_z}{15A} \end{bmatrix}$$

$$\mathbf{M}_{21}^e = \mathbf{M}_{12}^{e\,T} = m_e \begin{bmatrix} \frac{1}{6} & 0 & 0 & 0 & 0 & 0 \\ 0 & \frac{9}{70}-\frac{6I_z}{5Al^2} & 0 & 0 & 0 & +\frac{13l}{420}-\frac{I_z}{10Al} \\ 0 & 0 & \frac{9}{70}-\frac{6I_y}{5Al^2} & 0 & -\frac{13l}{420}+\frac{I_y}{10Al} & 0 \\ 0 & 0 & 0 & \frac{I_p}{6A} & 0 & 0 \\ 0 & 0 & \frac{13l}{420}-\frac{I_y}{10Al} & 0 & -\frac{l^2}{140}-\frac{2I_y}{30A} & 0 \\ 0 & -\frac{13l}{420}+\frac{I_z}{10Al} & 0 & 0 & 0 & -\frac{l^2}{140}-\frac{2I_z}{30A} \end{bmatrix}$$

$$\mathbf{K}_{11}^e = \frac{1}{l^3} \begin{bmatrix} Al^2 & 0 & 0 & 0 & 0 & 0 \\ 0 & \dfrac{12EI_z}{1+P_y} & 0 & 0 & 0 & \dfrac{6EI_zl}{1+P_y} \\ 0 & 0 & \dfrac{12EI_y}{1+P_z} & 0 & -\dfrac{6EI_yl}{1+P_z} & 0 \\ 0 & 0 & 0 & GI_tl^2 & 0 & 0 \\ 0 & 0 & -\dfrac{6EI_yl}{1+P_z} & 0 & \dfrac{EI_yl^2(4+P_z)}{1+P_z} & 0 \\ 0 & \dfrac{6EI_zl}{1+P_y} & 0 & 0 & 0 & \dfrac{EI_zl^2(4+P_y)}{1+P_y} \end{bmatrix}$$

$$\mathbf{K}_{21}^e = {\mathbf{K}_{12}^e}^T = \frac{1}{l^3} \begin{bmatrix} -EAl^2 & 0 & 0 & 0 & 0 & 0 \\ 0 & -\dfrac{12EI_z}{1+P_y} & 0 & 0 & 0 & -\dfrac{6EI_zl}{1+P_y} \\ 0 & 0 & -\dfrac{12EI_y}{1+P_z} & 0 & \dfrac{6EI_yl}{1+P_z} & 0 \\ 0 & 0 & 0 & -GI_tl^2 & 0 & 0 \\ 0 & 0 & -\dfrac{6EI_yl}{1+P_z} & 0 & \dfrac{EI_yl^2(2-P_z)}{1+P_z} & 0 \\ 0 & \dfrac{6EI_zl}{1+P_y} & 0 & 0 & 0 & \dfrac{EI_zl^2(2-P_y)}{1+P_y} \end{bmatrix}$$

Appendix B

Numerical Issues with ANSYS

B.1.   Pore-Pressure Instability in Two-Phase Modelling

The FEM software ANSYS provides two-phase type elements as 8-node CPT213 for 2D and 20-node CPT216 for 3D. The models with these two-phase element types showed many stability issues. The numerical instability was related to the pore pressure, which kept growing exponentially till the model eventually exploded. Determining the source of the instability took much time and effort as the instability was unpredictable and seemed to be happening at random. The instability primarily started at boundaries in the model, leading to the assumption that it had something to do with certain boundary constraints or contact effects. Numerous different models with certain aspects of the model turned off were developed in an attempt to localise the source of the instability.

Two examples of the instability are presented in the figures B.1 and B.2. The first figure shows the emergence of a exponentially growing pore pressure field for the situation where there are no contact elements between the soil and pile (inner radius). Figure B.2 also shows the pore pressure variable in the soil for the situation where the soil-pile contact is modelled with contact elements.

The cause of the instability showed to be related to the bulk stiffness of the soil material. The reason for this instability is not exactly known. Certain combinations of material parameters did not show the instability. The exploding of the pressure degrees of freedom showed to be insensitive to various types of material damping. Eventually, the trial and error method showed that the instability is related to the ratio between the bulk modulii of the pore fluid and the soil skeleton. If not specified, ANSYS determines the value of the Biot coefficient based on the entered soil and pore fluid bulk modulii. Using a user specified Biot coefficient of 1 instead of the by ANSYS calculated one resulted in stable soil elements.
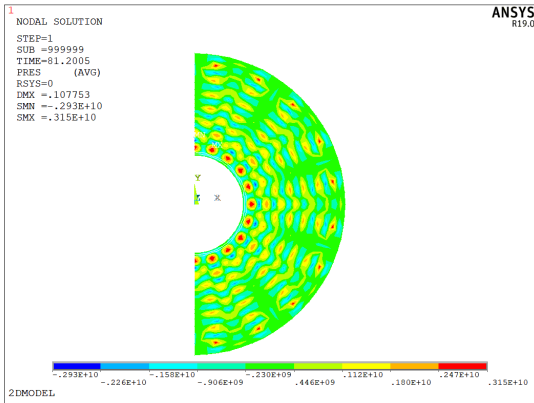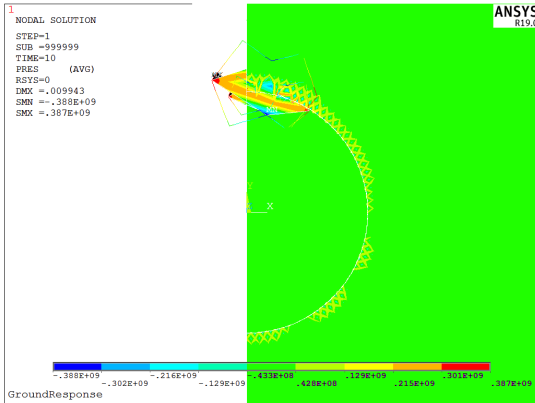

Figure B.1: Numerical instability

Figure B.2: Numerical instability

Appendix C

Liquefaction Modelling Attempts

C.1. Manual Pore-pressure build-up Implementation

Pore pressure build-up results in the decrease of effective stresses in the soil skeleton, according to equation 2.12. An attempt to model the effect of pore-pressure build-up and the resulting shear strength reduction was done by manually updating the pore pressure in the two-phase elements in a number of time steps. The CPT element types provided by ANSYS have an option to define an fluid in and outflow and a boundary pore pressure at every node. The pore-pressure ratio was determined according to the empirical formulation as presented in section 4.2.1.1. At specified time steps, the build-up pore pressure according to the formulation was determined and implemented into the model as boundary condition.

The method provided not the desired result. Small changes in the elements pressure related boundary conditions showed no change in response, while the required pressure build-up resulted in convergence issues.

This method was only test for the 2 dimensional SSI model. The 3 directions in the FEM seismic monopile response model highly complicated the method.

## C.2. PM4Sand Constitutive Soil Model

The accuracy of a FEM soil-structure interaction analysis is as accurate as the formulation of the soil material model. Material models trying to capture the mechanics of soil are referred to as constitutive models (section 2.3.4.1). An attempt to implement such a constitutive model in ANSYS models was done since manual implementation of pore pressure build-up was unsuccessful.

Recently, the sand plasticity model PM4Sand for geotechnical earthquake engineering applications was developed (12). The model is based on a framework set by (21), which comprises of a stress-ratio controlled, critical state compatible, bounding surface plasticity model for sand. The plastic characteristics of the model are determined by surfaces in the stress domain: bounding surface for ultimate plastic strength and dilatancy and critical surfaces to determine plastic volumetric strains. The surfaces in the stress ratio domain are presented in figure C.1. The plastic characteristics are a function of the distance from the yield surface to the normal of the other surfaces. The equations behind the PM4Sand model are all presented in the material models manual (12).

ANSYS provides the option to write self-defined constitutive material equations through the UserMat subroutine option. The subroutine defines the stress-strain relationship of a material and is called at every material integration point in the elements during the calculation of the solution (6). The subroutine calculated the new stresses and state variables based on the stresses, strains and state variables in the previous time step together with the strain increment occuring in that time step.

The subroutine is written in the programming language FORTRAN. This means that to be able to run the self defined subroutine in ANSYS, the code needs to be compiled with a FORTRAN and C++ com-

Figure C.1: Bounding, dilatancy, and yield surfaces on the ryy-rxy stress-ratio plane with the yield surface, normal tensor, dilatancy back stress ratio, and bounding back stress ratio. After (12)
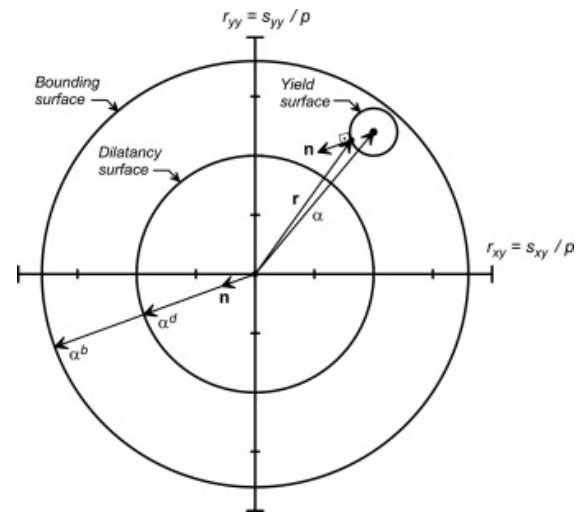
piler. The software required for this compilation could not be installed due to software safety regulations.